Optimal Electrical Activation of Retinal Ganglion Cells

Alexander Emmanuel Hadjinicolaou

August, 2013

A thesis submitted for the degree of Doctor of Philosophy
of The Australian National University

Declaration of Authorship

I hereby certify that this thesis and the work presented in it are, to the best of my knowledge, original and generated by me as the result of my own investigations. Except where acknowledged below, I was responsible for the collection of electrophysiological data, the classification of retinal ganglion cells, the writing of analysis software, and the analysis of data featured in this thesis.

Two chapters involved collaborations with external investigators:

- The work presented in Chapter 4, *Stimulating with N-UNCD*, was a collaborative effort in which I performed the electrophysiological data collection, RGC classification, and data analysis. All other work concerning the development, fabrication, and electrochemical testing of the diamond electrodes was performed by David Garrett and his team at the School of Physics, University of Melbourne. This work has been published previously: Hadjinicolaou, A. E., Leung, R. T., Garrett, D. J., Ganesan, K., Fox, K., Nayagam, D. A. X., Shivdasani, M. N., Meffin, H., Ibbotson, M. R., Prawer, S. and O'Brien, B. J. (2012). Electrical stimulation of retinal ganglion cells with diamond and the development of an all diamond retinal prosthesis. *Biomaterials* 33(24): 5812–5820.

- The work presented in Chapter 6, *Selective Sinusoidal Activation of RGCs*, features an RGC model (Kameneva et al., 2010) developed by Tatiana Kameneva, of the Centre for Neural Engineering, University of Melbourne. Tatiana provided the implementation of the model and assisted with the simulations. I was responsible for all data collection, RGC classification, and data analysis and interpretation.

Alexander Emmanuel Hadjinicolaou

March, 2013

Acknowledgements

Firstly, I would like to thank Michael Ibbotson, Shaun Cloherty, and Brendan O'Brien for their supervision and guidance over the length of my programme. Their collective brand of research is marked by equal helpings of optimism and pragmatism, which have had a strong influence on my own approach to identifying and solving problems. Aside from the sharing of ideas and fruitful discussions, my supervisors have been generous in doling out sanity checks, quips, lame jokes, and amusing anecdotes – all of which have kept me sharp and made the journey all the more entertaining.

I owe a great deal to my parents, Helene and Nick, who have always offered me their unconditional love and support in my endeavours. It is no understatement to say that without their continued interest in my education and personal development, I would not have the opportunity to write this thesis.

Finally, to my close friends, who at times have helped to keep me afloat amid figurative seas of excrement, I offer a large amount of gratitude. Our discussions are often a mechanism for self-discovery, which I use to continually reassess and refine my personal philosophies. The value of their company is beyond measure.

Abstract

Retinal prostheses are emerging as a viable therapy option for those blinded by degenerative eye conditions that destroy the photoreceptors of the retina but spare the retinal ganglion cells (RGCs). My research sought to address the issue of how a retinal prosthesis might best activate these cells by way of electrical stimulation.

Whole-cell patch clamp recordings were made in explanted retinal wholemount preparations from normally-sighted rats. Stimulating electrodes were fabricated from nitrogen-doped ultra-nanocrystalline diamond (N-UNCD) and placed on the epiretinal surface, adjacent to the cell soma. Electrical stimuli were delivered against a distant monopolar return electrode. Using rectangular, biphasic constant current waveforms as employed by modern retinal prostheses, I examined which waveform parameters had the greatest effect on RGC activation thresholds. In a second set of experiments intracellular current injection was employed to assess the effectiveness of sinusoidal current waveforms in selectively activating different RGC subsets. These recordings were used to validate a biophysical model of RGC activation. In all cases, recorded cells were identified and classified based on 3D confocal reconstruction of their morphology.

Electrodes fabricated from N-UNCD were able to electrically activate RGCs while remaining well within the electrochemical limits of the material. They were found to exhibit high electrochemical stability and were resistant to morphological and electrochemical changes over one week of continuous pulsing at charge injection limits.

Retinal ganglion cells invariably favoured cathodic-first biphasic current pulses of short first-phase duration, with a small interphase interval. The majority of cells (63%) were most sensitive to a highly asymmetric waveform: a short-cathodic phase followed by a longer duration, lower amplitude anodic phase. Using the optimal interphase interval led to median charge savings of 14% compared to the charge required in the absence of any inter-phase interval. Optimising phase duration resulted in median charge savings of 22%.

All RGCs became desensitised to repetitive electrical stimulation. The efficacy of a given stimulus delivered repeatedly decreased after the first stimulus, stabilising at a lower efficacy by the thirtieth pulse. This asymptotic efficacy decreased with increasing stimulus frequency. Cells with smaller somas and

dendritic fields were better able to sustain repetitive activation at high frequency.

Intracellular sinusoidal stimulation was used to demonstrate that certain RGC subsets, defined on the basis of morphological type, stratification, and size, were more responsive to high frequency stimulation. Simulated RGC responses were validated by experimental data, which confirmed that ON cell responses were heavily suppressed by stimulus frequencies of 20 Hz and higher. OFF cells, on the other hand, were able to sustain repetitive activation over all tested frequencies. Additional simulations suggest this difference may be plausibly attributed to the presence of low-voltage-activated calcium channels in OFF but not ON RGCs.

The results of my work demonstrate that (a) N-UNCD is a suitable material for retinal prosthesis applications; (b) a careful choice of electrical waveform parameters can significantly improve prosthesis efficacy; and (c) it may be possible to bias neural activation for certain RGC populations by varying the frequency of stimulation.

"I can't write five words but that I change seven."

Dorothy Parker

Contents

Chapter 1

The Retina

The visual system is arguably the most complex of the sensory systems. Vision allows the individual to construct a representation of the world from light and facilitates the perception and interpretation of the visual scene. Light entering the eye (fig. 1.1) is projected onto the retina, a photosensitive organ that represents the earliest stage of the visual system. The retina converts incident light into electrical signals, which are then conducted to the brain via the optic nerve. An impressive amount of processing takes place before visual stimulation of the retina can be translated into signals that are understood by later neural processing stages. I briefly review the general function of the retina in this chapter.

Although the experimental animal used throughout this thesis is the rat (*Rattus norvegicus*), the research was conducted to facilitate the development of visual prosthetic devices for humans. It is, therefore, necessary to describe the retina in a comparative fashion, comparing several animal species, including rats and primates.

1.1 Anatomy and physiology

The retina is a thin film of tissue lining the inner wall of the eye. It contains five broad classes of neurons (Kolb et al., 2007), which are organized into three cellular (nuclear) layers and separated by two synaptic (plexiform) layers (fig. 1.2). Photoreceptors are housed in the outer nuclear layer (ONL) and serve to detect and signal the presence of light in the visual field. Horizontal, bipolar and amacrine cells situated in the inner nuclear layer (INL)

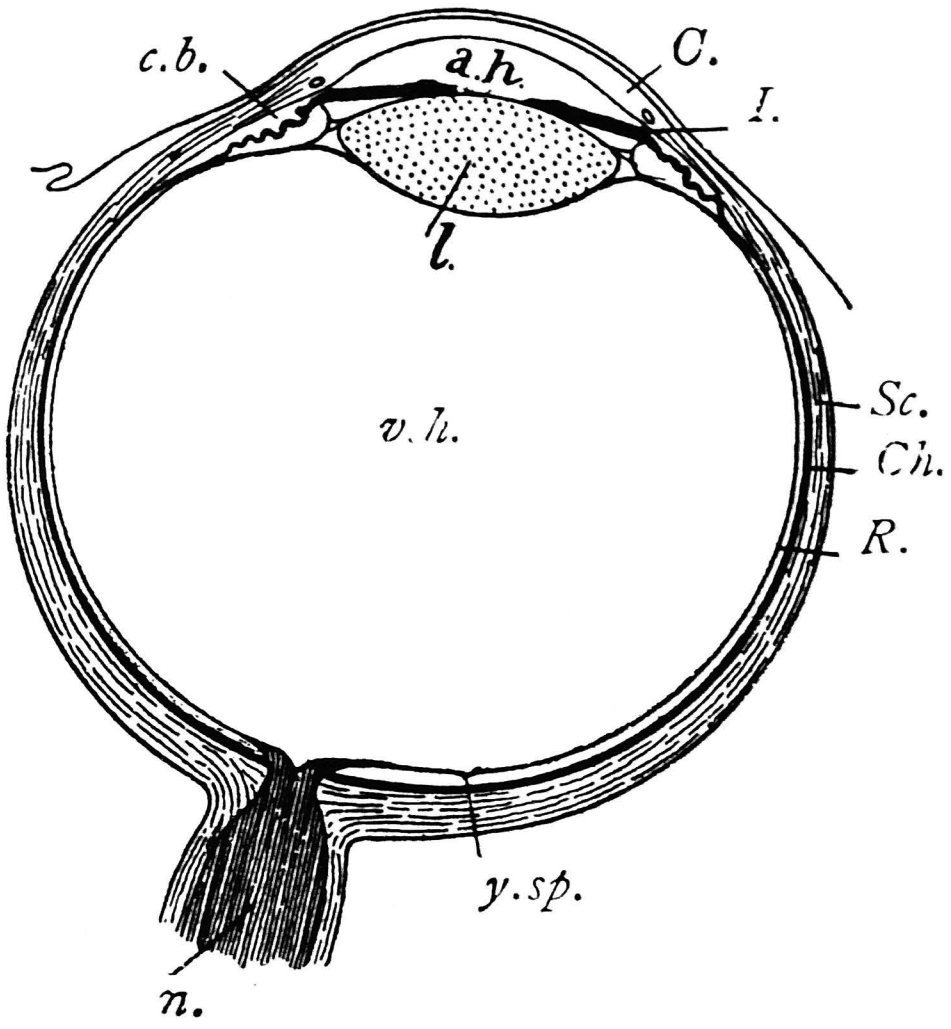

Figure 1.1. Schematic of the human eye. *R.*, retina; *Ch.*, choroid; *C.*, cornea; *a.h.*, aqueous humour; *Sc.*, sclera; *n.*, optic nerve; *l.*, lens; *I.*, iris; *v.h.*, vitreous humour; *y.s.*, yellow spot, or macula lutea. Taken from Thomson (1916). Source URL: http://etc.usf.edu/clipart.

have numerous roles and are responsible for maintaining the visual system's sensitivity to visual contrast of the incoming image, among other things. The ganglion cell layer represents the output of the retina in which ganglion cells transmit information about retinal stimulation to the brain through their axons, which pass through the optic disc and leave the eye to form the optic nerve. The primate retina is home to multiple subtypes of each neuron class with at least two types of horizontal cell, 12 types of bipolar cell, 29 types of amacrine cell and 10–15 types of retinal ganglion cell (Masland, 2001; Wässle, 2004).

The retinae of human and non-human primates share much in common, including the morphology and organization of retinal circuitry, and the processing of neural activity through several parallel pathways (Dacey, 1993; Masland, 2001; Wässle, 2004). In the following sections, some key features of the primate visual system will be discussed, with particular emphasis on the ganglion cells of the retina.

1.1.1 Photoreceptors

Light must traverse the cornea, aqueous humour, lens, vitreous humour, and a great deal of retinal tissue before it can be absorbed by the photoreceptors (Kolb et al., 2007). The transduction of light takes place in the outermost retinal layer where photons are absorbed by the outer segments of rods and cones, the two classic types of photoreceptor cell found in the primate retina. Rods are highly sensitive to light intensity and mediate vision in dim light, but saturate at regular daylight intensities. They consequently play little part in visual processing during the day. Conversely, cones are responsible for colour vision and can operate over a wide range of bright light. They function poorly in dim light. The distribution of rods and cones varies greatly over the retinal surface and is nowhere more conspicuous than in the *fovea*, a small, central region of the macula, the latter being the yellow-coloured central retinal region that is protected from sun damage by luten (Schalch, 1992). The fovea has a densely-packed cone arrangement and few rods. Only cones populate the very centre of the fovea in a region known as the *foveola*. Here, the centre-to-centre spacing of cones is smallest. Together with the focal length f of the eye, the cone spacing s determines the smallest visual angle ($\Phi = s/f$) that can be resolved (Mather, 2009) and therefore underlies the anatomical limit for visual acuity (Curcio et al., 1990). As distance from the fovea increases, cone photoreceptor density falls sharply from 199,000 cones per square millimetre to less than 16,000 cones/mm^2 in the periphery (Curcio et al., 1990) and central vision gives way to lower-resolution peripheral vision.

1.1.2 Midget and parasol pathways

Within the outer plexiform layer (OPL) of the mammalian retina, photoreceptors synapse with bipolar cells and receive inhibitory feedback from horizontal cells. Bipolar cells are classified as either rod bipolar or cone bipolar cells corresponding to the type of photoreceptor that supplies their input. Most cone bipolar cells of the primate retina receive input from between five and ten cones (Wässle, 2004). Bipolar cells in turn synapse with retinal ganglion cells and are laterally inhibited by amacrine cells within the inner plexiform layer (IPL). It follows that signals generated by a given photoreceptor can traverse the neural network and reach the ganglion cell layer in a multitude of ways.

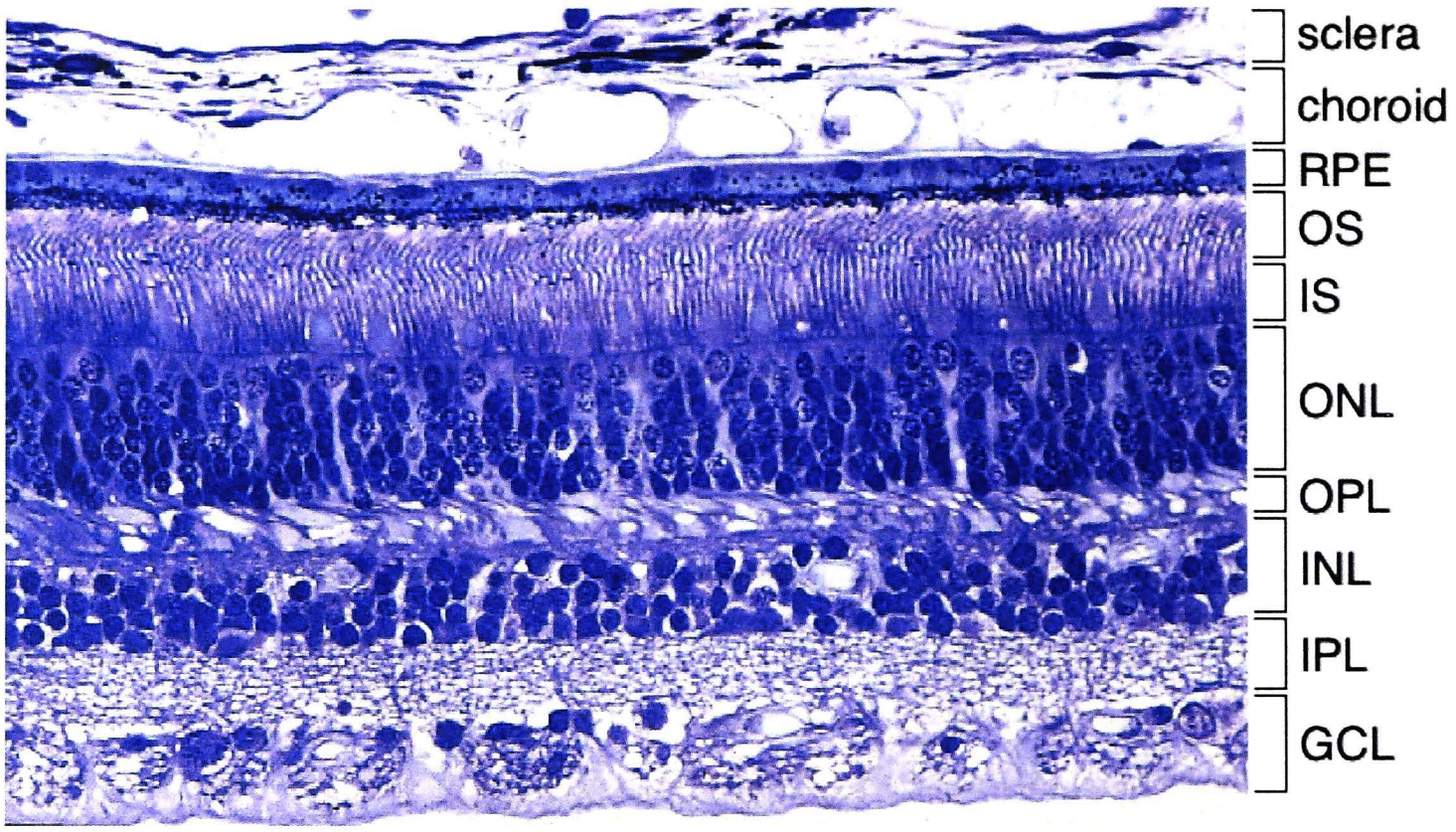

Figure 1.2. A transverse section of the retina. *RPE*, retinal pigment epithelium; *OS*, outer segments; *IS*, inner segments; *ONL*, outer nuclear layer; *OPL*, outer plexiform layer; *INL*, inner nuclear layer; *IPL*, inner plexiform layer; *GCL*, ganglion cell layer. Image from the Human Retina Teaching Set, Scheie Eye Institute, University of Pennsylvania.

A ganglion cell outside of the fovea generally synapses with a large number of cells in the inner nuclear layer, which in turn receive input from many photoreceptors. Such a cell is said to have a large *receptive field*. This term was first coined by Hartline (1938) to describe the surface area of the retina that responds to light stimulation with an increase in neural activity. As cellular density in the retina increases, receptive field size decreases and is smallest for cells located in the fovea (fig. 1.3). One particular type of foveal ganglion cell, the midget ganglion cell, receives input from a single (midget) bipolar cell, which itself receives input from a single cone. Midget ganglion cells constitute around 70% of the total ganglion cell population in the primate retina (Masland, 2001). The *midget pathway* (cone → midget bipolar → midget ganglion → brain) enables the transmission of fine spatial detail and underlies high visual acuity in primates.

The *parasol pathway* provides another major source of input to the visual system. Parasol ganglion cells make up 8% of all ganglion cells in the primate (Masland, 2001) and are thought to convey achromatic information concerning movement and luminance (Dacey and Petersen, 1992). The importance of these two pathways is highlighted by studies that investigate the effect of lesions on visual task performance of monkeys. When cells of the midget

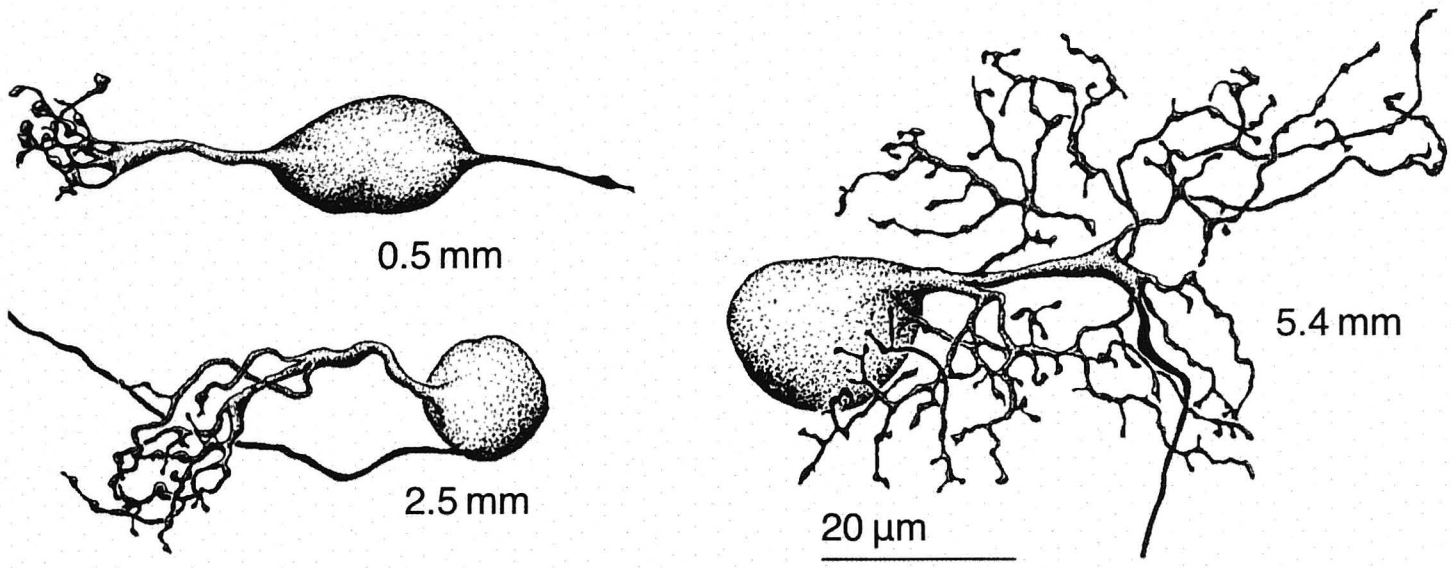

Figure 1.3. Examples of midget ganglion cell morphology for varying eccentricity, indicated next to each cell. Dendritic density decreases and field size increases with distance from the central retina. Modified from Dacey (1993).

pathway are destroyed, tasks such as pattern detection and colour discrimination are severely compromised (Schiller et al., 1990), while lesions of the parasol pathway result in a profound reduction in sensitivity to motion and flicker perception (Merigan and Eskin, 1986; Merigan et al., 1991). Lesions of both pathways result in a near-complete loss of vision (Schiller and Logothetis, 1990).

The midget and parasol ganglion cell classes of the primate together account for a great deal of visual information leaving the retina. Certain neural properties allow each class to handle different aspects of visual processing (Schiller and Logothetis, 1990; Schiller et al., 1990; Merigan et al., 1991). The large receptive fields of parasol cells are generated as a result of their extensive dendritic field size and so can integrate information over a larger area of the visual field, assisting with movement detection. The relatively small dendritic fields of the midget ganglion cell subtypes are suited for discrimination of fine spatial detail, forming a mosaic that evenly tiles the retina (Dacey, 1993; Field et al., 2007, 2010).

1.1.3 ON and OFF pathways

In most mammalian species, the great majority of retinal ganglion cells can be grouped into two distinct categories according to certain functional and morphological properties of their receptive fields (Wässle and Boycott, 1991). Kuffler (1953) discovered that receptive fields of ganglion cells in the cat have a specific spatial structure, characterised by a circular *centre* that responds

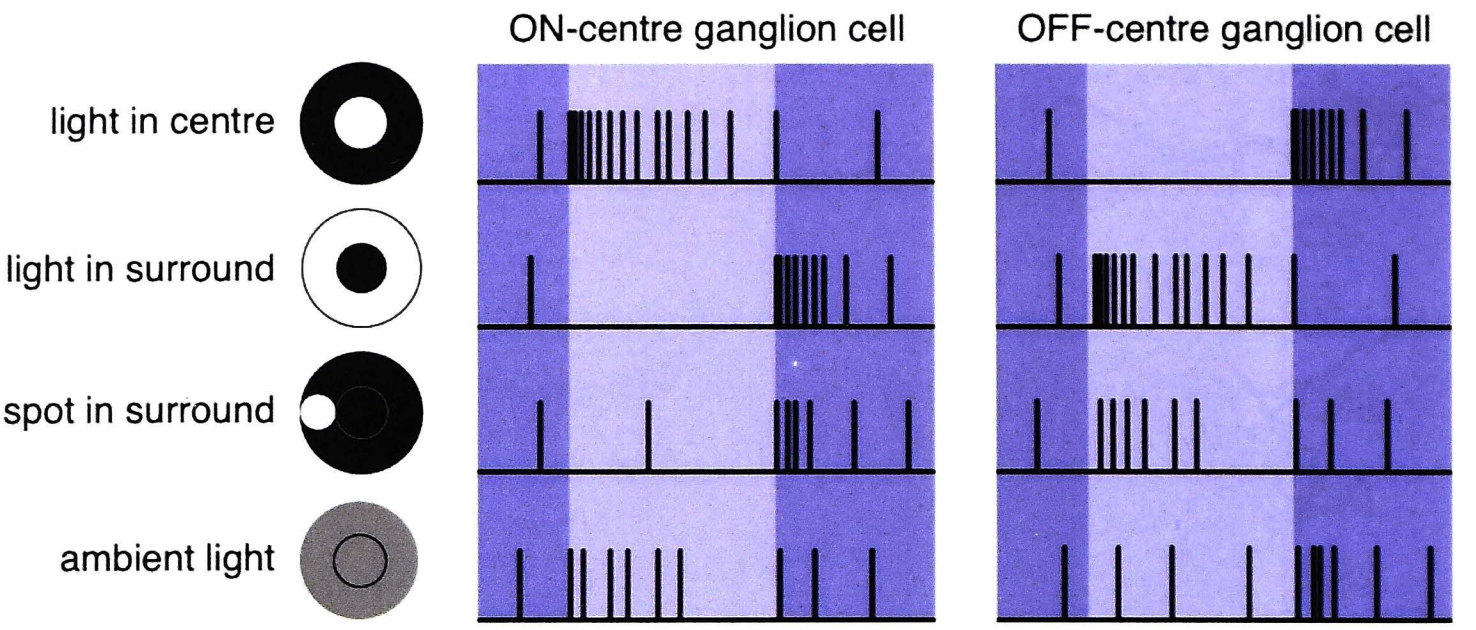

Figure 1.4. The responses of ON and OFF retinal ganglion cells to selective stimulation of their visual fields. Light shading indicates the duration of the visual stimulus. Adapted from Purves (2001).

to either light increments (cells of this nature are termed *ON cells*) or decrements (*OFF cells*), and an antagonistic annular *surround* that suppresses neural activity when stimulated by the centre's preferred light polarity (fig. 1.4). These different response properties are associated with spatially distinct stratification patterns within the inner plexiform layer, where OFF ganglion cell dendrites make synaptic contact with OFF bipolar cell axons in sublamina a, and ON ganglion cells synapse with ON bipolar cells in sublamina b (Nelson et al., 1978). Monostratified ON and OFF ganglion cells develop from bistratified retinal ganglion cells as the postnatal retina matures with visual experience (Maslim et al., 1986; Tian and Copenhagen, 2003; Chalupa and Günhan, 2004). It has since been demonstrated that midget ganglion cell dendrites are similarly organized (Field et al., 2010). The flow of neural activity through these parallel *ON and OFF pathways* underlies feature detection and enables the retina to extract the boundaries between objects revealed by the contrast between relatively bright ridges and neighbouring shadows in a typically structured visual scene (Nelson and Kolb, 2003).

The centre-surround receptive field structure of bipolar and ganglion cells arises from lateral interactions with horizontal cells. These cells integrate input from multiple photoreceptors and respond to excitation of a central photoreceptor by inhibiting neural activity in all photoreceptors that synapse with the horizontal cell. The functional coupling of an excitatory photoreceptor response with this concentric, inhibitory horizontal cell network grants centre-surround antagonism to the bipolar cells that receive input from these photoreceptors (Werblin and Dowling, 1969; Verweij et al., 2003). In effect, the

function of horizontal cells is to measure ambient light intensity and subtract it from localised neural activity, thus accentuating changes in local luminance.

A retinal ganglion cell encodes its output using a sequence of electrical 'spikes' known as *action potentials*. By varying the rate at which these signals are delivered, a ganglion cell can convey information about excitatory or inhibitory stimulation through the optic nerve to the next visual processing stage in the brain. The action potential and the mechanism by which they are generated are overviewed in a later section.

1.1.4 RGC classification

Over the last few decades, studies in the cat retina have given rise to an assortment of retinal ganglion cell classification schemes. Enroth-Cugell and Robson (1966) discovered that for certain cell types, the neural activity elicited by decreases in illumination over one half of the receptive field could be almost completely nullified by simultaneous illumination increases over the other half of the receptive field. These *X cells* therefore integrate their receptive field inputs in a linear fashion, and have small receptive field sizes. Conversely, *Y cells* have large receptive fields and have highly nonlinear receptive field summation where, for instance, both brightness polarities lead to excitatory responses. The X cells are estimated to constitute 35–55% of all ganglion cells in the cat retina, and are most sensitive to fine spatial detail. Y cells comprise 3–5% of the population and respond best to abrupt changes in ambient light (Shapley and Perry, 1986; Troy and Shou, 2002). While the precise role of X and Y cells in vision is not yet clear, their characteristic axonal projection patterns suggest that each type constitutes an independent information pathway (Troy and Shou, 2002).

Cleland et al. (1971) expanded upon the X/Y dichotomy with their *sustained-transient* scheme, which classifies a cell based on its response to an assortment of visual tests. Both transient and sustained cell types showed a rapid increase in activity in response to stimulation with a small target spot, but transient cell spiking (as their name suggests) quickly returned to the baseline level maintained before stimulus onset (fig. 1.5). On the other hand, the level of activity in sustained cells remained significantly higher than at rest, for the duration of the stimulus. When the spot was removed, spiking activity was heavily suppressed before gradually recovering with time. The sustained-transient dichotomy groups cells by their response to (a) steady-state contrast,

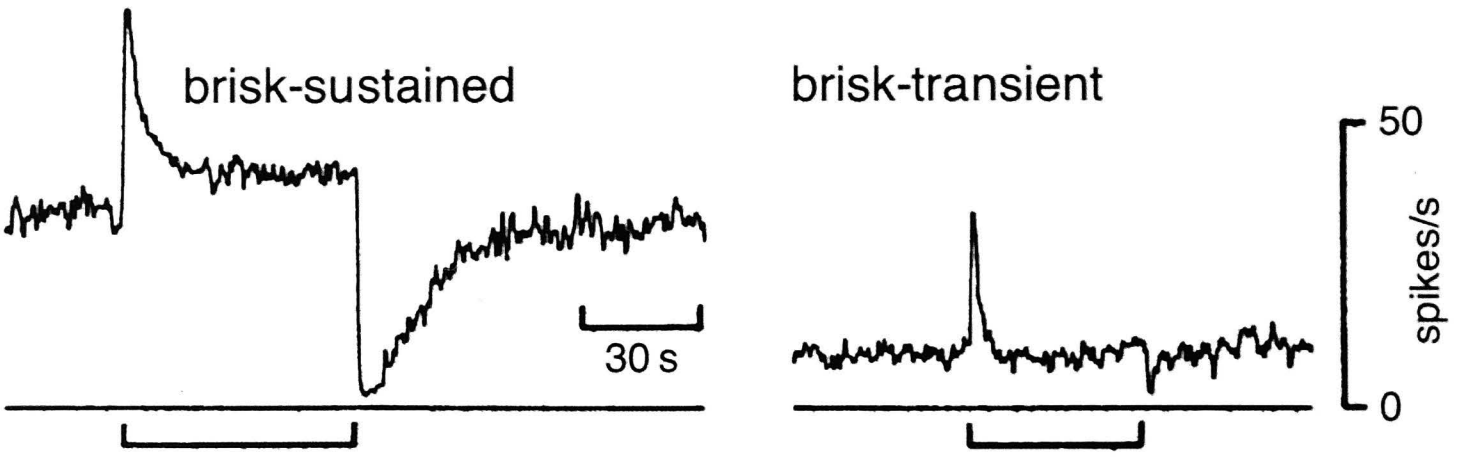

Figure 1.5. The responses of brisk-sustained and brisk-transient retinal ganglion cells to a standing contrast stimulus. Horizontal brackets indicate stimulus duration. Adapted from Cleland et al. (1971).

(b) grating patterns, (c) visual target size and speed, and (d) a peripheral stimulus, and accounts for almost all retinal ganglion cells. Cleland and Levick (1974) went on to demonstrate that cells could also be grouped according to fast (*brisk*) or slow (*sluggish*) axonal conduction velocity. Cells with the fastest conduction velocities were of the brisk-transient class, with brisk-sustained velocities being slower and sluggish velocities the slowest. X cells were found to correspond with brisk-sustained cells, and brisk-transient cells with Y cells.

The term *W cell* has become used to describe cells whose physiology is neither X- nor Y-like. This is somewhat regrettable, given that these cells exhibit a wide variety of physiological properites and represent 45–60% of the ganglion cell population (Troy and Shou, 2002). W cells collectively refer to the sluggish cell class in addition to the minority (8%) of ganglion cells that do not have a centre-surround receptive field structure (Cleland and Levick, 1974; Levick, 1975).

Work by Boycott and Wässle (1974) identified α, β, and γ *cells* as three distinct morphological cell types within the ganglion cell population. α cells have the largest dendritic fields, the largest somas and the thickest axons of any ganglion cell type in the cat retina, and are conserved in the primate and a wide range of other mammalian species, including the rabbit, horse, ox, and rat (Peichl, 1991). The idea that the respective morphological correlates of the physiological Y- and X-types are the α- and β-types was suggested by the authors of the study and later substantiated by several studies (Cleland and Levick, 1974; Saito, 1983; Stanford and Murray Sherman, 1984; Stanford, 1987). An analogous connection between the anatomical midget and parasol ganglion cell dichotomy and the functional *parvocellular cell* (P cell) and *magnocellular* (M cell) dichotomy of the primate visual system has also been

validated (Boycott and Wässle, 1991). P and M cells are named after the distinct neural layers of the lateral geniculate nucleus (LGN) in which they reside. The LGN is the recipient of 90% of the ganglion cell output from the macaque retina (Perry et al., 1984). Parvocellular neurons, implicated in colour vision and transmission of fine spatial detail, receive their input from midget cells. Magnocellular neurons, with their good contrast sensitivity and ability to resolve high temporal frequency information, synapse with parasol cells (Leventhal et al., 1981; Michael, 1988). As an unfortunate consequence of different groups conducting the experiments, the field is left with the uncomfortable terminology that retinal M(idget) cells feed into geniculate P(arvocellular) cells and retinal P(arasol) cells feed into geniculate M(agnocellular) cells.

How well do the α-Y and β-X cells of the cat correspond to the midget-P and parasol-M ganglion cells of the primate? The parasol cell has the thickest axon and largest soma of the ganglion cell population and so appears to be an ideal candidate for matching the morphological α-type. Both M- and Y-types possess achromatic light responses, have high contrast sensitivity and are specialized for motion detection (Dacey and Petersen, 1992; Saito, 1983; Kaplan and Benardete, 2001) and so their physiological properties too, seem well-matched. There is disagreement, however, as to whether the M cells of primate geniculate possess the classic integrative properties of the Y-type receptive field found in the cat (Petrusca et al., 2007; Crook et al., 2008). Also unclear is the degree to which parasol cells project their axons to the superior colliculus (Perry and Cowey, 1984; Rodieck and Watanabe, 1993), a sub-cortical region that is known to receive substantial input from the α-Y cell population in cats (Wässle and Illing, 1980). Additionally, there is evidence that the anatomically similar β and midget ganglion cells, with their relatively small dendritic fields and axonal conduction velocities, are functionally dissimmilar (Shapley and Perry, 1986; Benardete et al., 1992). One theory reviewed by Shapley and Perry (1986) asserts that there are actually two subtypes of M cell, M_X and M_Y, which correspond to X and Y cells.

The visual systems of the cat and primate diverge as a result of the distinct behavioural needs of each species. In the human, the high sampling density offered by the fovea is required to perform everyday tasks that depend on high spatial acuity. There is a similar retinal feature in the cat known as the *area centralis* that contains the highest cone density (Steinberg et al., 1973). Although this density is significantly lower than that of cones in the primate fovea, it works to enhance spatial resolution in low ambient light

(Pasternak et al., 1983). The cat retina is highly sensitive to stimulation under low light conditions (Kang et al., 2009) and is particularly suited to hunting and movement at night. It is therefore important to consider that while the retinal structures of cats and primates share much in the way of morphological cell types and parallel pathways for visual information (Sterling, 1983; Masland, 2001; Wässle, 2004), they are certainly not identical.

1.1.5 The rat retina

It is easy to accept that the visual system of the rat (see Sefton and Dreher 1995 for review) is quite different in function from that of the primate. With its rod-dominated retina, the rat is primarily suited to vision in dim light. As do all non-primates, rats lack a fovea as well as the associated visual acuity, instead relying more on other sensory cues to orient themselves and escape predators in their environment. The rat is, nevertheless, of interest in visual neuroscience research as their retina has the same complement of cone bipolar cells as the primate and cat, and expresses similar diversity to other species in retinal ganglion cell classes (Wässle, 2004).

As was done in the cat, the retinal ganglion cells of the rat have been morphologically classified into three groups, according to soma size (Fukuda, 1977; Perry, 1979; Huxlin and Goodchild, 1997), dendritic field size (Perry, 1979; Huxlin and Goodchild, 1997), branching patterns (Perry, 1979; Huxlin and Goodchild, 1997), and stratification (Huxlin and Goodchild, 1997). In the rat retina, RG_A cells (or simply *A cells*) are the anatomical correlates of the cat alpha cells, with their large somata and dendritic field sizes. RG_B cells have small soma and dendritic field sizes, and RG_C cells have small-medium somata and medium-large dendritic field sizes. Sun et al. (2002) confirm this classification scheme and provide support for another class, RG_D, differentiated by bistratification. Interestingly, a small population of alpha-type ganglion cells (1% of the total ganglion cell population) has been found in the rat and gerbil retinae that exhibit Y-like physiological function and yet are thought to serve some non-visual function (Fite et al., 1999; Luan et al., 2011). Whether the beta cell and other morphological types of the cat have their counterparts in the rat retina remains uncertain.

Retinal ganglion cells in the rat have been shown to possess X- and Y-like properties. In their study, Heine and Passaglia (2011) found that rat ganglion cells too, had brisk and sluggish responses to a spot of light. Most brisk cells

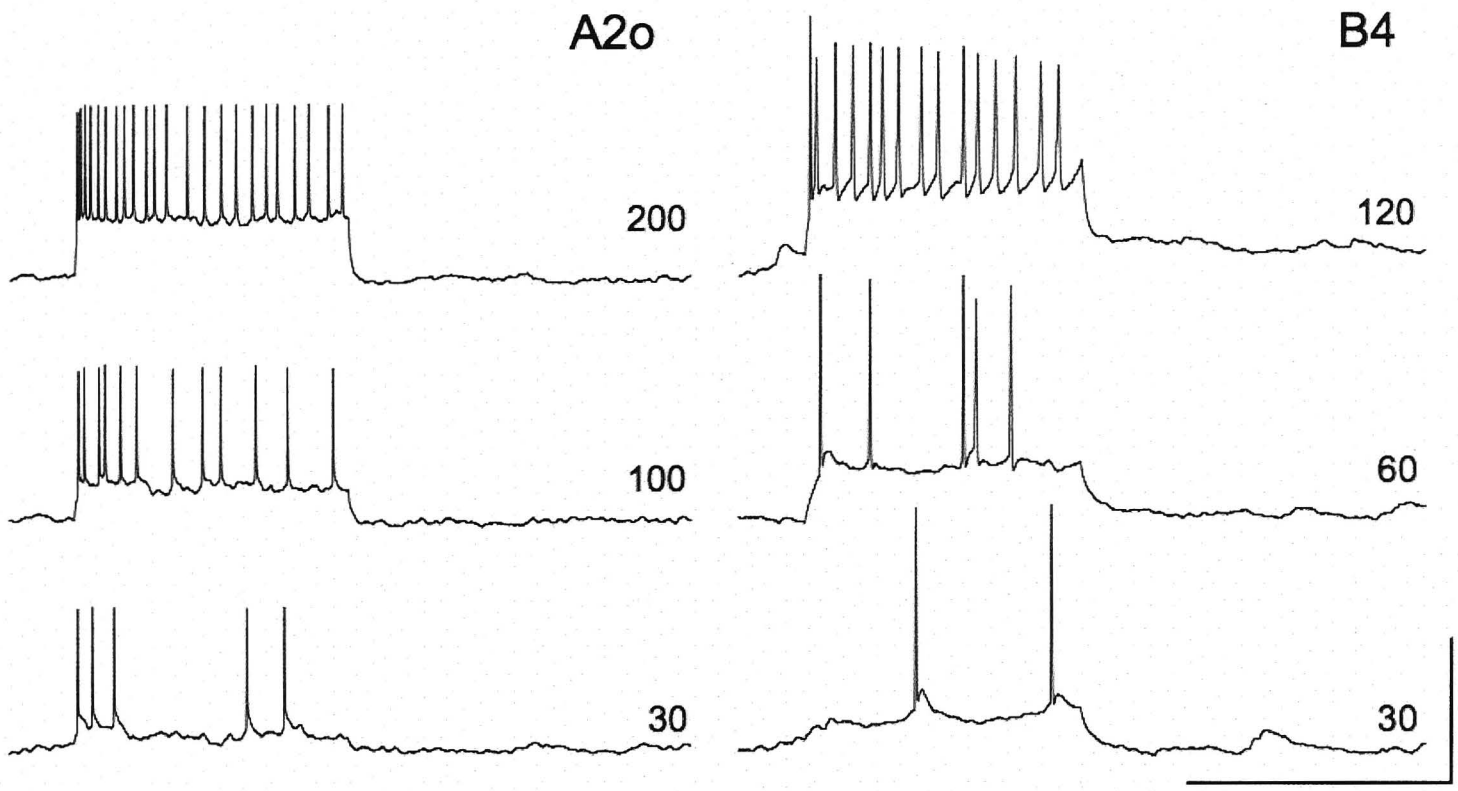

Figure 1.6. Representative spiking patterns for A2 and B4 cells of the rat retina in response to depolarizing current injection. Number next to each trace indicates stimulus amplitude (pA). Vertical and horizontal scale bars represent 50 mV and 400 ms respectively. Adapted from Wong et al. (2012).

also had an antagonistic centre-surround receptive field that performed either linear or non-linear spatial summation. The receptive field sizes of rat brisk-sustained were, however, indistinguishable from those of brisk-transient cells. Given the relatively small receptive fields of the beta cell compared with the alpha cell in the cat, this is suggestive of a functional asymmetry between X cells of the two species. The authors propose that since receptive field size homogeneity is common to several other prey species, their visual systems may be more suited for threat detection, as opposed to spatial discrimination of targets from the visual scene.

The flow of visual information is ultimately shaped by the intrinsic physiological differences between each cell type. With respect to retinal ganglion cells, they include both passive properties (resting potential V_m, membrane input resistance R_m and membrane time constant τ_m, discussed later in this chapter) and active properties, such as maximum firing rate and frequency adaptation. The intrinsic properties for a given cell are largely influenced by its morphological characteristics. It follows that morphologically distinct cell types also have distinct sets of intrinsic properties (O'Brien et al., 2002; Wong et al., 2012). Figure 1.6 features representative spiking patterns for A2 and B4 cells of the rat from the work of Wong et al. (2012), which demonstrate clear differences between the spike width, and maximum and steady-state spiking frequency of each cell type. The A2 cells of the rat were found to have very

similar intrinsic properties to that of the alpha cell in the cat (see O'Brien et al., 2002), while B4 cells were found to be similar to cat zeta cells. On the other hand, there were clear differences between the properties of beta cells and many other cat cells and their supposed correlates in the rat.

In summary, there is much to support the hypothesis that discoveries made in the electrophysiological study of the rat A2 cell can be extrapolated to the alpha cell in the cat and even further, to the parasol/brisk-transient cell of the primate. The intrinsic physiological properties of A2 cells, as well as their morphological characteristics, match those of the alpha cell. Furthermore, there is evidence that the alpha cell is the anatomical and functional equivalent of the parasol cell. Finally, the alpha cell has been found in all investigated mammals to date. All of these findings collectively provide a sound basis for use of the rat retina (especially A2 cells) as a model in prosthetic vision research.

Table 1.1. A comparison of key morphological and electrophysiological properties of the rat A2 and primate parasol ganglion cells. Rat A2 data (○: A2i, ●: A2o) were sourced from Wong et al. (2012). Primate parasol data were taken from Watanabe and Rodieck (1989) (♠), Dacey and Petersen (1992) (◊), and Weber and Harman (2005) (♣). Primate dendritic field diameter was estimated for 12 mm eccentricity.

Property	A2 cell	Parasol cell
Soma diameter (μm)	21 ± 2 ○	20 ± 3 (baboon) ♠
	22 ± 1 ●	17 ± 3 (macaque) ♠
DF diameter (μm)	480 ± 72 ○	353 (human) ◊
	362 ± 26 ●	299 (macaque) ♠
Input resistance (MΩ)	121 ○	22.5 ♣
	98 ●	
Time constant (ms)	11.9 ○	2.7 ♣
	9.5 ●	
Spike width (ms)	1.08 ○	0.43 ♣
	0.85 ●	
Max firing rate (Hz)	165 ○	92.8 ♣
	204 ●	

1.2 Underlying concepts

1.2.1 Neuronal signalling

All cells maintain an electrical potential difference across their membrane. In the absence of stimulation, the unequal ion concentrations between the interior and exterior of a cell give rise to a certain *resting membrane potential.* The response of a sensory neuron to excitation involves a transient change in this membrane potential, which depends on the biochemical properties of the membrane and the synaptic connections made by the neuron. The conduction of electrical impulses across a cellular membrane allows for signalling between neurons and forms the basis for information coding and transmission in the central nervous system.

Each of the five major retinal neuron types is receptive to stimulation. Photoreceptors, horizontal, and bipolar cells respond to light with a sustained *graded potential*, a change in membrane potential proportional in amplitude to the intensity of the stimulus, which persists for the duration of the stimulus. These signals are passively conducted along the cellular membrane. Since neurons are poor conductors of charge, graded potentials decay rapidly and are susceptible to noise and distortion as they propagate along the membrane. The processes of neurons that employ graded potentials are short enough, however, that intercellular messaging of this nature is effective.

An amacrine or ganglion cell that receives enough excitation will respond with another kind of signal characterized by an abrupt, short-lived fluctuation in membrane potential of fixed amplitude and shape – the *action potential*, or *spike*. Stronger excitation beyond the stimulation threshold will result in multiple action potentials, with the strength of the stimulus encoded by the rate of spiking. These signals are distinguished by several phases (fig. 1.7). During the *rising phase*, the membrane rapidly depolarizes until it reaches a certain peak voltage, after which it begins to repolarize over the *hyperpolarizing phase.* In some cases the membrane potential will then fall below the initial membrane potential in the *undershoot phase* before returning to the resting potential. An action potential will excite and subsequently trigger another action potential in the next membrane region to be reached as it propagates over the cell. This regenerative mechanism allows the signal to travel a great distance without

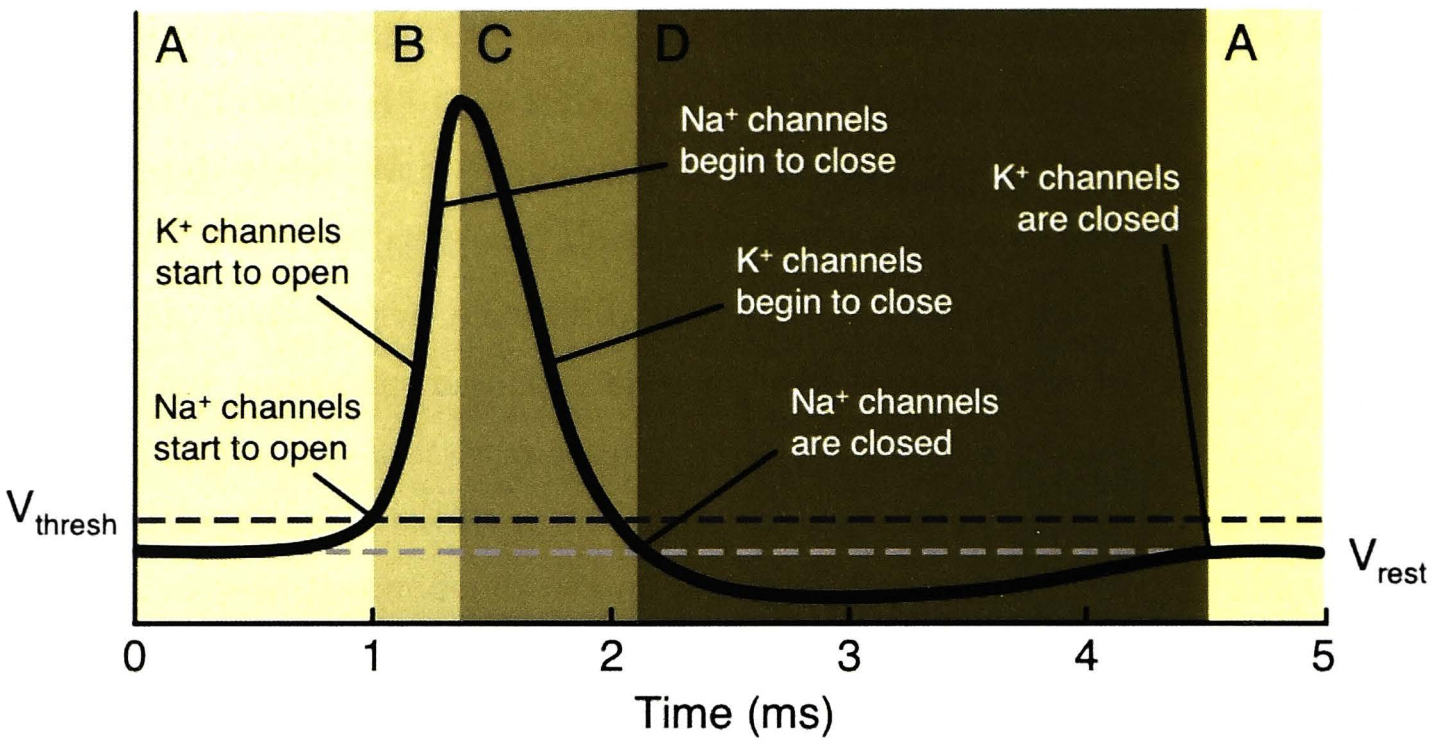

Figure 1.7. Phases of the typical action potential. When sufficiently stimulated, the membrane rapidly becomes highly permeable to Na^+ and leaves the resting state (A) to enter the rising phase (B). As the action potential reaches its peak, K^+ channels begin to open. Soon after Na^+ channels begin to close, the action potential enters the hyperpolarizing phase (C). Conductance of K^+ begins to fall and the membrane reaches the original resting potential V_{rest} when Na^+ channels are closed. The membrane potential continues to hyperpolarize and stays in the undershoot phase (D) as the remaining active K^+ channels close before finally returning to the resting potential.

suffering attenuation and excessive noise. Action potentials are therefore essential in transmitting information about the visual world to the brain through the long fibres of the optic nerve.

Action potentials result from rapid changes in the flow of certain ions across the cellular membrane. The permeability of the membrane to these ions is regulated by *ion channels*, which permit ion flow in response to stimulation (for review, see Armstrong and Hille 1998). Ion channels can be classified by the type of ions they allow passage (e.g. sodium ions), or by the mechanism which leads to their activation. *Voltage-gated ion channels*, activated by changes in membrane potential, allow neurons to generate and conduct electrical signals. The action potential was first described as a sequence of changes in sodium (Na^+) and potassium (K^+) conductance (see fig. 1.7) by Hodgkin and Huxley (1952) after a series of experiments in the squid giant axon. During the rising phase, Na^+ channels open and the membrane becomes extremely permeable to sodium. As there is a higher concentration of sodium within the extracellular medium, the ions flow inward and depolarize the cell. The increase in Na^+ permeability is paired with a slower increase in permeability to K^+, which works to repolarize the cell due to there being a lower concentration

of extracellular potassium. The action potential ends when the membrane permeability of sodium and potassium ions return to their resting levels. Ion channels cycle through different states over the course of stimulation. When excited, an ion channel opens and enters the 'activated' state. After allowing a certain number of ions to traverse the membrane, the channel closes (i.e. becomes 'desensitised') and cannot be reactivated until after returning to the former 'resting' state. The duration required for a sodium or potassium channel to make the desensitised $\rightarrow$ resting transition largely contributes to the cell's *refractory period*, which limits the rate at which a cell can respond to sustained stimulation.

1.2.2 The patch-clamp technique

To measure ionic currents as they did in their experiments, Hodgkin and Huxley developed an experimental technique known as the *voltage-clamp*, first invented by Cole in the 1940s (Bear et al., 2006). In a voltage-clamp experiment, the membrane potential is controlled and the transmembrane current required to maintain that potential is measured. Here, the flow of current is proportional to the number of active ionic channels. Further refinement of the voltage-clamp by Neher and Sakmann (1976) resulted in the *patch-clamp* technique, which made possible the recording of currents flowing through a single ion channel (Hamill et al., 1981) and thereby allowed the action potential mechanism proposed by Hodgkin and Huxley to be directly tested.

Patch-clamp recordings are made using an electrode sheathed by a glass micropipette with an extremely fine (usually not much more than a micrometer) open tip diameter. In the 'cell-attached' configuration, the micropipette tip is brought close to the surface of the cell membrane and suction is applied to establish a tight pipette-membrane seal of high electrical resistance. In addition to improving the mechanical stability of the recording, this 'gigaseal' works to electrically isolate the ion channel of interest, reducing the corruptive influence of noise on measurement. From this recording configuration, a *whole-cell* patch-clamp recording can be established by rupturing the gigaseal to gain electrical access to the intracellular medium (fig. 1.8). Whole-cell recordings typically employ a wider pipette tip (1–2 μm) and enable the measurement of electrical activity over the entire cell membrane. Although the original patch-clamp technique was developed to observe current, the experimental apparatus

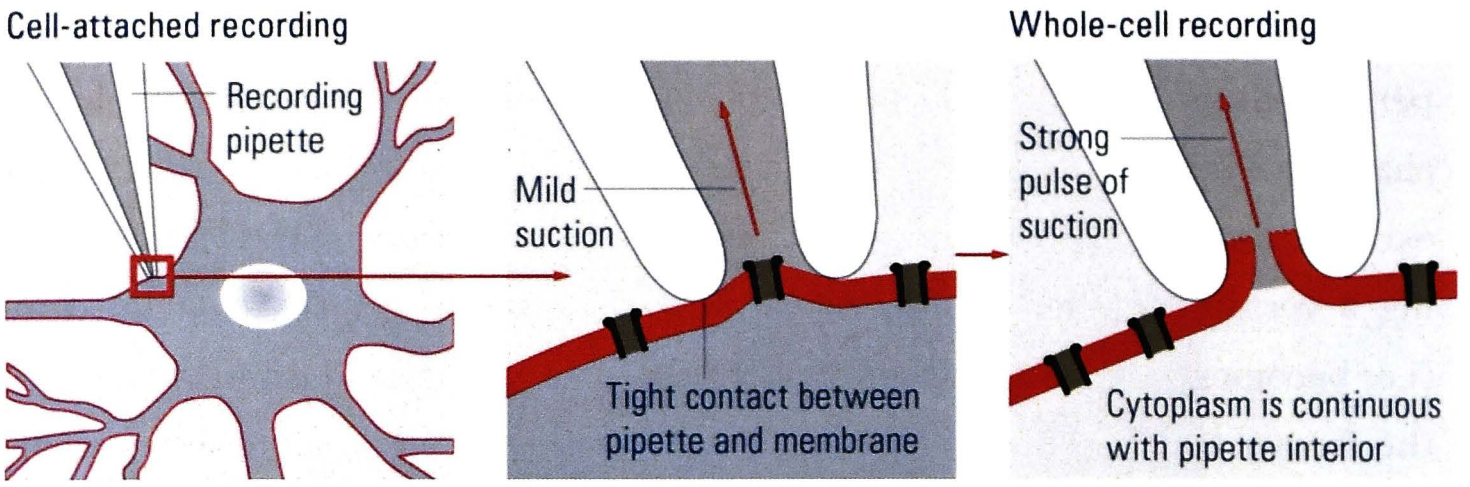

Figure 1.8. Two patch-clamp recording configurations. Cell-attached: suction is applied to gain a tight seal between the pipette and membrane. Whole-cell: a strong pulse of suction ruptures the membrane to gain access to the cytoplasm. Modified from Veitinger (2011).

can be modified to measure changes in membrane potential in response to current injection.

The rupture of the gigaseal at the start of a whole-cell recording initiates the gradual replacement of the intracellular medium with the internal solution of the pipette. The solution is usually made to approximate the cytoplasm of the cell so as to extend the recording period before inevitable cell death. Typical internal solutions are potassium- and chloride-rich, made resistant to changes in pH, and are carefully controlled for osmolarity. Similarly, the extracellular solution is composed to replicate the natural environment of the neuron *in vivo*. A careful selection of both solutions can support neural function in explanted tissue hours after isolation.

1.2.3 Electrical stimulation

Intracellular recordings have been used extensively to characterise the function of retinal neurons and their circuitry (e.g. Kolb and Nelson, 1984). Since the primary language of neurons is electrical, they can be made to 'talk' by any stimulus that results in sufficient membrane depolarization. The electrical stimulation of excitable tissue, together with the recording of the biological response, forms the basis for electrophysiological research.

The electrode used to make a whole-cell current-clamp recording can be used to deliver *intracellular electrical stimuli*. In this configuration, current is injected through the recording electrode and flows through the cytoplasm before passing through the membrane and finding signal ground, positioned relatively far away from the cell within the extracellular solution. A simplified electrical

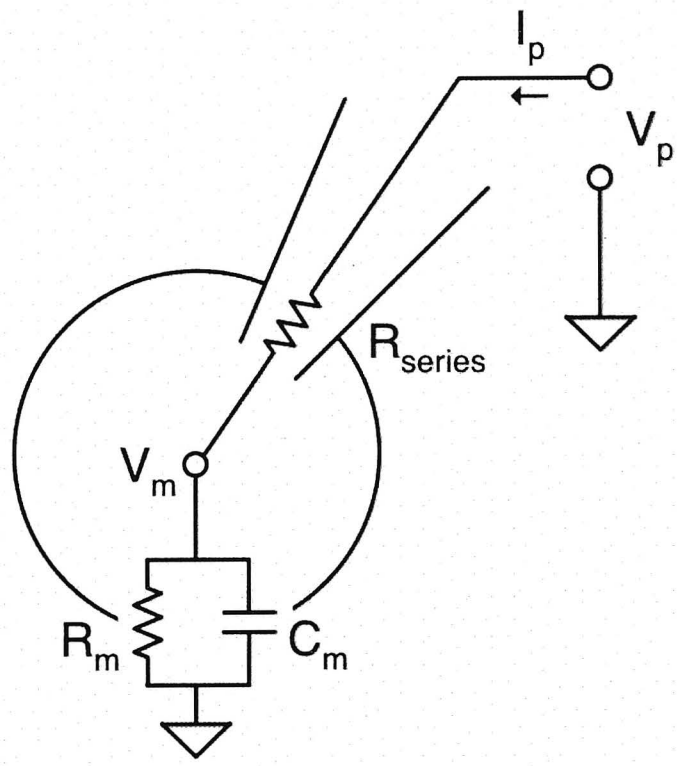

Figure 1.9. Simplified equivalent circuit showing important circuit elements for whole-cell recording and intracellular electrical stimulation.

representation of this setup is shown in fig. 1.9. The injected current I_p encounters pipette resistance R_p (originating from the small size of the pipette tip) and access resistance R_a (representing the impedance of the fractured gigaseal, which is negligible for a high quality recording). R_p and R_a are together referred to as the 'series resistance'. The flow of current through this resistance leads to a proportional drop in potential such that the measured potential V_p is not equal to the desired membrane potential V_m. After compensating for the series resistance, the membrane potential may be measured across the (relatively large) membrane resistance R_m. The effective parallel coupling of the membrane capacitance C_m with R_{series} serves to delay changes in membrane potential (governed by the membrane time constant $\tau_m = R_m \cdot C_m$), and impacts upon the response dynamics of the cell to subthreshold stimulation.

In the case of *extracellular electrical stimulation*, at least one additional stimulating electrode is placed within the extracellular medium, often with an accompanying ground electrode. An action potential can result from the activation of cell body, axon, or any anatomical site that features voltage-gated ion channels, each with their own sensitivity to electrical stimulation (e.g. Fried et al., 2009). It is likely that the injection of current into excitable tissue leads to widespread activation of multiple neuronal populations at varying distances from the stimulating apparatus (Ranck Jr, 1975; Joucla et al., 2012).

The generation of neural activity through extracellular electrical stimulation is primarily influenced by (a) the geometry of the stimulating electrode, (b) the position of the stimulating apparatus relative to excitable neuron elements,

(c) the arrangement of excitable elements within the electric field, and (d) the electrical stimulus itself (see Ranck Jr 1975 and Durand 2006 for details). In a homogenous cell population, the neurons closest to the stimulating electrode tend to be most easily stimulated. Recent work by Joucla et al. (2012) demonstrate that the relationship between electrode-to-neuron distance and stimulus threshold is quadratic for distances of less than 250 µm and essentally constant for distances larger than 1 mm. The orientation of the axon within the evoked electric field is also of importance, as the longitudinal component of the electric field is responsible for fibre excitation (e.g. Basser and Roth, 2000).

Since the electrical field largely determines the distribution of active ion channels over the cell membrane, it is clear that the stimulus waveform used to excite a neuron has a profound effect on neural activation. An *anodic* current, flowing from a stimulating monopolar electrode placed in close proximity with a neuron fibre, out to a distant return electrode, will locally hyperpolarize the membrane and depolarize neighbouring regions. The same current flowing into the stimulating electrode (*cathodic* current) generates an identical potential distribution of reversed polarity. The distributions associated with each stimulus polarity suggest that less cathodic current is required to stimulate a local axon, and this has been validated experimentally by numerous studies throughout the literature as reviewed by Durand (2006) and Rattay et al. (2012). In later sections, this thesis will investigate how manipulation of additional waveform parameters affects the efficacy of a rectangular, biphasic electrical stimulus.

Chapter 2

Prosthetic Vision

We now turn our attention to electrical stimulation of the visual system, and in particular, the retina. Here, I describe the operation of a microelectronic *retinal prosthesis* and how it may be used to grant vision to the blind. Several key issues are discussed, including the viability of electrically stimulating the degenerate retina. The chapter concludes with a brief review of some fundamental principles that underlie the operation of every microelectronic retinal prosthesis.

2.1 Overview

Visual perception involves the translation of light emitted from the outside world into meaningful information about the visual scene. The loss of this sense is associated with restricted mobility and a consequent loss of independence which can have a devastating impact on health and emotional wellbeing. Vision impairment represents a significant global health problem with more than 124 million people experiencing some form of visual loss and a further 37 million people suffering from blindness in 2002 (Taylor et al., 2006).

Vision loss can occur in several different ways. The more common, readily treatable eye conditions involve refractive error, where the lens of the eye does not focus light onto the retina in a precise way – cataracts, for instance, disrupt retinal focus by a clouding of the lens. Eye conditions such as macular degeneration and retinitis pigmentosa (RP) are more serious and destroy the photoreceptors of the retina that detect light and perform the initial processing of visual information. Glaucoma refers to a group of diseases that affect

the retina and optic nerve, compromising the retinal ganglion cells and consequently severing the connection between the retina and the central nervous system.

The function of damaged neural systems can be partially restored by means of a *neural prosthesis* – a medical device used to electrically, chemically or otherwise stimulate excitable tissue. A well-known example is the cochlear implant which bypasses damaged hair cells of the inner ear and stimulates the auditory nerve inside the cochlea to restore a sense of sound to the deaf or hard of hearing. Similarly the visual system left intact by degenerative retinal disorders may be stimulated to restore visual perception in a patient suffering from profound vision loss, granting the patient a sense of *prosthetic vision*. In some cases damaged visual systems may be repaired through therapeutic gene transfer, an experimental technique in which the defective genes responsible for the subject's vision loss are replaced by insertion of a normal gene into a nonspecific location within the genome. A modest improvement in retinal function was observed using this method to treat three patients suffering from Leber's congenital amaurosis, an inherited retinal disease (Maguire et al., 2008). A similar technique was used by Bi et al. (2006) to restore visual responses in mice lacking photoreceptors by conferring light sensitivity to surviving inner retinal neurons through the expression of engineered rhodopsin. Buch et al. (2008) review the viability of gene therapy for the treatment of retinal disorders.

The idea of prosthetic vision has received attention from as early as 1929 when Foerster investigated the effects of electrical stimulation on the occipital lobe of the human cortex (Brindley and Lewin, 1968). This stimulation caused his subject to perceive a small spot of light. Brindley and Lewin referred to this sensation as a *phosphene* and later confirmed the phenomenon in 1968 by implanting an electrode array in a blind patient and stimulating the occipital pole of the right cerebral hemisphere.

Visual neuroprosthesis development is currently being pursued by a number of groups worldwide. The question of where to stimulate the visual system has lead to several different approaches to the problem with each characterised by their mode of stimulation. In addition to visual cortical stimulation, research groups have considered retinal, optic nerve and lateral geniculate nucleus (LGN) stimulation (e.g. Humayun et al., 2003; Brelén et al., 2005; Pezaris

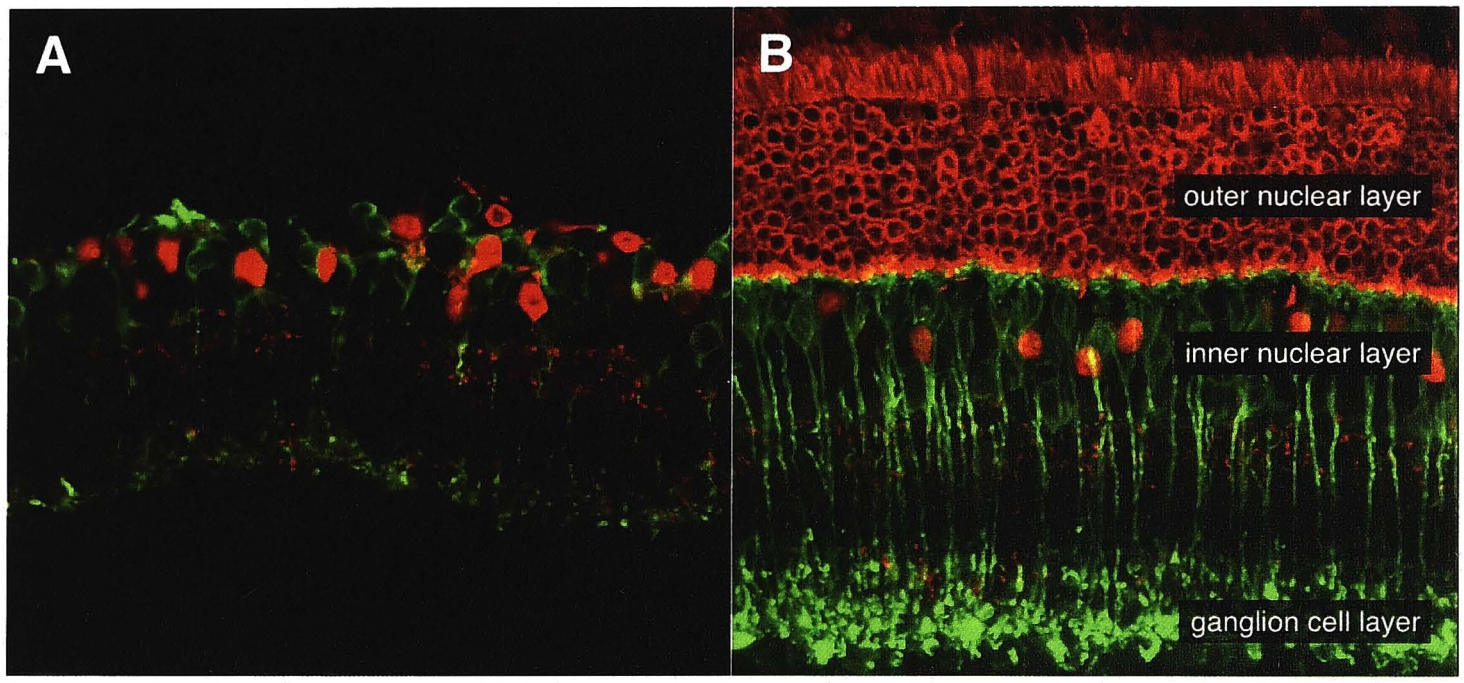

Figure 2.1. Retinal degeneration in the P23H rat, an animal model of retinitis pigmentosa. Panel A shows the retina in the advanced stages of the disease. For comparison, panel B features the healthy rat retina in the same animal before degeneration onset. Images made by Nicolás Cuenca of the Department of Physiology, Genetics and Microbiology at the University of Alicante.

and Reid, 2006). Vision prostheses that target higher stages of the visual system do not need surviving retinal cells to function – they have the potential to help sufferers of a broader range of diseases such as glaucoma and diabetic retinopathy. Nonetheless, the brain surgery required for a cortical or LGN prosthesis is more invasive and dangerous than the eye surgery involved with a retinal implant. Other groups have focused on chemical means of stimulation with the idea of eliciting retinal neural activation through localised neurotransmitter delivery (e.g. Mehenti et al., 2007).

A retinal neuroprosthesis aims to restore visual perception through electrical stimulation of the surviving retina (fig. 2.1). Santos and coworkers (1997) found more than 95% of the outer nuclear layer was lost in cases of severe retinitis pigmentosa when compared with control cases. Despite this, 80% of the inner retina layer and 30% of ganglion cells were preserved. Similarly promising findings were made by Kim et al. (2002) in their analysis of the macula in eyes with disciform age-related macular degeneration – although a 70% reduction in ONL cell number was noted, there were no significant changes to inner nuclear layer and ganglion layer cell counts. These findings suggest that for sufferers of these two eye diseases and their numerous variants, the restoration of sight through replacement of photoreceptor function is quite feasible.

Several broad types of retinal prosthesis are currently in development, with each characterised by the site of intervention (fig. 2.2). The *epiretinal* prosthesis developed by Humayun et al. (2003) stimulates surviving ganglion cells by injecting charge through an array of electrodes implanted at the vitreoretinal interface. This device consists of an external unit that captures an image of the visual scene and converts it into a command sequence and an implanted unit which uses this sequence to drive the electrode array. With the exception of the electrode array, all of the device electronics are kept off the retinal surface in this configuration. Other epiretinal prototypes (e.g. Liu et al., 2000) position the electronics within the vitreous cavity – a fluid-filled space which acts as a heatsink and allows the device to dissipate a significant amount of power (Piyathaisere et al., 2003; Gosalia et al., 2004). The architecture of the Humayun prosthesis allows stimulus parameter adjustments and processing unit upgrades to be made by interfacing with the external components of the device, with no need for additional surgery.

The *subretinal* prosthesis devised by Zrenner et al. (1999) is based on the proposal of replacing photoreceptor function using an array of photodiodes implanted between the outer retina and the retinal pigment epithelium. In this way the residual INL retinal network can be utilised to process electrical signals and elicit visual percepts. The device itself is powered solely by incident light and does not use an external power source. One key advantage this approach has over epiretinal implantation concerns fixation of the device to the retina. Long-term electrode attachment to the retinal surface has been shown to give rise to an assortment of complications including retinal detachment (Walter et al., 2005; Güven et al., 2005), vitreous haemorrhaging (Majji et al., 1999; Rodrigues, 2003) and cataract development (Gerding et al., 2007). Electrodes placed subretinally are supported by the relatively strong natural adherence forces existing between the retinal pigment epithelium and sensory retina and do not usually give rise to such severe surgical problems. These electrodes have the additional advantage of being in close proximity to the next surviving neuron type in the visual processing chain – the bipolar cell. Such placement should minimise the incidence of unwanted neural activation and allow for more precise phosphene generation. In the case of an epiretinal prosthesis, electrical stimulation would likely activate not only the targeted neuron population (i.e. retinal ganglion cells) but also their axons which lie in the nerve fibre layer in direct contact with the electrode array. This assertion

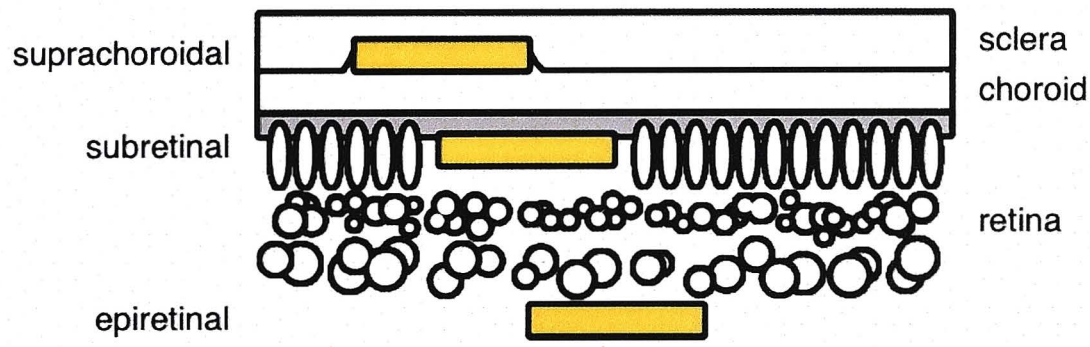

Figure 2.2. Schematic showing potential sites of stimulation for a retinal prosthesis, indicated by the yellow rectangles.

was made by Schiefer and Grill (2006) using computational models of the retinal ganglion cell and experimentally validated by Sekirnjak and colleagues with their finding that the lowest epiretinal stimulation thresholds were observed when the stimulating electrode was situated at the axon hillock (Sekirnjak et al., 2008). Activation of ganglion cell axons would then potentially result in multi-site or smeared visual percepts (Wilms and Eckhorn, 2005; Schiefer and Grill, 2006). The Zrenner device too comes with its own distinct drawbacks. In contrast to the Humayun prosthesis the device electronics are in direct contact with the retina, increasing the likelihood of thermal injury to retinal neurons and placing further constraints on the output power of the device. The limited space available for device electronics represents an additional challenge to be faced by hardware designers. It has also been demonstrated that the energy generated by a single photodiode is insufficient to elicit retinal activation from ambient light (Zrenner et al., 1999; Besch et al., 2008), undermining the feasibility of the passive 'photodiode prosthesis' concept (but see Yang et al., 2011). Subretinal prostheses of this type currently in development employ external power sources for this reason.

Research groups are also exploring the possibility of *suprachoroidal* retinal activation whereby an electrode array is placed between the choroid and sclera and driven by an external neurostimulator (e.g. Wong et al., 2009). As the electrodes are not in direct contact with the retina, the suprachoroidal approach mitigates the risks of incurring retinal damage by surgical implantation and device operation and as such represents an improvement over subretinal array placement. A study by Yamauchi and coworkers (2005) compared the two modes of implantation in the rabbit and observed histological evidence of ONL retinal damage following subretinal array placement. No such damage was found after suprachoroidal implantation. Being situated on the choroidal surface may also prove to be beneficial. A reflexive mechanism that increases choroidal blood flow in response to light or light-generated heat has been

demonstrated in monkeys and humans and helps to maintain a stable temperature for the outer retinal layers (Parver et al., 1983). With respect to a prosthesis situated in the suprachoroidal space this choroidal blood flow should act to dissipate heat and minimise the incidence of thermal retinal trauma. Additional benefits include a relatively simple surgical procedure, reduced risk of choroidal haemorrhaging and good long-term implant stability (Zhou et al., 2008). The distance between the electrode array and the retina however, is of particular concern for this type of prosthesis as is the disadvantage of having to stimulate through the retinal pigment epithelium – a high-resistance layer of ocular tissue (e.g. Heynen and van Norren, 1985). On top of needing more current to activate retinal neurons, suprachoroidal electrical stimulation will likely activate a broader area of the retina compared with other modes of stimulation, limiting the maximum spatial resolution achievable by such a prosthesis.

2.2 Human trials

Human trials of retinal prostheses have been successful in eliciting visual percepts. Preliminary experimentation by Humayun et al. (1996) demonstrated the viability of generating visual input through electrical stimulation of the retina in five subjects with little or no light perception. Electrical stimulation was delivered through small, hand-held probes containing one or more electrodes which were inserted through the sclera and placed over the retinal surface. Subjects who previously had useful vision observed phosphenes varying in size (pea, match head, pin, 2.54 mm by 6 mm) and shape (round, ring, lines, rectangle) and were able to accurately localise the phosphenes according to the retinal area stimulated. In 2003 Humayun and co-workers went on to develop an epiretinal prosthesis and implant the device in a blind subject with retinitis pigmentosa. A small camera set within the frame of a pair of glasses and connected to a belt-worn visual processing unit comprised the external portion of the device. Electrical stimulation commands generated by the processing logic were transmitted wirelessly to a 4×4 array of platinum discs of 520 µm diameter arranged into a square layout and implanted onto the retinal surface. The subject observed phosphenes on all 16 electrodes of the array and could resolve visual percepts evoked by a pair of adjacent electrodes with 720 µm centre-to-centre separation during acute experimentation. Reported

phosphene sizes varied from a 'match head' to a 'quarter[1]' at arm's length and shapes were mostly described as round spots of light. More recent clinical trials of retinal prostheses have demonstrated that with sufficient training (and given enough time), blind subjects are able to read large, high-contrast letters, recognise everyday objects such as a plate, a square and a cup on a table, and perform basic mobility tasks (Rizzo III, 2011; Zrenner et al., 2011).

Although electrical stimulation of the human retina yields visual sensation, the underlying physiological response is neither consistent nor well-understood. In contrast with the encouraging results reported by Humayun's group in 2003, a different epiretinal implant study later that year reported difficulty in reliably evoking visual percepts (Rizzo III et al., 2003). Using square grids containing 100 μm to 400 μm diameter electrodes three blind volunteers with severe retinitis pigmentosa matched evoked percepts with their corresponding stimulating electrodes 48% of the time. Results of two-point discrimination trials between electrode pairs were at best inconclusive. At present, blind patients generally do not consider the benefits imparted by modern retinal prostheses useful enough to justify the risks associated with surgical implantation, or the monetary cost (Rizzo III et al., 2003).

In addition to perceptual efficacy the amount of current needed to elicit a visual percept, or the *perceptual threshold* represents another factor that varies widely across not only clinical trials but trial subjects. While stimulation thresholds in Humayun et al.'s subject varied between 50–500 μA, two other trials reported average stimulation threshold ranges of 24–702 μA (Mahadevappa et al., 2005) and 27–239 μA (de Balthasar et al., 2008) across their subjects with considerable inter-subject variation. Each of these studies involved chronic epiretinal implants and used similar electrode diameters (500 μm or 520 μm), centre-to-centre separation (720 μm or 800 μm), phase durations (1 ms) and stimulation paradigms.

2.3 Stimulating the healthy retina

A successful retinal prosthesis will use electrical stimulation to replicate light-evoked cellular activity. Given that there are multiple types of both bipolar and retinal ganglion cells (Dacey has identified 17 different types of retinal ganglion cell (RGC) in the macaque retina (2004) and Chan et al. (2001) have

[1] A US quarter has a diameter of around 24 mm.

found 10 types of bipolar cell in the marmoset) with each class exhibiting its own characteristic spatiotemporal pattern of activity (Roska and Werblin, 2001), this is an enormously complex task. Light-evoked retinal activity is characterised by fast spiking frequencies – certain classes of RGC can reach spiking rates of more than 260 Hz (O'Brien et al., 2002). High-resolution vision further requires a high degree of spatial specificity which is complicated by the substantial overlap of ganglion cell dendritic fields in the retina (Wässle, 2004) as well as the extremely large number of retinal cells excited by electrode stimulation – ganglion cell densities can reach 32,000–38,000 cells/mm^2 in the human retina (Curcio and Allen, 1990). It follows that indiscriminate electrical stimulation would recruit multiple neuron populations and result in a physiological response bearing little resemblance to that of natural vision.

The physiological response of the retinal network to electrical stimulation has been investigated in a number of studies. Jensen et al. (2005a) established that the response of rabbit RGCs to epiretinal electrical stimulation consists of short- and long-latency components. Short-latency activity recorded from RGC axons was characterised by a single, time-locked action potential recorded less than 5 ms after stimulation onset and was attributed to *direct* RGC activation. In contrast, long-latency responses appeared between 8 and 60 ms after the stimulating pulse and were abolished by chemically blocking ganglion cell input, suggesting that retinal interneurons presynaptic to the RGCs were responsible for this *indirect* activation. Other groups (e.g. Sekirnjak et al., 2006) have observed this type of response but differ in how they classify the two components, with short spike latency classified as less than 2 ms and later responses labelled as long-latency in this study. These temporally distinct responses to retinal stimulation have likewise appeared in evoked potential recordings from the visual cortex (Chen et al., 2006).

It has been demonstrated that direct retinal ganglion cell activation can replicate the temporal properties of light-evoked responses. Fried et al. (2006) established that direct RGC activation typically resulted in a single action potential and could reliably be used to generate spiking rates of up to 250 Hz. Direct activation of RGCs has been found to support high-frequency electrical stimulation in both epiretinal (Sekirnjak et al., 2006) and subretinal (Tsai et al., 2009) studies. In contrast with these studies is that of Jensen and Rizzo III (2007) which investigates the effect of repetitive electrical stimulation of the retinal neural network. The strength of the response to indirect RGC stimulation was found to be highly dependent on the pulse interval.

As well as observing lower response strength for shorter pulse intervals, response amplitudes became progressively lower with each consecutive pulse of the stimulating pulse train. Even for a relatively low stimulation frequency of 15 Hz, the response strength for the second pulse was reduced by 42% in comparison to the first pulse, with this reduction increasing to 59% by the tenth pulse. This desensitization has been observed in other animal studies featuring electrical stimulation of the retinal network (Ahuja et al., 2008; Tsai et al., 2009) and is likely related to the rapid fading of phosphenes evoked by periodic stimulation during clinical trials (Zrenner et al., 2011; Wilke et al., 2011).

There is, however, some evidence to suggest that while direct activation facilitates temporal control of retinal spiking, indirect activation is more spatially localized. Elfar et al. (2009) found that the centre of gravity for retinal activity induced by indirect activation followed the location of the electrical stimulus, while centres of direct retinal activation were shifted towards the area centralis. It is thought that the short latency retinal response to electrical stimulation originates from the incidental activation of ganglion cell axons underneath the stimulating electrode (Jensen et al., 2005b; Elfar et al., 2009). Accordingly, cortical activity arising from indirect RGC stimulation may offer better spatial resolution largely because the targeted bipolar cells do not have lateral axons. It may be possible, however, to avoid axonal activation by using a particular electrical waveform, as suggested by Freeman et al. (2010). The authors found that while sinusoidal stimulation using frequencies of 10 Hz and 25 Hz could be used to evoke a robust RGC response when stimuli were delivered near the soma, spiking could not be elicited with even the strongest stimuli when the stimulating electrode was positioned over the distal axon, roughly 1 mm from the soma.

Improvements to spatial selectivity have been afforded by the development of electrodes with increasingly small diameters (but see Behrend et al. 2012). Stett et al. (2000) used 10 µm diameter electrodes in their study of the isolated chicken retina and found that evoked activity resulting from subretinal charge injection was localised to an area within 100–200 µm of the electrode. Jensen et al. (2003) put 2 µm diameter electrodes to use in an *in vitro* study of the rabbit retina aimed at determining extracellular RGC stimulus thresholds, concluding that in addition to lower thresholds and more localised activation, cathodic stimulation allowed for better cell body selectivity over axons in comparison with anodic stimulation. A later study of the macaque retina

showed that parasol ganglion cells could be stimulated with enough spatial specificity such that single cell stimulation produced negligible activation of neighbouring cells (Sekirnjak et al., 2008). Parasol ganglion cells are thought to be responsible for conveying achromatic spatial vision (e.g. Dacey, 2004) and have dendritic trees that cover areas roughly 100 µm wide on the retina (Dacey, 1993). The electrode arrays used in these *in vitro* studies are remarkable in that such electrode diameters (5–15 µm) and spacings (25–100 µm) are an order of magnitude smaller than those encountered in the majority of *in vivo* studies.

At this stage it is unclear whether electrical stimulation can be made to selectively activate particular cell types of a broader class. As mentioned previously, ganglion cells favour brief pulse durations while inner retinal neurons are targeted by longer pulse durations (Margalit and Thoreson, 2006). Freeman et al. (2010) have shown that certain retinal types respond preferentially to specific frequencies of sinusoidal stimulation. RGCs were best activated by high frequency (100 Hz) stimulation, with lower frequencies (25 Hz) targeting bipolar cells and photoreceptors preferentially stimulated at 5 Hz. This seems to agree conceptually with the result of Margalit's group, as a given cycle of a sinusoid resembles a biphasic pulse. One finding from the study of Jensen and Rizzo III (2006) suggests that ON RGCs (those which are stimulated by light, as distinct from those stimulated by an absence of light) favour cathodic current pulses.

The indiscriminate activation of multiple retinal pathways by means of electrical stimuli represents a profound issue that will hinder the generation of meaningful prosthetic vision. A stimulation strategy that is able to selectively activate ON and OFF pathways, for example, may well allow for the smooth perception of fundamental spatial patterns – a great boon to any unsighted patient. Selective activation of neural populations remains a key challenge to be addressed by any vision prosthesis that endeavors to restore normal vision to the blind.

2.4 Stimulating the degenerate retina

There are concerns about the viability of evoking visual perception from electrical stimulation of the degenerate retina. The brain exhibits *neuroplasticity* – the ability to reorganise and adapt neural circuitry to compensate for injury

or disease. In the case of blind individuals, parts of the visual cortex activate in response to auditory and tactile stimulation so as to enhance the processing of associated sensory information (Theorét et al., 2004). Such abnormal operation of the visual cortex may have a detrimental effect on the ability to perecive phosphenes. Gothe and colleagues (2002) demonstrated this possibility in their use of transcranial magnetic stimulation to evoke phosphenes in blind subjects through stimulation of the occipital lobe. Results of their study found that only two of the ten subjects with no residual vision (both with previous visual experience) reported phosphenes. The retina itself also undergoes extensive neural reorganisation during the progression of a degenerative disorder such as retinitis pigmentosa (RP) (see Marc et al., 2003). The structure and function of the RP-afflicted retina may therefore be substantially different compared with that of the healthy retina, as may be the effect of electrical stimulation.

Retinal degeneration commonly begins when rods lose the ability to regenerate their outer segments. As the rods deteriorate, their neurites sprout and enter the inner layer. The loss of rod outer segments collapses the subretinal space as cones begin to follow the path taken by the rods through the deterioration of cone outer segments. A dense layer of Müller cell processes (the beginnings of what is termed the 'glial seal') has formed over a substantial area of the retina by this stage, separating the RPE from the distal margin of the neural retina. At this point, the rate of rod death has significantly increased, a certain proportion of bipolar cells has died and the reorganisation of neural circuitry has begun. Rod and cone bipolar cells retract their dendrites while cone-synapsing horizontal cell bodies expand and extend neurites into the inner plexiform layer. After the complete loss of photoreceptors, the glial seal becomes compacted and Müller cell hypertrophy results in the formation of columnar structures which segment the retina. Neurons of the inner plexiform layer produce dendrites whose foci form in the residual outer plexiform layer. Neuronal cell death is now indiscriminate. A number of physiological processes take place alongside neuronal death during the advanced stages of neural remodelling including cell migration, microneuroma (complex tangles of processes from multiple cell types) formation and excessive neurite growth, with horizontal and amacrine neurites forming abnormal connections within the neural network (Fariss et al., 2000). These physiological events may have different timings depending on the type of disease.

How do the rewired visual pathways function in the degenerate retina? Since

they are no longer driven by the sensory retina, it has been suggested that surviving cells extend their neurites to derive input from residual visual pathways (Marc et al., 2003). The formation of microneuromas demonstrates that retinal neurons are not programmed to restore their original circuitry – the degenerate retina hosts many different abnormal synaptic structures which disrupt visual processing and introduce sporadic oscillatory circuit behaviour. Some evidence for this stems from the intermittent perception of flashes of light known as *photopsias* commonly observed by RP patients. Photopsias are thought to originate in the retina because not only do they eventually disappear (suggestive of ganglion cell death), they have also been temporarily induced through electrical stimulation of the retina in an RP patient who reported last experiencing the percepts around 40 years earlier when her vision was beginning to deteriorate (Marc et al., 2003; Delbeke et al., 2001). The significant difference in retinal structure and function suggests that the evocation of meaningful visual perception from electrical stimulation will be more difficult in the degenerate retina than in the healthy retina and will surely pose further hindrance to vision restoration strategies.

2.4.1 Degenerate models

Animals with degenerative retinal diseases pathologically equivalent to those found in humans provide an alternative means of investigating human retinopathy and potential treatment. The inception of successful retinal prosthetic stimulation strategies to restore high resolution vision to RP patients will likely follow a much improved understanding of a) the residual functional capacity of the RP-afflicted retina and importantly, b) how electrical stimulation modulates the output of this retina. Degenerate animal models allow researchers to make informed assumptions about implant efficacy in the human and so are valuable subjects in retinal prosthesis studies (Suzuki et al., 2004; O'Hearn et al., 2006; Weitz et al., 2011; Cho et al., 2011, 2012).

One of the earliest animal models studied is the *rd mouse*. Originally discovered in 1923 by Keeler and soon after forgotten until its rediscovery some thirty years later by Brückner and coworkers (Hafezi et al., 2000), the rd mouse suffers from a genetic mutation resulting in the rapid degeneration of the outer retina after the first postnatal week of life. Most of the photoreceptor population is eliminated by the first month. This mutation has been observed in human sufferers of the autosomal recessive form of RP (Takahashi et al., 1999)

which accounts for around 20% of RP patients (Daiger et al., 2007). Autosomal dominant RP is another major RP type with 30% prevalence among sufferers and it too has an associated degenerate model: the *Abyssinian cat*. These and other *hereditary* models vary in animal, genetic mutation and time course of degeneration – while photoreceptor loss can be observed within days in the rd mouse, similar observations in the Abyssinian cat will not be made for months (Hafezi et al., 2000).

The identification of genetic sequences or 'genotypes' which give rise to retinitis pigmentosa has clearly demonstrated that it is not a single disease but a group of diseases characterised by varying point mutations within the human genome. Not long after Dryja and colleagues (1990) discovered the most prevalent genotype for autosomal dominant RP, efforts aimed at transgenically engineering an animal model of the disease led to the creation of the *P23H* rat (Olsson et al., 1992). A *transgenic* model can be made to express any genotype of retinitis pigmentosa through insertion of the corresponding mutant gene into the animal's genome.

Retinal degeneration generally follows a pathological sequence consisting of photoreceptor loss followed by various remodelling events, as has been discussed. Are these secondary events caused solely by photoreceptor degeneration or are they influenced by developmental defects? Nagar et al. (2009) have addressed this question through the use of a *nongenetic* animal model of degeneration in which selective photoreceptor loss was induced in an adult mouse with an injection of N-methyl-N-nitro-sourea (MNU). The study found that retinal remodelling took place in much the same way as in genetic animal models, suggesting that the remodelling is independent of the cause of photoreceptor degeneration. This finding is particularly encouraging for retinal prosthesis research, as nongenetic models are generally cost-effective and allow for control over the onset and severity of degeneration. Other methods of inducing retinal degeneration involve exposure to bright light, a taurine-deficient diet and retinal hypoxia (e.g. Krebs et al., 2009; Hayes et al., 1975; Maslim et al., 1997).

As a result of its profound anatomical transformation, the late-stage degenerate retina exhibits markedly different functional properties to its healthy counterpart. Pu et al. (2006) investigated single-unit RGC responses in the RCS rat and found significant decreases in receptive field size, and reductions in sensitivity to luminance and contrast. The study also suggested that the

degenerative process has a differential effect on the ON and OFF pathways, with the likelihood of recording from an ON cell drastically falling after P36-37. While the dendritic morphology and structure of the RGC population appear to be substantially preserved (Mazzoni et al., 2008), the degenerate RGC is known to possess greater spontaneous activity (Pu et al. 2006; Stasheff 2008; Margolis et al. 2008; Margolis and Detwiler 2011; but also see Sekirnjak et al. 2008), as well as characteristic 'waves' of spiking (Margolis et al., 2008; Stasheff, 2008). These aberrant behaviours arise not only from pathological circuitry that forms during the remodelling phase of degeneration (Margolis and Detwiler, 2011; Jones et al., 2012), but also through changes in intrinsic cellular properties (Sekirnjak et al., 2011). It is plausible then, that the ability of a retinal prosthesis to electrically induce neuronal inhibition may be just as important as the ability to induce excitation, particularly when considering the elevated spontaneous activity present in the degenerate retina.

It has been established that cortical activation in response to electrical stimulation of the diseased retina is indeed possible. Kanda and coworkers (2004) managed to elicit evoked potentials in the visually deprived RCS rat model through suprachoroidal retinal stimulation. The stimulation thresholds in the degenerate retina were found to be higher (μ: 12.9 nC versus 7.2 nC) and more variable (σ: 7.7 nC c.f. 2.8 nC) than those of the healthy retina. Visual stimuli failed to elicit any response in the RCS retina. Another study found that cortical responses could be evoked from epiretinal stimulation of the degenerate retina in three different biological models: the mouse, canine and human, with the canine response exhibiting similar latency to that of the human (Chen et al., 2006). Further work by Sekirnjak et al. (2009) investigated the response of individual ganglion cells to electrical stimulation in the P23H retina *in vitro*. The study found that despite severe photoreceptor degeneration and a complete absence of any light response, the responses of ganglion cells to electrical stimulation in the degenerate retina were similar to those of the normal rat retina.

The overwhelming (yet unsurprising) finding among research groups is that the degenerate retina is more difficult to electrically activate than the healthy retina *in vivo*. Not only does the diseased retina require more charge to activate (Kanda et al., 2004; Siu and Morley, 2008), functional thresholds appear to increase as the degeneration progresses (Suzuki et al., 2004; Chan et al., 2008; Siu and Morley, 2008). As Fried et al. (2006) suggest, the precise spatiotemporal patterns of ganglion cell activity resulting from visual stimuli are

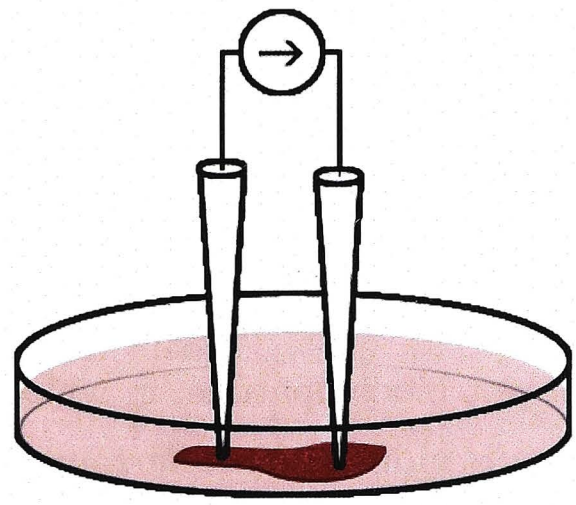

Figure 2.3. Basic electrochemical system using a current source to pass current between two electrodes to stimulate excitable tissue.

likely not being replicated by the electrical stimulation in animal studies to date.

2.5 Underlying principles

Each type of microelectronic retinal prosthesis operates by injecting charge into excitable tissue to elicit cellular activation. An electrode array placed on the retinal surface forms an electrochemical system in which the physiological medium serves as an electrolyte. At least two electrodes are needed to complete the circuit and permit stimulation: one to allow current to flow into the electrolyte and another to provide the current's return path. One method for controlling charge injection at the electrode-electrolyte interface is to use a current source to pass a user-specified current through the electrolyte as shown in figure 2.3. Since ions are responsible for carrying charge within the electrolyte and neuron activation is regulated by extracellular ion movement, the modulation of electrical stimulation by current flow adjustment is particularly effective. This method affords direct control over the net charge delivered to the tissue which proves to be useful in ensuring a safe stimulation paradigm, as will be discussed.

Safety is an essential aspect of any medical system. Retinal prosthesis usage can potentially give rise to damage which may be electrical, chemical, or mechanical in nature. An ever-present source of chemical damage is the stimulation mechanism itself. A current waveform with non-zero DC component leads to a net charge transfer into the electrolyte and results in the increased production of chemical species that may be harmful to the retina or electrode (Roach, 2003; Merrill et al., 2005). The common use of a biphasic waveform

seeks to mitigate the production of such species with the second phase acting to reverse the offending electrochemical reactions that take place during the stimulating phase. The use of short phase periods on the order of microseconds is also common as longer current pulses tend to result in electrode degradation (Rose and Robblee, 1990). Chemical and physiological damage can result if the electrode material is not biocompatible, in which case a toxic, necrotic or otherwise averse response is induced from surrounding tissue. Other sources of tissue damage may include the intrinsic biological processes that arise from overstimulation. Oxygen and glucose depletion, changes in ionic concentrations of extracellular potassium, and excessive release of neurotransmitters in the central nervous system have all been proposed as mechanisms for excitotoxicity (Merrill et al., 2005).

A fundamental consideration for a retinal prosthesis is the selection of fabrication materials, particularly for the stimulating electrodes that come into contact with excitable tissue. In addition to exhibiting biocompatibility, they must be capable of delivering enough charge to evoke a suitable biological response, while operating within safe stimulation limits. The electrodes must also retain electrochemical stability for the specified lifetime of the implant, which can potentially span for decades. Cogan (2008) review several different materials encountered in previous electrophysiological studies, together with their relative advantages and disadvantages.

Electrical stimulation has been associated with retinal damage in a number of *in vivo* animal studies. Butterwick et al. (2007) have investigated the dependence of damage thresholds on electrode size, pulse duration and number of pulses for a charge-balanced biphasic waveform in the chicken retina. They found damage thresholds decreased with the number of pulses and observed the threshold current density to be independent of electrode surface area for diameters greater than 300 µm, scaling by $1/d^2$ for diameters smaller than 200µm (figure 2.4). The relationship between threshold current density J and pulse width t was deduced roughly as $J \propto t^{-0.5}$. This scaling suggests that charge per phase and charge density are not the only factors that determine the tissue damage threshold. Another study investigated the pathology of electrically induced retinal damage in the rat (Colodetti et al., 2007). In one group of animals, a single electrode was inserted into the vitreous cavity of the eye and made to contact the retinal surface. A second group also had the electrode implant but no contact was made with the retina. It was found that, although the mechanical pressure exerted by the electrode was damaging to the retina

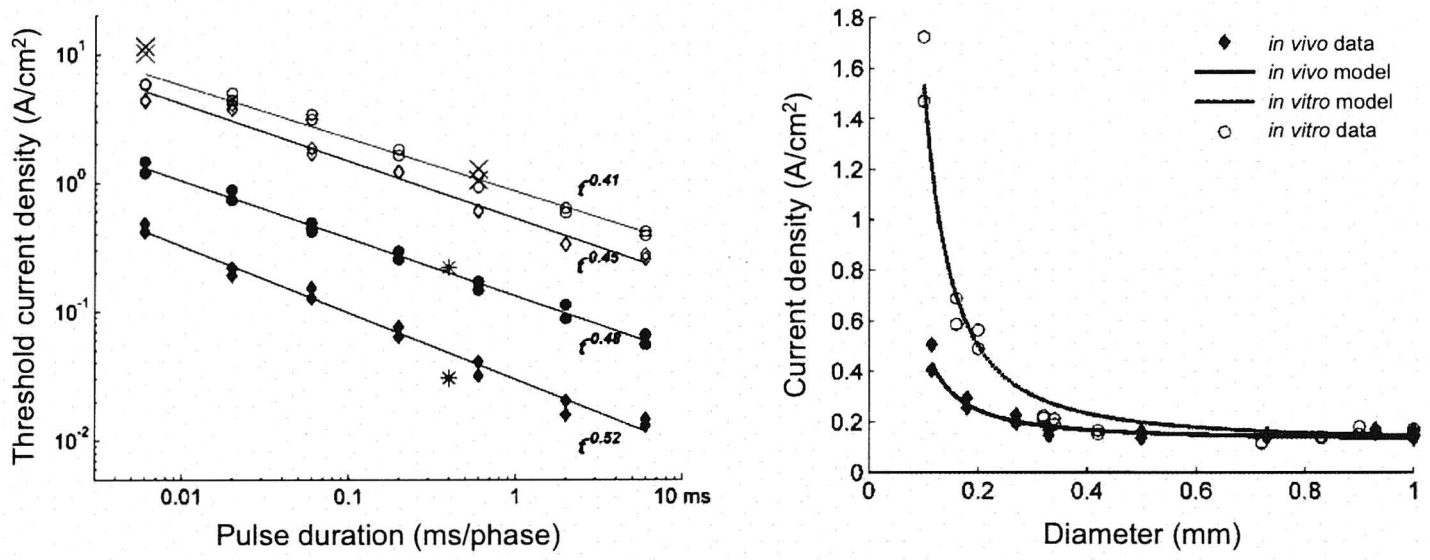

Figure 2.4. Modulation of retinal damage thresholds with pulse duration (left) and electrode diameter (right). Modified from Butterwick et al. (2007).

regardless of whether electrical stimulation was being delivered, the damage was greatest when retinal contact and electrical stimulation were coupled. The induction of tissue damage through excessive electrical stimulation is a possibility deserving of consideration in any vision prosthesis study, particularly in the case of retinal prostheses that intervene at the retinal surface.

2.6 Summary

While significant advances in the scientific body of knowledge have progressed the field of prosthetic vision well beyond the rudimentary stages fathered by Brindley and Lewin in the late 1960s, the electrophysiological mechanisms governing the operation of retinal prostheses remain poorly understood. There are many technical challenges facing the development of high quality prosthetic vision, but the issue of selective neural activation by means of electrical stimulation is perhaps the most salient. I seek to address this issue in later chapters.

Chapter 3

Thesis Overview

Broadly, this thesis is concerned with the electrical activation of retinal ganglion cells with a view towards prosthetic vision. In the first chapter, the merits of studying rat A2 ganglion cell electrophysiology were established. Chapter 2 introduced the concept of prosthetic vision and examined some key issues associated with the idea of electrically stimulating the degenerate retina to elicit vision, including the requirement to elicit excitation in select cell populations. In the next chapter, I demonstrate the viability of using a stimulating electrode fabricated with nitrogen-doped ultra-nanocrystalline diamond (N-UNCD) to elicit neural activity in RGCs. This stimulating electrode is then recruited in Chapter 5 to determine the biphasic, rectangular electrical waveform parameters most effective in activating RGCs. Chapter 6 investigates the extent to which intracellular sinusoidal electrical stimulation can selectively stimulate ON and OFF RGC populations. The final chapter summarises the results of this thesis and suggests potential future directions.

My research sought to address the following questions:

1. For a rectangular, biphasic waveform, what are the most effective waveform parameters for electrical activation of retinal ganglion cells?

2. Can high frequency electrical stimulation selectively stimulate certain cell populations over others?

3. Is N-UNCD an electrochemically viable material for use in an electrode array for a retinal prosthesis?

Chapter 4

Stimulating with N-UNCD

This work has been published previously: Hadjinicolaou, A. E., Leung, R. T., Garrett, D. J., Ganesan, K., Fox, K., Nayagam, D. A. X., Shivdasani, M. N., Meffin, H., Ibbotson, M. R., Prawer, S. and O'Brien, B. J. (2012). Electrical stimulation of retinal ganglion cells with diamond and the development of an all diamond retinal prosthesis. *Biomaterials* 33(24): 5812–5820.

Electronic retinal implants for the blind are already a market reality. A worldwide effort is underway to find the technology that offers the best combination of performance and safety for potential patients. Our approach is to construct an epiretinally targeted device entirely encapsulated in diamond to maximize longevity and biocompatibility. The stimulating array of our device comprises a monolith of electrically insulating diamond with thousands of hermetic, microscale nitrogen-doped ultra-nanocrystalline diamond (N-UNCD) feedthroughs. Here we seek to establish whether the conducting diamond feedthroughs of the array can be used as stimulating electrodes without further modification with a more traditional neural stimulation material. Efficacious stimulation of retinal ganglion cells was established using single N-UNCD microelectrodes in contact with perfused, explanted, rat retina. Evoked rat retinal ganglion cell action potentials were recorded by patch clamp recording from single ganglion cells, adjacent to the N-UNCD stimulating electrode. Separately, excellent electrochemical stability of N-UNCD was established by prolonged pulsing in phosphate buffered saline at increasing charge density up to the measured charge injection limit for the material.

4.1 Introduction

The emergence of electronic retinal implants has the potential to significantly improve the lives of people suffering from several diseases that cause blindness (Dowling, 2005; Weiland et al., 2011; Klauke et al., 2011). The majority of existing implants consist of an array of electrodes that are surgically implanted into a position on or near the damaged retina. Data from the visual field is mapped onto the electrode array and the retina is electrically stimulated accordingly. Currently, three implantation locations for the electrode array dominate, namely; epiretinal (on the inner retina) (Klauke et al., 2011; Yanai et al., 2007), subretinal (between the retina and the choroid) (Zrenner et al., 2011; Yang et al., 2011; Kelly et al., 2011) or suprachoroidal (between the choroid and the sclera) (Shivdasani et al., 2010). A representation of the visual field is typically captured either by a camera worn by the user or by a photodiode array on the retinal device itself. Visual data from a camera can be sent to the retinal implant via either a wired or wireless link (fig. 4.1). Photodiode arrays on a retinal implants have the advantage that the diodes can be directly mapped to stimulating electrodes such that the image transduction and stimulating array move with the eye. The disadvantage of photodiode arrays is that they are electronically relatively simple giving the user limited control of stimulation parameters or image manipulation (Zrenner et al., 2011). Alternatively, data fed from a camera source can be relayed to a stimulating array in many different ways potentially making the device useful under a wider variety of conditions and better able to adapt to varying user needs and developments in information technology. The current generation of implants have sufficient resolution to aid the user with basic navigation (Yanai et al., 2007) and in some instances reading of large high contrast print (Zrenner et al., 2011). An aim for future devices is to achieve higher resolution and consequently a more useful and naturalistic visual experience for patients.

Materials selection for fabrication of electronic implants is of critical importance, in particular for components exposed to the body. To protect the device's electronics from the body, the device must exhibit excellent hermeticity. To protect the user from the device, it must additionally exhibit biocompatibility and biochemical stability. All materials must be resistant to sterilization procedures, mechanically robust, and sufficiently biochemically inert to operate continuously, potentially for decades. Diamond is a material that possesses all of these properties.

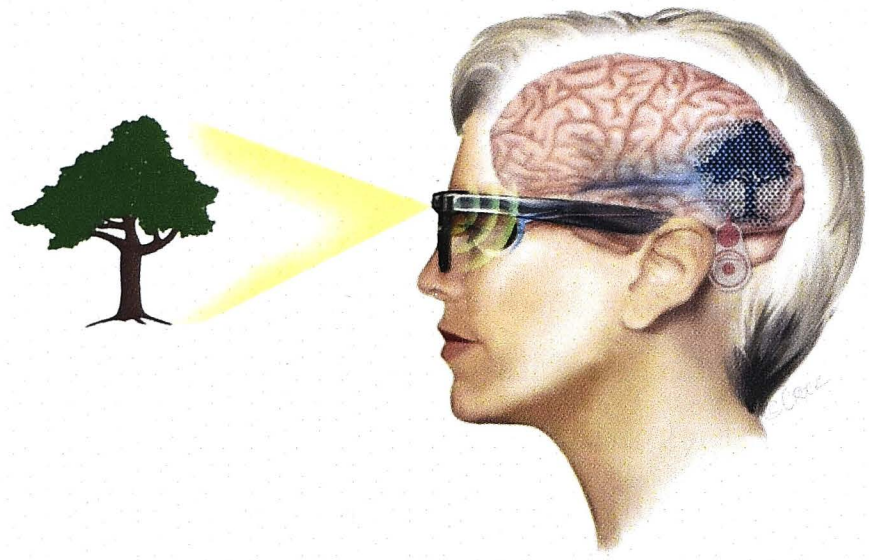

Figure 4.1. Illustration depicting image capture of a visual scene by a camera mounted on a pair of glasses. The visual data is relayed via a wireless link to an implanted retinal device that electronically stimulates the retina with a special pattern derived from the image. The stimulation pattern on the retina is relayed to the brain via the optic nerve providing the visual system with sufficient information to generate visual perception.

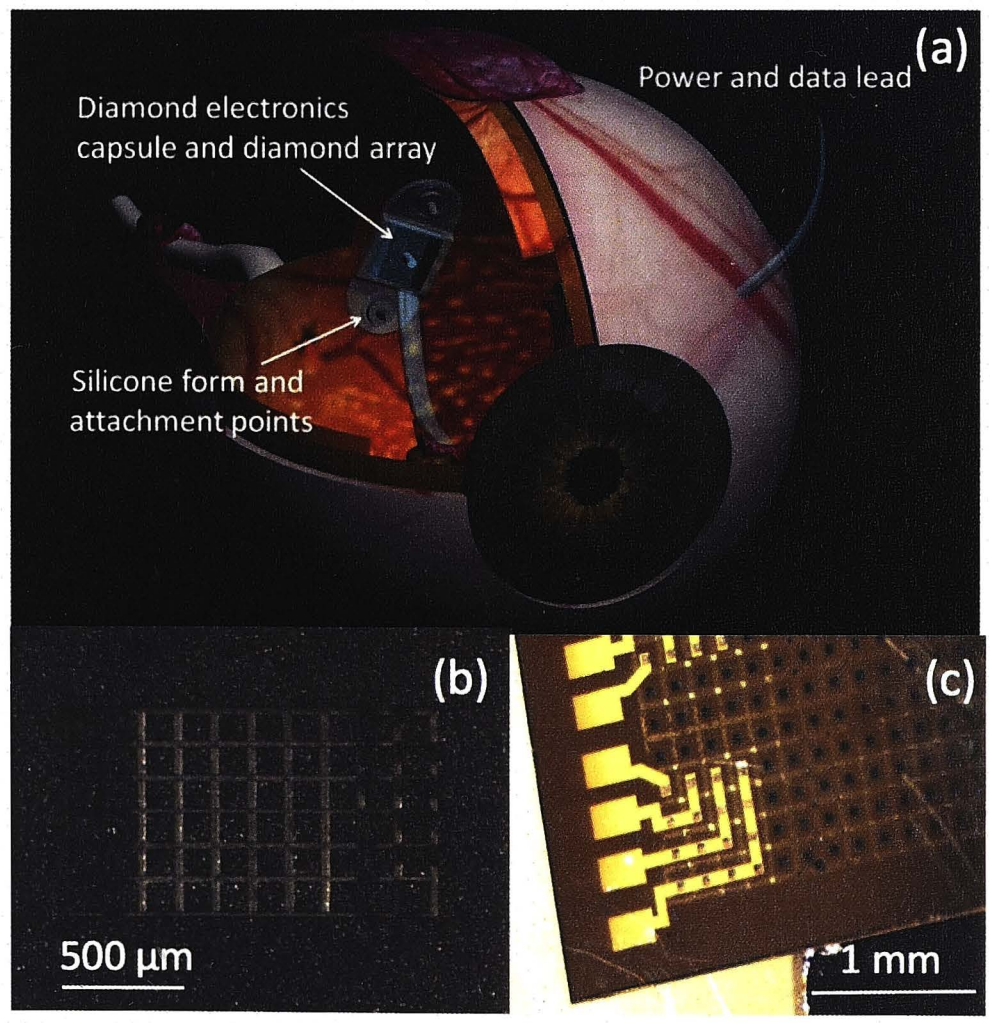

Figure 4.2. (a) Medical illustration of the form for the BVA epiretinal device, tacked in position over the macula. (b) Micrograph of the external face of a diamond feedthrough array. The black squares are conducting N-UNCD and the lighter lines are exposed PCD through which light is transmitted. Some ligt through the array is blocked by evaporated wires on the reverse side. (c) Interior face of the feedthrough array with evaporated metal wires contacting some feedthroughs.

The chemical and mechanical stability of diamond is well known. The device being developed as part of the Bionic Vision Australia (BVA) initiative is an epiretinal design that will interface with a head-mounted camera. The stimulating array and electronics capsule of this device will be fabricated entirely from diamond. The form of the current generation of the Bionic Vision Australia (BVA) epiretinal device, as shown in figure 4.2, incorporates a diamond capsule which houses the stimulator electronics and feedthrough array, soft silicone wings, retinal tack attachments as well as a data and power lead. The device will utilize electrically insulating polycrystalline diamond and electrically conducting N-UNCD, both of which have been shown to exhibit excellent biocompatibility (Tang et al., 1995; Aspenberg et al., 1996). The limited use of diamond in electronic devices can be attributed to the fact that diamond is difficult to shape and manipulate due to its extreme hardness and lack of ductility. We have developed a suite of techniques for manipulating diamond structures including fabrication of capsules, microneedles (Ganesan et al., 2010) and high numbers of conducting diamond feedthroughs in monolithic polycrystalline diamond films. A micrograph of our diamond electrode interface array is shown in fig. 4.2 (b) and (c). The array is constructed from a flat sheet of electrically insulating polycrystalline diamond through which feedthrough holes are cut. The feedthroughs are backfilled with conducting N-UNCD.

Of critical importance to the long term efficacy of an electronic retinal prosthesis is the electrochemical performance of the electrodes that are physically in contact with the retina. The electrodes must be able to deliver enough charge to evoke action potentials from ganglion cells while remaining within safe voltage limits (Cogan, 2008). In electrochemical terms this translates to a high electrode capacitance. We have previously shown that N-UNCD can be coated with platinum or electrochemically formed iridium oxide to increase charge injection (Garrett et al., 2011). Though coating of the N-UNCD feedthroughs with a high charge injection material is an option, it is one that comes with associated risks (e.g. delamination) (Cogan et al., 2004). It is advantageous both in terms of risk mitigation and fabrication simplicity if the N-UNCD feedthroughs can be used as the stimulating electrodes. We have previously established that by tailoring growth conditions and electrochemical activation the charge injection capacity (Q_c) of N-UNCD can be increased to values where neural stimulation becomes feasible (Garrett et al., 2011). Here we demonstrate that N-UNCD can effectively stimulate retinal ganglion cells (RGCs) while remaining within electrochemical limits. We also show

that N-UNCD exhibits very stable electrochemistry over extended use even when operating at the predefined electrochemical limits. Efficacious stimulation of RGCs is demonstrated by direct stimulation of RGCs in explanted rat retina. Responses from individual RGCs were recorded using the patch clamp recording technique. The collated threshold charge values required to affect a ganglion response are compared to the charge injection value established for the N-UNCD electrodes showing that efficacious stimulation was achieved well within the predefined electrochemical limits.

4.2 Materials and methods

4.2.1 N-UNCD electrode fabrication and characterisation

Fifty micrometre (μm) thick films of N-UNCD were grown in an Iplas microwave plasma assisted chemical vapour deposition (CVD) system. Samples were grown with a gas mixture of 20:79:1 N_2:Ar:CH_4 under conditions that have been described in detail elsewhere (Garrett et al., 2011). Single 200 × 200 μm square N-UNCD electrodes were prepared for retinal electrophysiology experiments (fig. 4.3 (a)). A 0.5 mm wide strip of N-UNCD was brazed to 100 μm thick tantalum foil in a high vacuum thermal annealer using a commercial diamond brazing alloy. Individual electrodes were cut from the brazed diamond/tantalum using a laser cutter (Oxford Lasers). The size of the electrode was reduced to 200 × 200 μm by laser milling of the excess diamond.

The metal shaft was insulated by placing a bead of silicone rubber on the electrode face under a microscope and then hand painting the tantalum shaft and electrode sides with epoxy resin. Finally the silicone rubber bead was removed to reveal only the face of the N-UNCD electrode and a final layer of silicone was applied to the shaft and the sides of the N-UNCD electrode. Electrical connection to the stimulator was made through the tantalum shaft.

Electrode arrays for electrochemical stability studies were four 600 μm diameter round discs of N-UNCD, synthesized under the same growth conditions (fig. 4.3b). The N-UNCD was cut by laser and glued to pads on a custom designed flexible printed circuit board (Flexible Circuits, USA) using conductive epoxy (Circuitworks, Chemtronics, USA). The electrodes were isolated by painting insulating epoxy resin around the electrodes and over the flex circuit under a microscope.

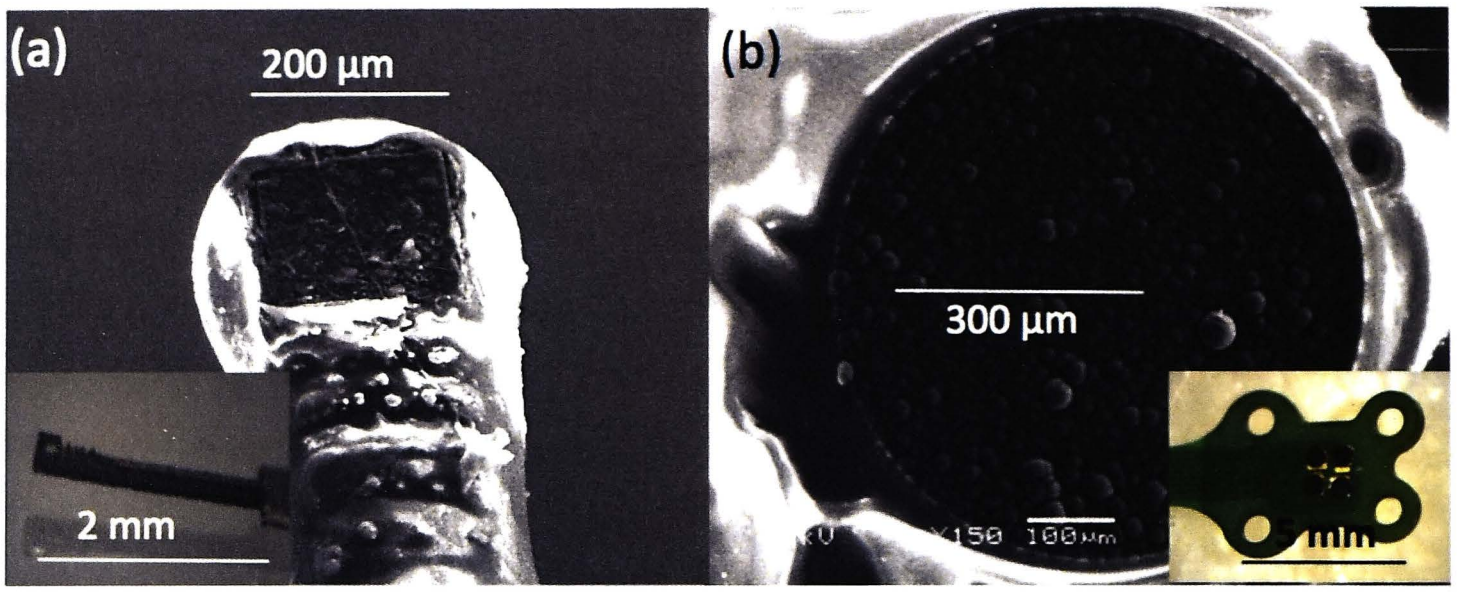

Figure 4.3. (a) SEM image of a 200×200 µm square N-UNCD electrode that has been used as a stimulating electrode on excised rat retina. Inset is a micrograph of the electrode before insulation with epoxy and silicone. (b) An SEM image of a 600 µm diameter N-UNCD disc electrode used to assess electrochemical stability. Inset is a micrograph of four such electrodes attached to a flexible circuit board and isolated with epoxy resin.

Both types of electrodes were electrochemically activated by three cyclic voltammograms (CVs) from 200 mV to 2.5 V versus Ag/AgCl at a scan rate of 100 mV s^{-1} in pH 7.4 50 mM phosphate buffer with 0.13 M NaCl (PBS), according to our previously established protocol (Garrett et al., 2011).

All cyclic voltammetry (CV) and some chronopotentiometry was conducted using an eDAQ EA163 potentiostat and a conventional three-electrode electrochemical cell arrangement with a 1 M Ag/AgCl reference electrode and a platinum wire counter electrode in PBS.

4.2.2 Electrochemical stability assessment

Interleaved stimulation of four 600 µm diameter N-UNCD disk electrodes was performed with a custom-built stimulator at current levels of 200 µA, 700 µA, 1200 µA and 1700 µA for 7 days such that all electrodes were subjected to a pulse frequency of 50 Hz. The range of current amplitudes was chosen to span the charge injection limit range for N-UNCD. Biphasic, cathodic first, charge balanced pulses of 500 µs/phase and 25 µs interphase duration were used. A platinum wire with capacitive coupling (10 µF) served as the counter electrode. All electrodes were short circuited together between pulses. Current and voltage waveforms (versus Ag/AgCl reference electrode) were recorded daily (PXI-4072, National Instruments, USA). Stimulation was performed in PBS, replenished daily, at room temperature, in a paraffin film (Parafilm M,

Pechiney, USA) sealed petri dish. Scanning electron microscopy (SEM) of all electrodes was performed before and after stimulation using a JEOL JSM-5910 microscope.

4.2.3 Explanted rat retina electrophysiology

Methods conformed to the policies of the National Health and Medical Research Council of Australia and were approved by the Animal Ethics Committee of the University of Melbourne.

Detailed procedures have been described previously (O'Brien et al., 2002). In brief, data came from 5 pigmented Long Evans rats ranging in age from 5 to 9 months. Animals were anaesthetized with a mixture of Ketamine (100 mg kg^{-1}) and Xylazine (10 mg kg^{-1}) and enucleated. After enucleation, rats were killed with an overdose of Sodium Pentabarbitone (350 mg, intracardiac). Retinal wholemounts were placed, ganglion cell layer up in the recording chamber (Warner Instruments, Hamden, CT USA, RC- 26GLP) and perfused (4–6 ml min^{-1}) with carbogenated Ames medium (Sigma-Aldrich, St. Louis, MO) heated to 34°C. The chamber was mounted on the stage of an upright microscope (Olympus, BX51WI) equipped with a 40× water immersion lens and visualized with infrared optics on a monitor with 4× additional magnification.

To obtain a whole cell recording, we first made a small hole in the inner limiting membrane and optic fibre layer overlying a ganglion cell (O'Brien et al., 2002; Taylor and Wässle, 1995; Robinson and Chalupa, 1997). Recordings were limited to RGCs exposed during this procedure that had smooth surfaces and agranular cytoplasm. The pipette internal solution contained (in mM): K-gluconate 110, NaCl 5, EGTA 5, HEPES 10, Mg-ATP 4; (mOsm = 282, pH adjusted to 7.3 with KOH) including Alexa Hydrazide 488 (250 μM) and biocytin (0.5%). Whole cell current clamp recordings from retinal ganglion cells were obtained with standard procedures (Hamill et al., 1981). Initial pipette resistance ranged between 3 and 7 MΩ. After obtaining a gigaohm seal and rupturing the cellular membrane, the pipette series resistance was measured and compensated with the bridge balance circuit of the amplifier. Resting potentials were corrected for the change in liquid junction potential that occurs upon break-in and cell dialysis. The liquid junction potential was measured directly as -11 mV (Neher, 1992). No capacitance compensation was employed.

Membrane potential was amplified (BA-1S, NPI), digitized with 16 bit precision at 20 kHz (USB-6221, National Instruments) and stored in digital form. The data collected were analyzed off-line with custom software developed in Labview (National Instruments). Cells were excluded from analysis if they exhibited marked instability of their resting potential or if their action potentials did not overshoot 0 mV. Once a quality recording was established, we measured each cell's response to biphasic (cathodic first) current stimuli of varying amplitude generated by the stimulator (Multi-Channel Systems, Germany) and delivered through a single diamond electrode (200×200 µm) placed upon the inner limiting membrane of the retina immediately adjacent to the recorded cell. Contact with the inner limiting membrane was evident when deformation of the surface of the retina could be seen under the microscope. In all cases, pulse duration of 500 µs per phase with an interphase gap of 25 µs was used. Each stimulus amplitude was repeated 10 times at a frequency of 1 Hz to generate an intensity response function where response was defined as the percentage of stimuli that evoked one or more action potentials. Individual action potential waveforms were extracted from the stimulus artefact by recording a subthreshold stimulus artefact, scaling it to the appropriate current amplitude, and subtracting it from the raw trace. This procedure is quite similar to that used to remove undesired leakage currents in voltage clamp experiments (p/n protocol, in our case p/3). Threshold was calculated as the current amplitude that evoked 50% efficacy using a two parameter logistic function to fit the data. Responses were recorded from a total of 12 RGCs using three identical electrodes such that each electrode was used to record responses from four RGCs.

Following recordings, the retinal tissue was removed from the chamber, mounted onto filter paper, fixed for 30–60 minutes in phosphate buffered 4% paraformaldehyde, and stored for up to 2 weeks in 0.1 M phosphate buffered saline (PBS; pH 7.4) at 4°C. The tissue was subsequently processed to reveal biocytin-filled cells by immersion in 0.5% Triton X-100, 20 mg mL^{-1} streptavidin conjugated to Alexa488 (Invitrogen) in PBS overnight. Tissue was washed thoroughly in PBS, mounted onto Superfrost plus slides and coverslipped in 60% glycerol. Cellular morphology was classified after 3D confocal reconstruction (Zeiss PASCAL).

4.3 Results

4.3.1 Electrode characterisation and electrochemical stability

Electrodes were characterised by cyclic voltammetry and chronopotentiometry before and after use. CVs were compared before and after activation and, in the case of the stability study, after use, to assess the degree to which the silicone insulation was leaking (i.e. thus exposing braze alloy) and to ascertain if electrochemical changes were occuring during use. Chronopotentiograms were recorded before and after activation using biphasic 100 µA amplitude constant current pulses of 1 ms per phase to assess the efficacy of the activation. A further set of chronopotentiograms were recorded to establish maximum charge injection values for the electrodes. These chronopotentiograms were recorded during 500 µs/phase constant current biphasic pulses of increasing current amplitude until the capacitive voltage excursion (the upward sloping section) during the pulse exceeded 1 V during the anodic phase. This was deemed to be a safe voltage as it lies well below the 1.5 V limit where oxidation of water begins to occur (see our previous work in Garrett et al. 2011). Representative CVs and 1 ms per phase chronopotentiograms recorded using both of the electrode types used in the work described here are shown in figure 4.4. Figure 4.4 (a) and (b) shows CVs and chronopotentiograms (respectively) for 600 µm disc electrodes used in electrochemical stability experiments. Figure 4.4 (c) and (d) show the corresponding plots for a 200 × 200 µm square N-UNCD electrode used for explanted rat retina experiments.

The CVs were recorded before (grey trace) and after (black trace) electrochemical activation and in the case of the 600 µm diameter electrode after one week of constant stimulation (dashed trace). Chronopotentiograms were recorded before (grey trace) and after (black trace) activation. The plots shown are typical of all the electrodes discussed in this paper with the exception of electrode 2 used for explanted rat retina. This electrode exhibited a small amount of silver contamination, which is highly likely to have occurred during brazing. CVs recorded over the voltage range -2–2.2 V exhibit significant oxidation of water above 1.5 V and reduction of water below 1.6 V, consistent with our previous findings (Garrett et al., 2011). After activation the charge injection capacity of the electrodes was calculated for biphasic constant current pulses, cathodic first and 500 µs/pulse. The charge injection capacity is derived from the current at which the capacitive charging voltage excursion reached 1 V.

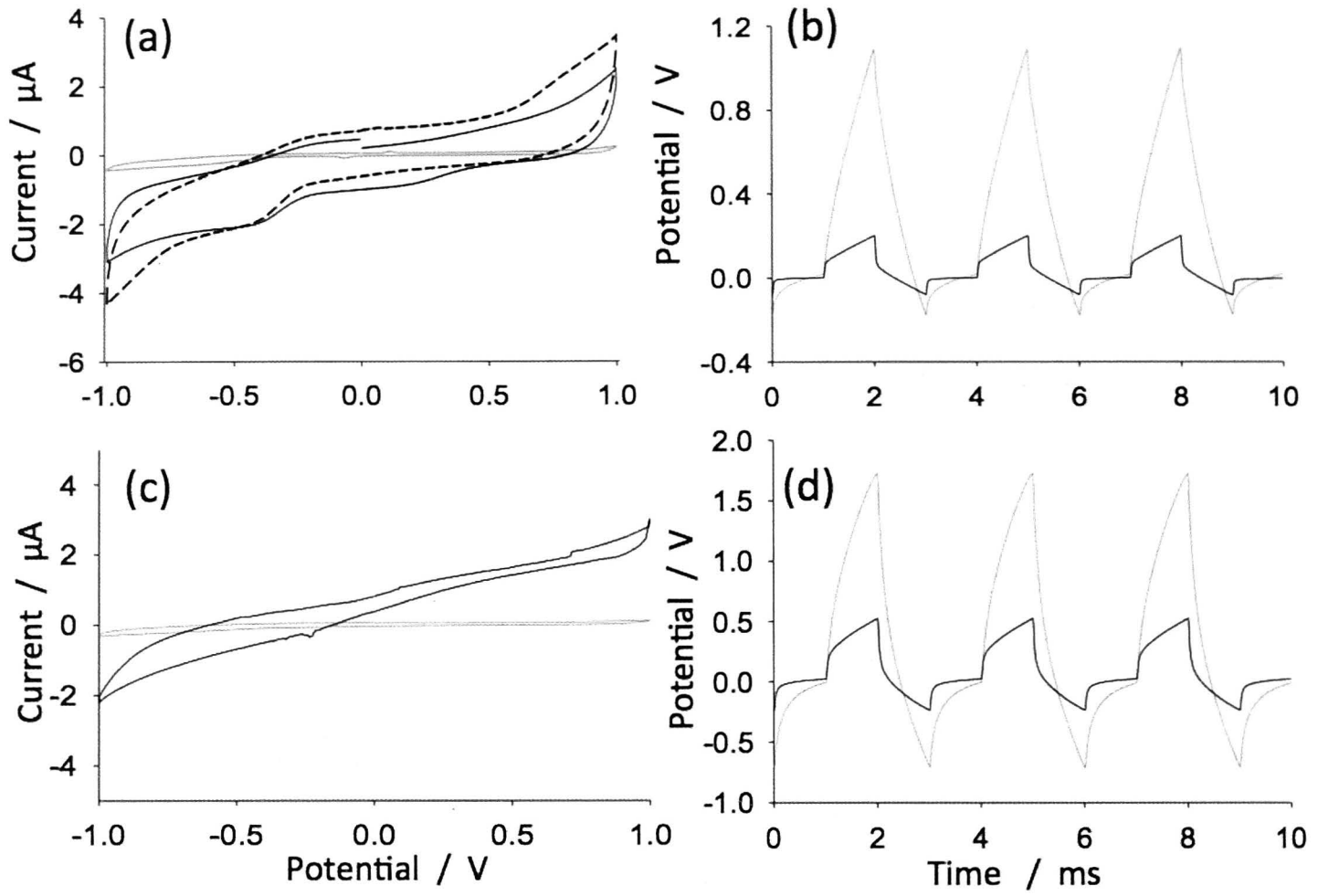

Figure 4.4. Representative CVs and voltage traces recorded using the electrode depicted in figure 4.3 (b) (plots (a) and (b)) and the electrode depicted in figure 4.3 (a) (plots (c) and (d)). CVs were recorded before activation (black trace) and after use (dashed trace). Voltage excursions were recorded during 1 ms, 100 µA per phase, biphasic constant current pulses before (dashed trace) and after (black trace) activation.

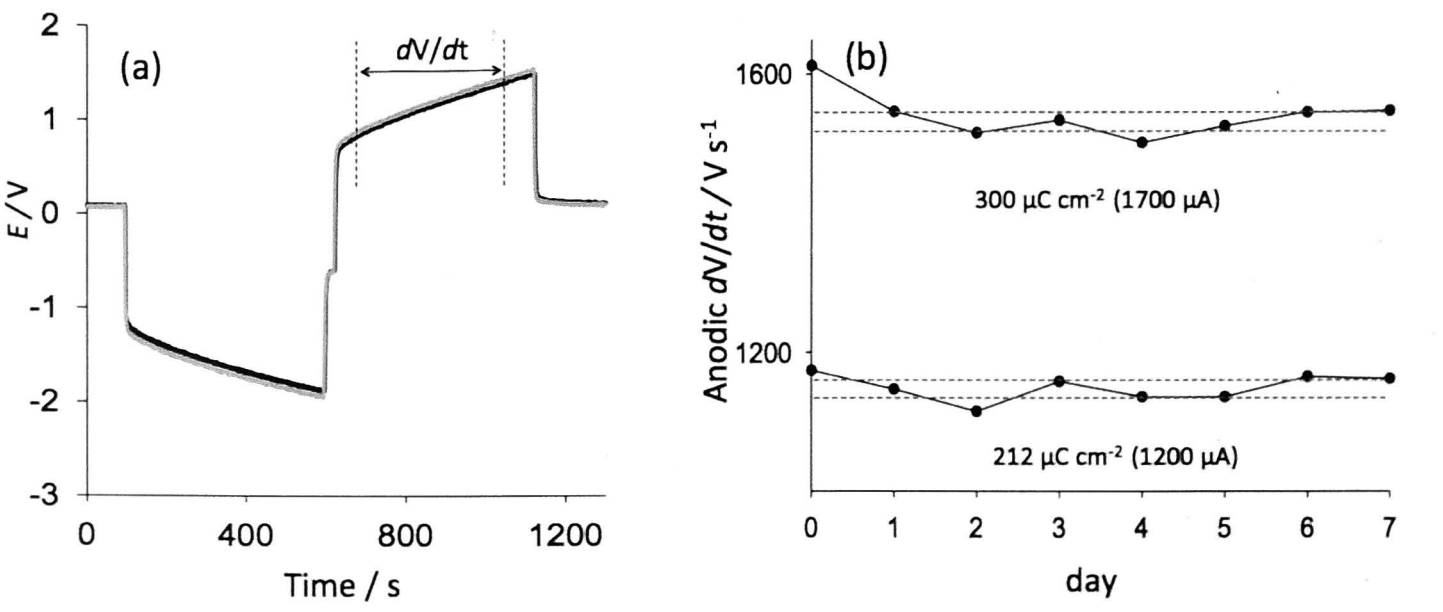

Figure 4.5. (a) Representative voltage excursions recorded using a 600 µm diameter N-UNCD electrode during 1700 µA, 500 µs per phase (300 µC cm^{-2}), biphasic, constant current pulses, before (grey) and after (black) one week of continuous pulsing at 50 Hz (3×10^7 pulses). Also shown is the region from which daily anodic charging voltage excursion slopes were calculated. (b) Shows day by day anodic excursion slopes recorded during pulsing at the current amplitudes and density indicated on the plots. The dotted lines represent $\pm$ one standard error of the mean or the 95% confidence interval of the mean (day 0 excluded).

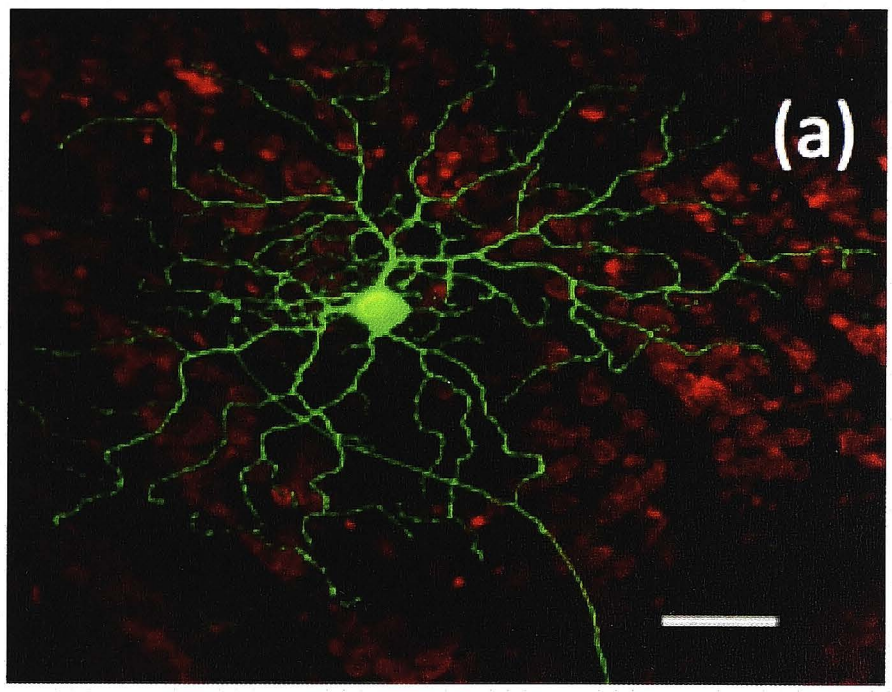

Figure 4.6. Rat retinal ganglion cell morphology and response to electrical stimuli. (a) En face view of a confocal reconstruction of the ganglion cell recorded and labelled with Alexa488 (green) along with the propidium iodide-labelled cells in the ganglion cell layer (red). Scale bar = 50 μm. (b) Raw responses of the ganglion cell in (a) above to a single subthreshold 20 μA pulse and several responses to 60 μA pulses. (c) Plots of action potentials elicited by the biphasic pulses extracted by scaling of the 20 μA trace and subtracting it from the 60 μA pulses.

For the 600 µm diameter electrodes this occurred at a current amplitude of 1700 µA/phase (shown in figure 4.5, grey trace), which equates to a charge injection capacity Q_c of 300 µC cm^{-2} according to the formula $Q_c = (I \times t)/A$ where I = the current amplitude at which the capacitive voltage excursion reached 1 V, t = the current pulse duration and A = the geometric surface area of the electrode in question. The capacitive charging voltage excursion for the three 200 × 200 µm square electrodes exceeded 1 V at a current of approximately 200 µA, which equates to Q_c = 250 µC cm^{-2}. For all subsequent experiments the charge injection limits for both electrode types was treated as an upper limit for testing. In some cases trace signals from residual braze could not be completely eliminated. Trace contamination was evident by the occurrence of a surface confined chemically reversible couple in the CV with a reduction peak at 0.2 V and an oxidation peak at 0.2 V, which we assume to be silver. Electrodes 1 and 3 described in this article exhibited clean CVs consistent with N-UNCD (e.g. fig. 4.4 (c)). Electrode 2 exhibited trace silver contamination but was used regardless, because the silver contamination was very low and did not adversely affect the electrochemical water window CV.

4.3.2 Electrochemical stability

Voltage waveforms were recorded daily for each of the four current amplitudes tested and the slope of the anodic voltage excursion calculated. Figure 4.5 (a) shows the voltage excursion occurring during a 1700 µA per phase pulse, before (grey) and after (black) one week of stimulation at 50 Hz. The slope of the voltage excursion during the pulse is related to the electrode capacitance by the relationship $dV/dt = i/C$ where dV/dt is the slope of the voltage excursion (V s^{-1}), i is the pulse current amplitude (A) and C is the electrode capacitance (F), therefore changes in the slope indicate changes in the charge injection capacity. A day-by-day plot of the slope of the voltage excursion during the anodic phase for the 1700 µA and 1200 µA are shown in figure 4.5 (b). Indicated on the plots (dotted lines) are the 95% confidence intervals of the means for the data recorded from days 1–7. In all cases the slope recorded on day 0 lay slightly above the 95% confidence interval and was therefore excluded from calculation of the mean.

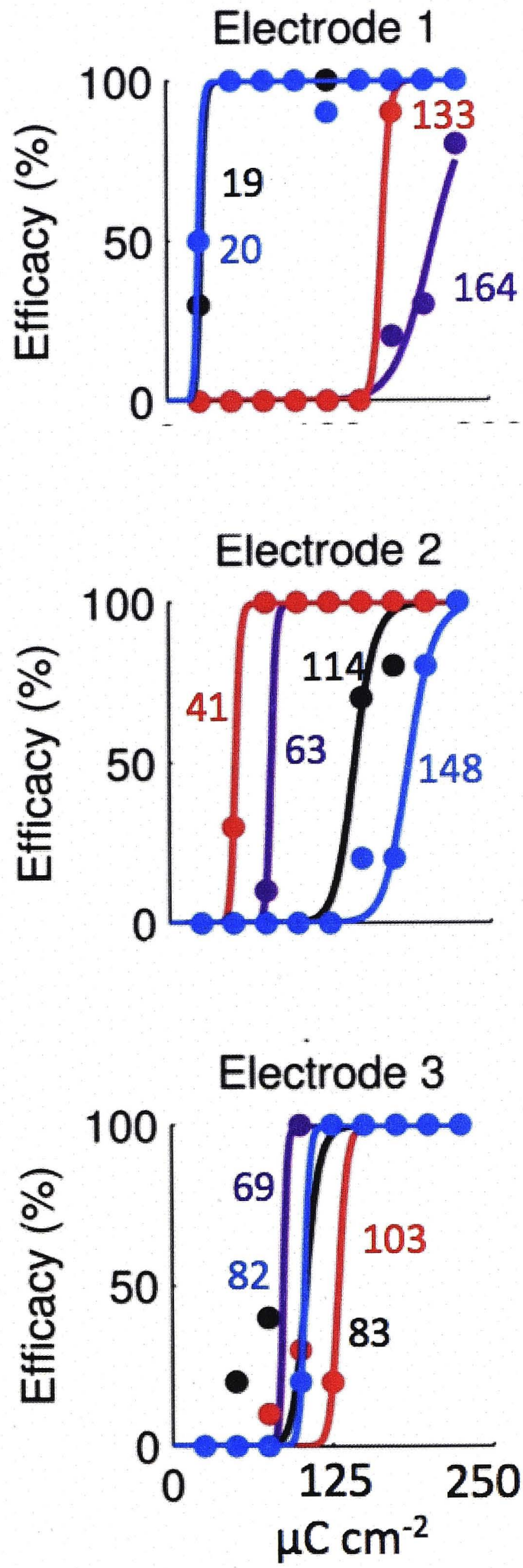

Figure 4.7. Intensity response functions of three N-UNCD electrodes. (a) Plots of raw data (coloured points) and their fitted curves (corresponding colours) for four different retinal gangilon cells activated by this electrode. The 50% efficacy threshold current amplitude for each RGC is indicated on each plot. Electrodes were placed in contact with the vitreal surface of the retina and biphasic stimuli of different amplitudes were applied at 1 Hz. Efficacy was defined as the number of stimuli out of 10 that evoked an action potential. Note that all cells reached threshold (50% efficacy) before the charge limitation was reached (250 µC cm^{-2}). (b), (c) Intensity response functions obtained using two additional N-UNCD electrodes ($n = 4$ for each). The intensity response function of the cell pictures in fig. 4.6 (a) was stimulated with electrode 2, and its response function is the red trace.

4.3.3 Explanted rat retina electrophysiology

We recorded the physiological responses of 12 rat RGCs to electrical stimulation through three different diamond electrodes. Figure 4.6 (a) shows a reconstruction of a typical rat RGC which gave rise to the physiological responses shown in figure 4.6 (b) and (c). The red stain labels the nuclei of all cells in the ganglion cell layer while the green stain fills the soma, dendrites and axon of the recorded retinal ganglion cell (fig. 4.6 (a)). Figure 4.6 (a) shows the cell as it appears in situ in the retina. Based on its morphological features we have identified this as a rat alpha (A2o) ganglion cell (Huxlin and Goodchild, 1997; Sun et al., 2002; Peichl, 1989).

The responses of the RGC imaged in figure 4.6 (a) to stimulation by the N-UNCD electrode are presented in figure 4.6 (b), (c). Electrical stimulation through the N-UNCD electrodes placed upon the surface of the retina adjacent to the recorded cell led to the generation of a stimulus artefact, present in all recordings, and action potentials generated by the recorded ganglion cell. In the raw recordings (fig. 4.6 (b)) stimuli with low intensity were subthreshold for generating action potentials (e.g. 20 μA trace). These subthreshold traces were scaled appropriately to fit the recorded suprathreshold stimuli (60 μA traces) and subtracted from the raw data to reveal the underlying action potentials (fig. 4.6 (c)).

Pulse amplitudes were repeated ten times at a frequency of 1 Hz and the individual spikes extracted as described. Efficacy was defined as the percentage of stimuli that elicited an action potential from 10 repeats delivered at 1 Hz (fig. 4.7). Each panel in figure 4.7 represents the data obtained from four different cells for the three diamond electrodes we tested. Threshold was defined as 50% efficacy and calculated for each cell by fitting the raw data with a two parameter logistic curve. All curves agreed with the raw data to $r^2 \geq 0.93$.

4.4 Discussion

Charging of an electrode surface for neural stimulation should ideally be a non-Faradaic or surface confined Faradaic electrochemical process. Faradaic (electron transfer) processes occurring between an electrode and the biological media or tissue adjacent to the electrode, (e.g. water electrolysis or protein reduction or oxidation) are potentially harmful *in vivo*. The driving force for

undesirable Faradaic reactions is the electrical potential (voltage) of the electrode surface. Two electrochemical parameters are critical when assessing the suitability of material for neural stimulation. The first of these is the electrochemical water window, which is defined as the voltage range inside which cathodic or anodic water electrolysis does not occur. Our activated N-UNCD electrode consistently exhibits a water window between 1.6 and 1.3 V versus Ag/AgCl. This is a wider water window than the most commonly used neural stimulation materials (platinum or iridium oxide, -0.6–0.8 V versus Ag/AgCl from Cogan 2008). Secondly, the electrochemical double layer capacitance or pseudo-capacitance (in the case of electrodes that exhibit surface confined electrochemical reactions, e.g. iridium oxide) must be high. A high capacitance electrode can store a high quantity of charge while maintaining a low voltage. Thus, sufficient charge for neural stimulation can be stored at the electrode surface without risking dangerous electrochemical processes occurring. For almost all previously reported forms of diamond, electrochemical capacitance is very low (Xie et al., 2006; Garrido et al., 2008) making those forms of diamond a desirable material for recording electrodes (Yoshimi et al., 2011; Varney et al., 2011; Suzuki et al., 2007), but unsuitable for stimulation. High capacitance forms of diamond are rare and to date are limited to very highly boron-doped polycrystalline diamond (Watanabe et al., 2010) and N-UNCD (Garrett et al., 2011; Bergonzo et al., 2011).

As previously observed, we measured a substantial increase in charge injection capacity after electrochemical activation by CV from 200 mV to 2.5 V in PBS. Figure 4.4 shows CVs and chronopotentiograms recorded from 600 µm diameter and 200 × 200 µm square N-UNCD electrodes before and after electrochemical activation. Surface capacitance is proportional to the integral area of a CV thus capacitance can be estimated from the anodic and cathodic current magnitude of a CV. The CVs recorded before activation (fig. 4.4 (a) and (c), grey trace) have very low anodic and cathodic current magnitudes and therefore relatively low double layer capacitance. After activation (black traces in figure 4.4 (a) and (c)), the CV current magnitudes increased significantly indicating increased capacitance. There is a discernible Faradaic reduction peak at 0.5 V, which is attributed to dissolved oxygen. Otherwise the CVs are free of any reversible peaks associated with surface confined chemically reversible Faradaic reactions, consistent with diamond electrochemistry and indicate charging via electrochemical double layer capacitance. The voltage traces depicted in figure 4.4 (b) and (d) show the effect of activation on

the electrode voltage excursion during a 100 μA amplitude, constant current, biphasic, 1 ms/phase neural stimulation pulse. The voltage required to drive the pulse before activation (dashed trace) is large in contrast to the activated electrode (black trace) where the voltage required is significantly lower. By pulsing the electrode at currents of increasing magnitude it is possible to define a maximum current amplitude for a given pulse condition by defining a voltage limit (1 V) that the electrode surface must not exceed. It is important to note that the voltage at the electrode surface is represented by the voltage magnitude over which the electrode rises after the initial rapid voltage change as the pulse is applied. This initial sharp voltage change (access voltage) is required to overcome the electrode solution interface impedance and any other resistances in the circuit (according to Ohms law) and thus is not actually present on the electrode surface. The maximum currents at which the capacitive voltage excursions exceed 1 V for 500 μs per phase pulses were approximately 1700 μA for the 600 μm diameter electrodes and 200 μA for the 200 × 200 μm square electrodes which equates to a charge injection capacity of 300 μC cm^{-2} and 250 μC cm^{-2}, respectively. It is unclear why the two types of electrodes exhibited different charge injection values. The N-UNCD sheets used to make the electrodes came from different growth runs and thus may indicate an area where a higher degree of process control is required. These values of 300 and 250 μC cm^{-2} are significantly higher than our previously reported value of 163 μC cm^{-2} recorded using 3 mm diameter N-UNCD electrodes (Garrett et al., 2011). In that work the charge injection capacities were estimated by observation of the slope of the voltage waveforms at moderate current amplitudes in contrast to the empirical method used here. This illustrates that calculated charge injection values from low amplitude current pulses are not good predictors of charge injection limits and represents a flaw in our previous method. The N-UNCD charge injection values of 250–300 μC cm^{-2} measured here are slightly higher than typical platinum values (≈150 μC cm^{-2} in Cogan 2008) but up to an order of magnitude lower than values reported for IrOx (1000–5000 μC cm^{-2} in Cogan 2008).

Calculation of the voltage slope during the anodic phase during pulsing revealed a small but significant drop in charge injection capacity between day 0 and day 1 of continuous pulsing (average 4%). Between 1 and 7 days of continuous pulsing the majority of slope values remained within the 95% confidence interval of the mean indicating no further significant change. This may represent a clear advantage over other materials. Platinum is known to

pit and erode with extended use even when used well inside electrochemical limits (Shepherd et al., 1985; McHardy et al., 1980) and some forms of iridium oxide have been shown to degrade and/or delaminate, particularly when the cathodic voltage excursion exceeds 0.6 V (Cogan et al., 2004; Negi et al., 2010). In all cases the voltage slopes are close to constant during the majority of the pulse indicating that no Faradaic (water electrolysis) processes are occurring. We observed no discernable changes in the surface morphology of the electrodes under SEM after the week of continuous pulsing. Little or no morphological or electrochemical change during prolonged use is an important electrode property because degradation of electrode material over long duty cycles is a potential limiter of device lifetime. Changes in the morphology or electrochemistry over time also represent risk factors because electrode voltages may stray to values that are unsafe *in vivo*. The after use CV shown in figure 4.4 (b) (dashed trace) was recorded after a three week delay and after a reactivation cycle of 3 CVs from 200 mV to 2.5 V versus Ag/AgCl. The CV is very similar to the freshly activated CV indicating very little electrochemical change over the week long stimulation period. A reactivation cycle was required as the charge injection capacity of the electrodes reduced by between 20 and 30% over the three weeks of storage in air. Previously we established by XPS analysis that the strongest predictor of high charge injection capacity in N-UNCD was oxygen concentration in the material and we also showed that electrochemical activation increased oxygen concentration (Garrett et al., 2011). Oxygen functionalization could increase capacitance by specific interactions with the electrolyte (Watanabe et al., 2010). In other work, oxygen functionalization of carbon nanotubes led to a 3.2-fold increase in electrochemical double layer capacitance (Kim et al., 2005) attributed by the authors primarily to an increase in hydrophilicity and electrolyte proton interactions with oxygen functionalities. The loss of charge injection capacity with storage in air is most likely due to adventitious adsorption of carbon species from the air which are readily removed during CV.

Having demonstrated the stability and charge injection capacity of the N-UNCD electrodes, we further sought to establish their utility in activating the ganglion cells of the mammalian retina. When placed epiretinally, close to the somas of the RGCs, the N-UNCD electrodes performed well, activating these cells well below the charge injection limit of 200 μA/500 μs phase (250 μC cm^{-2}). This was true for all recorded RGCs. While the average activation curve for each electrode we tested was quite similar, there was a high degree of

variability within the pool of cells recorded by each electrode (fig. 4.7). This variability in the activation curves may be due to variability in the excitability of different RGC types. It is well established that there are at least 16 different morphological types of RGC in the rat retina (Huxlin and Goodchild, 1997; Sun et al., 2002). Each type is defined by different cellular morphology (size, pattern of dendrites, axon diameter) and is also well known to respond differently to current injection. The variability is well established for both intra- and extracellular stimulation (O'Brien et al., 2002; Sekirnjak et al., 2006; Tsai et al., 2009). Threshold values could also be affected by the position of the recorded RGC relative to stimulating electrode. Uneven tissue on the retina surfaces means some cells may have been further away from the electrode than others. In this work the RGC response latency of approximately 0.6 ms was consistently observed (e.g. figure 4.6 (c)), which is similar to latencies previously reported by Cai et al. (2011) and Sekirnjak et al. (2006). Longer spike latencies of approximately 2 ms were observed by Tsai et al. (2009) after stimulation from a subretinal position.

What is clear from our data is that the diamond electrodes are capable of activating the retinal tissue well within the 200 μA current amplitude limitation (Q_c = 250 μC cm^{-2}). The lowest thresholds of 19–20 μA were observed with two ganglion cells stimulated using electrode 1 (fig. 4.7, Electrode 1, blue and black traces). This equates to a charge injection of 25 μC cm^{-2}, well below the limit of 250 μC cm^{-2} established for the electrode. The highest threshold value of 164 μA was also recorded using electrode 1 (fig. 4.7, Electrode 1, purple trace) and equates to a charge injection value of 205 μC cm^{-2}, which is 82% of the 250 μC cm^{-2} limit. Voltage excursions were not recorded during stimulation owing to equipment limitations but it is reasonable to assume that a voltage of approximately 0.82 V may have been present on the stimulating electrode being 82% of the 1 V limit. Thresholds of 41–133 μA (51–166 μC cm^{-2}) were recorded over the 10 remaining cells, again well inside electrochemical limits. Effective stimulation using voltages lower than 1 V is desirable because, although the defined safe voltage of 1 V is well below the water electrolysis limit, it is unknown what other bioelectrochemistry may be occurring in the 0.6–1 V range. It is difficult to compare our threshold results to other wholemount retinal recordings because our electrodes are very large in comparison to most other studies. The 200×200 μm electrode size was intentionally chosen because it matches the size of the electrodes on the BVA epiretinal device. Tsai et al. (2009) report lowest charge density thresholds of 1430 μC cm^{-2} after subretinal

stimulation of wholemount rabbit retina using a 25 μm diameter Pt-Ir electrode. Sekirnjak et al. (2006) consistently measured thresholds less than 10 μC cm^{-2} using a 14 μm diameter platinum disc array. Though an isolated RGC response does not necessarily lead to a cortical response, it appears that there is no firm evidence for cortical response thresholds being consistently higher than RGC thresholds. The review of Sekirnjak and colleagues covers RGC and cortical thresholds and cites reported values over a wide range between 10 and 1200 μC cm^{-2}. The collated results do not indicate that recording in RGCs or in cortex results in higher thresholds for one technique over the other (Sekirnjak et al., 2006). The range of threshold results is so broad however that firm conclusions cannot be drawn. de Balthasar et al. (2008) report perceptual thresholds between 5 and 750 μC cm^{-2} over 6 human patients fitted with the Argus I device. The Argus I had 16, 260 or 500 μm diameter platinum disc electrodes and was attached in an epiretinal position. In that work they correlate low thresholds with close proximity to the retina.

SEM investigation of the used 200 × 200 μm square electrodes showed limited delamination of the silicone insulation, in particular where it contacted the sides of the diamond electrodes (fig. 4.3 (a)). It is possible that this may have acted as a source of current leakage by increasing the area of diamond exposed to solution. Furthermore, in this case, some N-UNCD would not have been directly in contact with the retina resulting in a low impedance pathway for current leakage. This current leakage would result in higher threshold values due to loss of some charge into the solution rather than through the tissue, causing the measured threshold to be inflated. Despite this potential current loss, our threshold values (25–188 μC cm^{-2}) are at the low end of the spectrum reported by Sekirnjak et al. and are well inside the safe electrochemical limits of the material (250 μC cm^{-2}). The results thus indicate that N-UNCD is electrochemically viable as a material for use in stimulating electrodes for retinal prostheses.

4.5 Conclusions

N-UNCD electrodes were fabricated and electrochemically activated yielding charge injection values over the range of 250–300 μC cm^{-2}. The electrodes exhibited no significant morphological or electrochemical changes after continuous pulsing at the charge injection limit in PBS for one week. N-UNCD electrodes were used to electrically stimulate excised wholemount rat retina

eliciting 50% efficacy activation thresholds between 25 and 188 μC cm^{-2} for RGCs adjacent to the N-UNCD electrode. Despite the possibility of some current leakage, these threshold values are low in the context of existing literature and are well below the safe charge injection limit of 250 μC cm^{-2} for N-UNCD. This is a strong indication that N-UNCD is an electrochemically viable material for retinal stimulation. Combined with the high electrochemical stability exhibited, N-UNCD is a promising electrode material for broad electronic implantable prosthesis applications.

Chapter 5

Optimal Electrical Activation of RGCs

Retinal prostheses seek to restore visual perception in the blind through electrical stimulation of surviving retinal ganglion cells (RGCs). While increased stimulus amplitude often results in greater neural activity, the influence of other waveform parameters such as phase duration on efficacy is unclear. I wished to determine the waveform parameters most effective in activating RGCs using planar electrodes fabricated from nitrogen-doped diamond. Whole-cell patch-clamp recordings from 40 A2-type RGCs were made in retinal whole mount preparations from 26 Sprague-Dawley rats. Membrane potential recordings were amplified, sampled at 50 kHz and stored in digital form. Cells were stimulated using a 200 μm square diamond electrode positioned over the soma and driven by current injection. Stimuli were delivered against a distant monopolar return electrode. Phase duration and polarity had the largest effect on activation thresholds – cells were most responsive to cathodic pulses of short phase duration. Waveform asymmetry and increases in interphase interval further reduced thresholds. Efficacy for 20 Hz and 200 Hz stimulation dropped to ~65% and ~30% of efficacy at 1 Hz respectively by the 20th pulse. These results suggest that a careful choice of electrical waveform parameters can significantly improve prosthesis efficacy.

5.1 Introduction

Retinitis pigmentosa (RP) refers to a family of degenerative eye diseases that ultimately result in blindness, affecting 1.5 million people worldwide (Shintani et al., 2009). While photoreceptors are largely destroyed, significant populations of inner retinal neurons and retinal ganglion cells (RGCs) survive the advanced stages of degeneration (Santos et al., 1997). Vision may be partially restored by means of a retinal prosthesis, which operates by electrically stimulating the surviving retina to evoke visual perception. Several research groups are working towards the development of such a device (see Weiland et al. 2011 for review), with each project employing a particular electrical waveform to elicit a neural response.

It is generally accepted that increasing the amplitude of a stimulus evokes greater neural activity. On the other hand, excessive stimulation can result in damage to the tissue or stimulation apparatus (Merrill et al., 2005; Colodetti et al., 2007). It is therefore desirable to evoke a given neural response using the smallest possible stimulus amplitude. Rectangular, biphasic pulses such as those employed by modern prosthetic devices can elicit more neural activity by extending the duration of each phase. How would this change if the amplitude was scaled such that the charge of the original waveform is preserved? More broadly, can certain waveform parameters be adjusted to bring about a reduction in activation threshold without increasing amplitude? What is the relationship between say, interphase interval and efficacy? I seek to answer these questions by observing the electrophysiological response of RGCs to extracellular epiretinal electrical stimulation using nitrogen-doped diamond electrodes (Hadjinicolaou et al., 2012). In this study I determine which waveform parameters have the greatest effect on charge thresholds and use this information to characterise the most efficacious electrical waveform.

5.2 Methods

5.2.1 Retinal wholemount preparation

Detailed procedures have been described previously (O'Brien et al., 2002; Wong et al., 2012). Data came from 26 pigmented Sprague-Dawley rats ranging in age from 3–5 months. Animals were anaesthetised with a mixture of Ketamine (100 mg kg^{-1}) and Xylazine (10 mg kg^{-1}) and enucleated. Rats were

sacrificed with an overdose of Sodium Pentabarbitone (350 mg, intracardiac) after enucleation. Retinal wholemounts were placed ganglion cell layer up in the recording chamber and held in place with a stainless steel harp fitted with Lycra threads (Warner Instruments, CT USA). Once mounted in the chamber, the retina was perfused (4–6 ml min^{-1}) with carbogenated Ames' medium (Sigma-Aldrich, St. Louis, MO) and heated to 34°C. The chamber was mounted on the stage of an upright microscope (BX51WI, Olympus) fitted with a 40× water-immersion lens. The microscope was fitted with a CCD camera (Ikegami, ICD-48E) used to visualise the retinal tissue on a monitor with 4× additional magnification.

5.2.2 Physiological data collection

To obtain a whole-cell recording, a small opening in the inner limiting membrane and optic fiber layer covering a ganglion cell was first made (O'Brien et al., 2002; Robinson and Chalupa, 1997; Taylor and Wässle, 1995). Large-diameter RGCs with smooth surfaces and agranular cytoplasm that were exposed during this procedure were targeted for recordings. The pipette internal solution contained (in mM): K-gluconate 110, NaCl 5, EGTA 5, HEPES 10, Mg-ATP 4; (mOsm = 282, pH = 7.3) including Alexa Hydrazide 488 (250μM) and biocytin (0.5%). Whole-cell current-clamp recordings were obtained according to standard procedures (Hamill et al., 1981), and the pipette series resistance was measured and compensated for using standard amplifier circuitry. Initial pipette resistance ranged from 3–7 MΩ. Prior to recording, the pipette voltage in the bath was nulled. After obtaining a gigaohm seal and rupturing the cellular membrane, the pipette series resistance was measured again to confirm break-in. Resting potentials were corrected for the change in liquid junction potential (Neher, 1992) that occurs upon break-in and cell dialysis. The liquid junction potential was measured directly as -11 mV. Capacitance compensation (i.e. the use of additional amplifier circuitry to reduce the unwanted low-pass filtering of voltage measurements) was not employed.

Membrane potential was amplified (BA-1S, NPI), digitized with 16-bit precision at 50 kHz (USB-6221, National Instruments) and stored in digital form. Collected data were analysed off-line with custom software developed in MATLAB (MathWorks). Extracellular stimuli were generated by an external constant current source (MCS-4004, Multi-Channel Systems) and delivered through

a single 200 × 200 µm square nitrogen-doped diamond electrode (recently described in Hadjinicolaou et al. 2012) placed upon the inner limiting membrane of the retina immediately adjacent to the recorded cell. Contact with the ILM was evident when surface deformation of the retina could be seen under the microscope. Stimulating electrode resistances varied between 4–6 kΩ. A distant silver chloride-coated silver ball electrode provided an electrical return.

5.2.3 Immunocytochemistry and morphological identification

Following recordings, the retinal tissue was removed from the chamber, mounted onto filter paper, fixed for 45 minutes in phosphate-buffered 4% paraformaldehyde, and stored for up to 2 weeks in 0.1 M phosphate-buffered saline (PBS; pH 7.4) at 4°C. The tissue was subsequently processed to reveal biocytin-filled cells by incubation in 0.5% Triton X-100, 20mg mL^{-1} streptavidin conjugated to Alexa488 (Invitrogen) in PBS overnight at room temperature. Tissue was then washed thoroughly in PBS and stained with propidium iodide for around 8 minutes in order to reveal the boundaries of the inner plexiform layer (IPL) by staining the nuclei of cells in the inner nuclear (INL) and ganglion cell layers (GCL). Samples were again washed in PBS and mounted onto Superfrost slides and protected in 60% glycerol using a coverslip. Cellular morphology was classified after 3D confocal reconstruction (Zeiss PASCAL) using previously established parameters (Sun et al., 2002; Wong et al., 2012).

5.2.4 Experimental protocol

The primary aim of this study was to characterise the most effective electrical waveform for extracellular activation of RGCs. All pulses generated were biphasic and charge-balanced so as to prevent the production of toxic chemical species and maintain electrode integrity (Merrill et al., 2005). Stimulus waveforms were limited to rectangular pulse trains as employed by current-generation retinal prostheses (e.g. Bionic Vision Australia, 2013). Such a waveform can be fully described by five parameters – phase duration (pd_1 and pd_2), asymmetry (defined by phase duration ratio PDR = pd_2/pd_1), interphase interval (ipi), polarity (negative-leading biphasic pulses are referred to as *cathodic first*), and frequency. This study seeks to determine which of these parameters have the greatest effect on efficacy.

Prior to performing the experiment, each cell was subjected to brief depolarizing currents delivered by way of the recording pipette to ensure viability of the cell and stability of the recording. Viable cells, which produced a robust response (consistency and positive spike overshoot) to intracellular current injection, were then subjected to further investigation using extracellular stimulation. An electrical pulse delivered through the stimulating electrode that managed to elicit a cellular response almost always evoked a single spike, although bursts of two or three spikes were observed on occasion. A limited number of trials were affected by membrane potential fluctuations that significantly increased (by a factor of at least 50%) the number of evoked spikes for a given stimulus. Additional trials were collected in these instances.

The first stage of the experiment, the *fractional factorial* (FF) protocol, surveyed a relatively large parameter space to address the question of which waveform parameters have the greatest effect on activation thresholds. Here, threshold was defined as the amount of charge per phase required to elicit 40–50% efficacy. Efficacy is defined here as the percentage of delivered stimuli that evoke at least one spike. The subsequent *waveform optimisation* (WO) protocol then used broad findings from this parameter survey to inform the design of a *baseline waveform* from which further refinement would result in a waveform optimised for extracellular RGC activation. Starting with this baseline waveform, stimulus waveform parameters were optimised to maximise efficacy. In protocol sections where frequency was fixed, each trial comprised ten pulses delivered at a rate of 2 Hz. Each stimulus condition was repeated at least three times unless otherwise noted. In the final *frequency* protocol, where the effect of stimulus frequency was investigated, at least two trials for each stimulus condition were collected.

Fractional factorial protocol

A minimal set of 12 electrical waveforms (table 5.1) defined by a fractional factorial design (see Gunst and Mason, 2009) was used to test four levels of first-phase duration (pd_1 = 60 µs, 200 µs, 340 µs, 480 µs), four levels of asymmetry (PDR = 1, 2, 3, 4), four levels of interphase interval (ipi = 60 µs, 240 µs, 420 µs, 600 µs) and polarity (anodic-first and cathodic-first). The waveforms were presented in random order and delivered at a fixed frequency of 2 Hz. Threshold amplitudes were evaluated by adjusting current amplitude until at least two consecutive trials exhibited 40–50% efficacy.

Table 5.1. The set of waveform parameters used in the FF protocol. Phase durations and interphase interval are in units of microseconds. Cathodic-first pulses are indicated with a minus symbol, anodic-first with a plus symbol.

n	pd_1	pd_2	ipi	pol
1	200	400	240	−
2	200	400	240	+
3	60	180	420	−
4	200	600	600	+
5	480	480	420	−
6	480	1920	60	+
7	480	1440	60	−
8	340	340	420	+
9	60	240	240	−
10	340	1360	600	+
11	340	680	600	−
12	60	60	60	+

Waveform optimisation protocol

Broad findings from the FF protocol were used to define a *baseline waveform* consisting of a symmetrical, cathodic-first pulse of 120 µs phase duration with no interphase interval. Beginning with this baseline waveform, the following procedure was then used to derive the *optimal waveform*:

1. Find threshold (40–50% efficacy) for the baseline waveform.
2. Test interphase intervals from 0–800 µs using threshold amplitude.
3. Update the baseline waveform with the most effective value of interphase interval between 0–100 µs, for threshold amplitude.
4. Test phase durations of 60 µs, 120 µs, 240 µs, 480 µs.
   (a) Find threshold amplitude I_{th} for the updated baseline waveform, where ($pd_1 = pd_2 = 120$ µs).
   (b) Test all phase duration combinations for both phases while preserving the charge per phase ($I_{th} \times 120$ µs) of the previous waveform (see fig. 5.1).
5. Update the baseline waveform with the most effective phase durations.
6. Define this waveform as the optimal waveform.

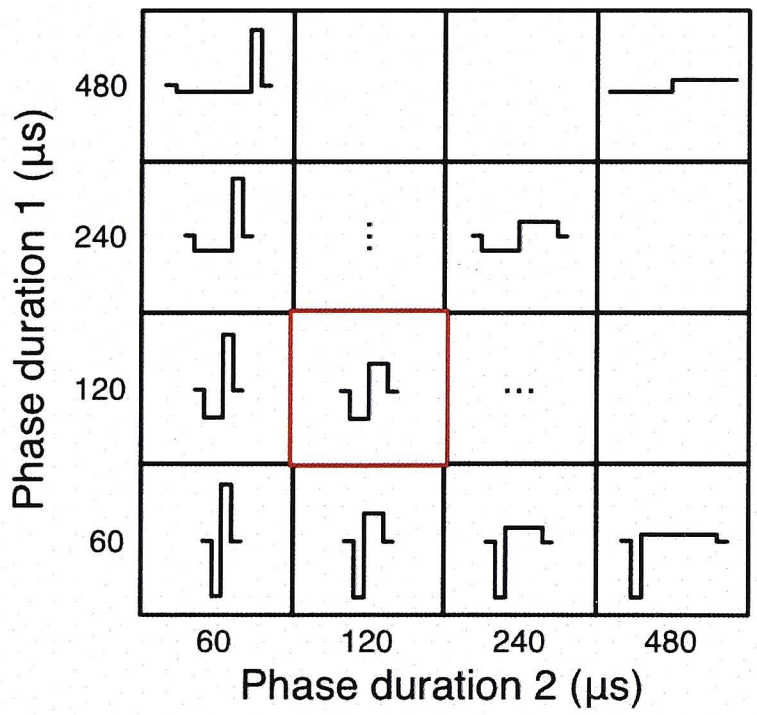

Figure 5.1. An illustration of the waveform matrix delivered during the phase duration optimisation stage. Phase durations of 60 µs, 120 µs, 240 µs, and 480 µs were tested for both phases. The waveform highlighted by the red box indicates the baseline waveform at threshold amplitude. All waveforms maintain the per-phase charge of the baseline waveform.

Frequency protocol

The optimal waveform, scaled to reach suprathreshold (90–99% efficacy) at 1 Hz, was then used to investigate the effect of stimulus frequency. Pulse trains containing a maximum of 50 pulses were then delivered for stimulation frequencies ranging from 1–200 Hz. At each stimulus frequency, efficacy was quantified as the percentage of stimulus pulses that evoked an action potential.

5.2.5 Data analysis

All data analysis was performed using custom software developed in MATLAB (MathWorks). Efficacy curves were generated by fitting a two-parameter logistic function to the data. In all cases, efficacy was defined at the proportion of stimulus events which evoked at least one action potential from the recorded cell. To explore the effect of cell morphology, two subsets of cells (*large* and *small*) were identified on the basis of either a) dendritic field size, or b) soma size. Cells with dendritic field diameters exceeding 460 µm were designated as large cells, while cells with dendritic field diameters less than 360 µm were designated as small cells. In terms of soma size, cells were defined as large if their soma diameters were 23 µm or greater, while diameters of 20 µm or less were classified as small. Efficacy for these large- and small-cell subsets was calculated by averaging efficacy over two analysis windows. At each stimulus

frequency the duration of the analysis windows was such that each contained 10 stimulus pulses. Thus, at 5 Hz, each window was 2 seconds in duration while at 50 Hz each window was 0.2 seconds in duration. The start of the first (or *early*) window was coincident with the onset of the stimulus pulse train. The start of the second (*late*) window was delayed, with respect to the first, by an interval equal to the window duration. In effect, the early window quantified efficacy over pulses 1–10 of the stimulus pulse train while the late window quantified efficacy over pulses 21–30.

Efficacy for large and small cells was compared within these windows at each stimulus frequency tested. The statistical significance of any observed difference in efficacy between large and small cells was determined with a random permutation test (Efron and Tibshirani, 1993). Specifically, efficacy within the two analysis windows was calculated for each cell. Cells were then randomly assigned to one of two groups with the size of the two groups being equal to the size of the original large and small cell groups (i.e., group assignment was randomly permuted). Efficacy was then averaged across cells within each group and the difference calculated. This permutation of group assignments was performed a minimum of 10,000 times, resulting in a null distribution of the expected difference in mean efficacy assuming cell size had no effect. The observed difference in the unpermuted data (i.e., the difference in the mean efficacy averaged across the original subsets of large and small cells) was deemed significant if the proportion of samples in the null distribution which exceeded the observed difference was less than 5% (i.e., $p < 0.05$).

Multilinear regression (`regress` in MATLAB) was used to construct a model for charge thresholds using data from the FF experiment. All model coefficients were nonzero over a 95% confidence interval. The relationship between soma diameter and dendritic field diameter ($\rho = 0.383, p = 0.028$) was confirmed by computing Pearson's linear correlation coefficient.

5.3 Results

We recorded physiological responses from 48 RGCs of which 40 could be classified as A2-type after morphological reconstruction. The remaining eight cells were determined not to be A2 cells but were otherwise unclassified. Attempts were made to obtain a complete set of data for each cell, however this was not always possible as the entire experimental protocol typically required more

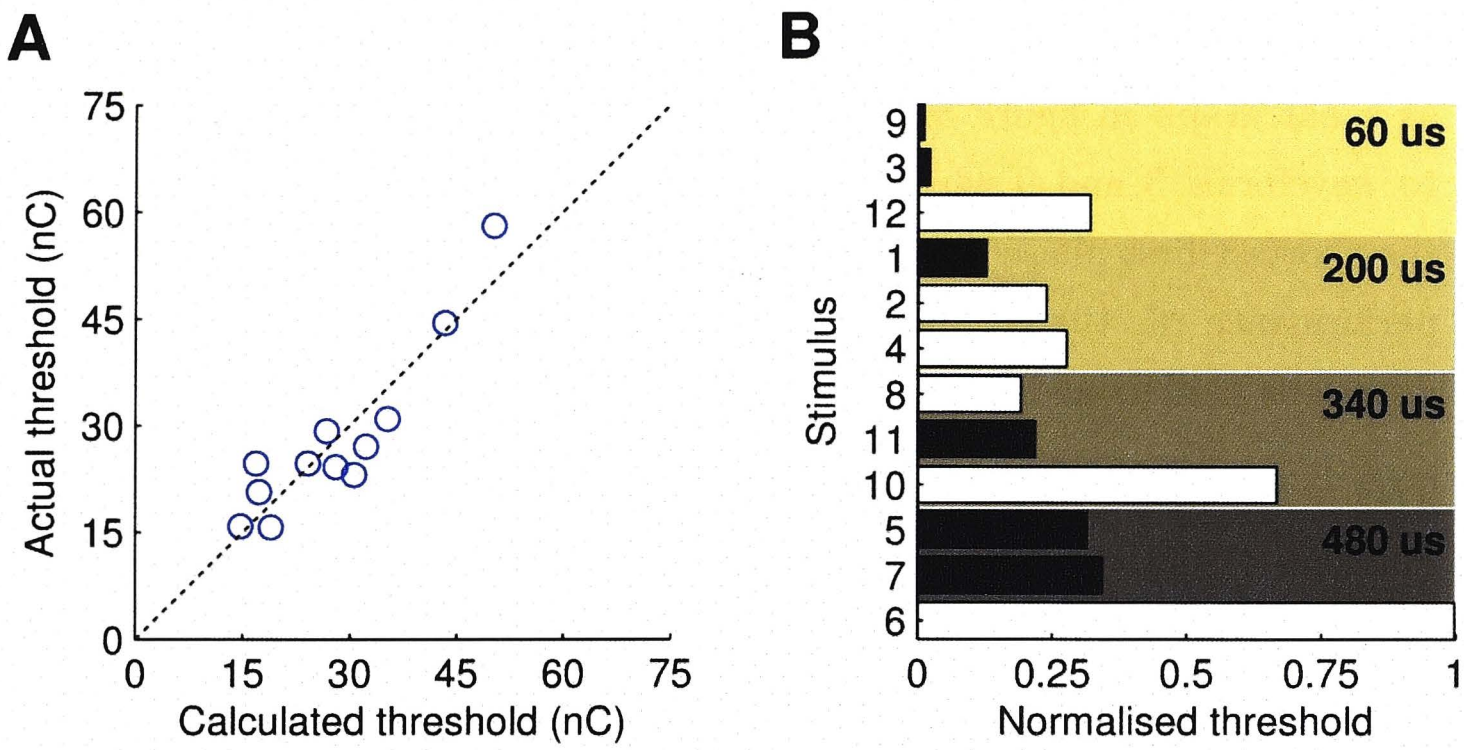

Figure 5.2. (A) Actual versus calculated charge thresholds. (B) Normalised charge thresholds averaged across all cells. White bars indicate anodic-first stimuli and black bars indicate cathodic-first stimuli. The data are ordered by increasing first-phase duration, which is listed for each group. The stimulus numbering scheme corresponds with that of table 5.1.

than two hours to perform and recordings were sometimes lost prior to completion.

5.3.1 Fractional factorial protocol

Multilinear regression was used to describe a relationship between several waveform parameters and charge thresholds ($r^2 = 0.831$) from 29 A2 RGCs. The charge thresholds associated with each stimulus waveform were averaged across all cells. The analysis found first-phase duration, polarity, and asymmetry to be significant factors (i.e. nonzero over a 95% confidence interval) in determining charge thresholds, for which a regression line was fitted and described by

$$Q_{th}(pd_1, pd_2, pol) = 4.4 + 0.045 \cdot pd_1 + 4.3 \cdot \frac{pd_2}{pd_1} + 5.4 \cdot pol,$$

where phase durations are in units of microseconds, charge thresholds are in units of nanocoulombs, and polarity is either -1 (cathodic) or +1 (anodic). Figure 5.2 (A) demonstrates the agreement between calculated and average experimental charge threshold for each of the twelve tested waveforms. We can better assess the relative efficacy of each waveform by normalising charge thresholds such that for each cell, the lowest threshold has a value of 0 and

the highest a value of 1. This data is averaged across all cells and displayed as a bar graph in figure 5.2 (B). We observe that cells are most responsive to waveforms 3 and 9 which are both cathodic-first, asymmetric, and have the shortest first-phase duration (60 μs). The two waveforms with the worst performance (6, 10) are anodic-first, asymmetric, and have long first-phase durations (340 μs and 480 μs).

This parameter survey demonstrates that cathodic pulses of short first-phase duration are effective in evoking neural activity with minimal charge. However, the effects of asymmetry and interphase interval remain unclear. Based on this result, the baseline waveform is defined as a symmetric, cathodic-first pulse of 120 μs phase duration with no interphase interval. This baseline waveform provided a starting point for the waveform optimisation.

5.3.2 Waveform optimisation protocol

Efficacy and strength-duration

The median current required to reach activation threshold was 171 μA for the baseline waveform. Efficacy curves for each cell are plotted in figure 5.3 (A). All fitted curves had an r-squared of > 0.9, with the median value being 0.99. Strength-duration curves (fig. 5.3, B) were generated for each cell by varying the phase duration (40–480 μs) of a symmetric pulse with no interphase interval. Threshold-vs-duration followed a power law ($r^2 > 0.99$) described by

$$I_{th}(pd) = 5.6 \times 10^4 \cdot pd^{-1.3} + 42,$$

where threshold current is in units of microamps, and phase duration is in units of microseconds.

Interphase interval

To evaluate the impact of interphase interval on waveform efficacy, we first found threshold amplitude for the baseline waveform (40-50% efficacy), which had no interphase component. We then added progressively longer interphase intervals and examined the consequent change in efficacy for these two amplitudes. The data (fig. 5.4) show that efficacy was improved with the inclusion of an interphase interval. At threshold amplitude, efficacy increased on average from 44% to 66% when increasing the interphase from zero to 20 μs. An

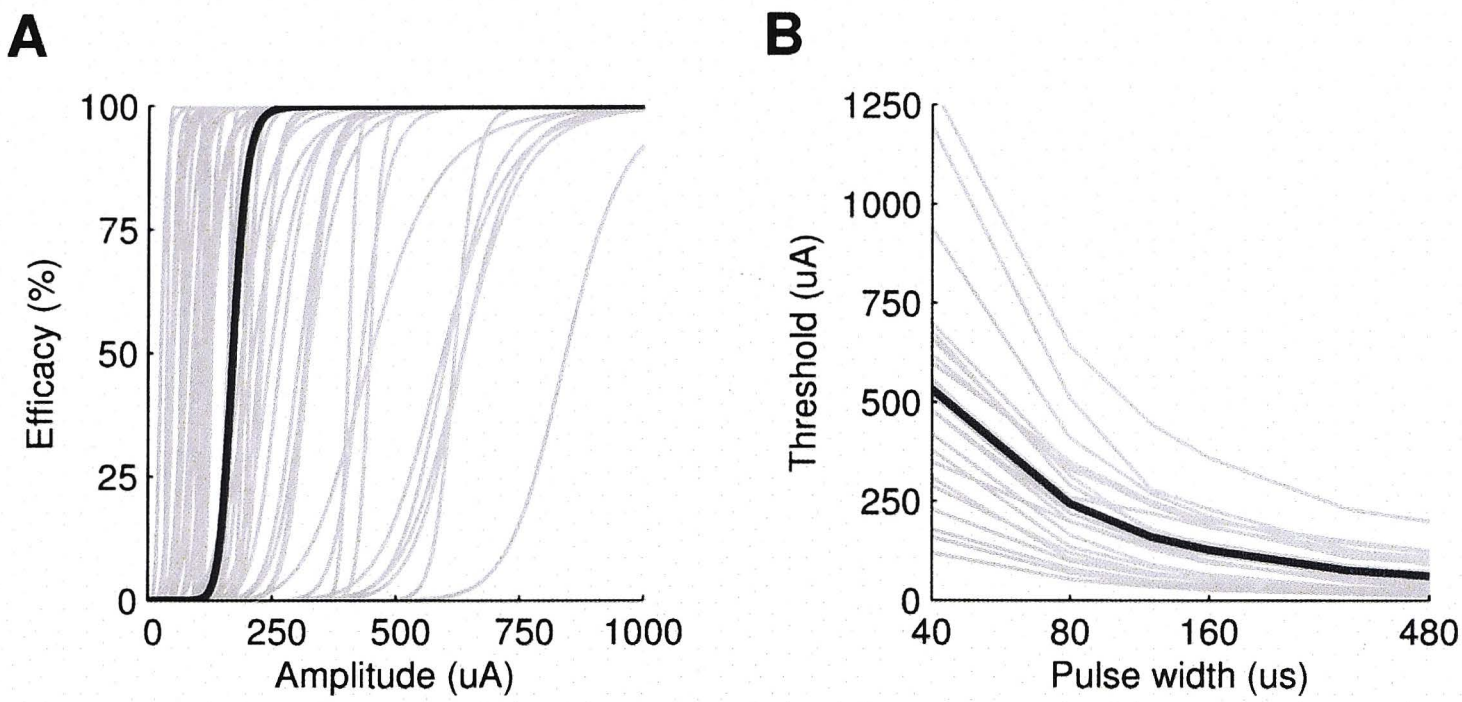

Figure 5.3. (A) Efficacy curves ($n = 48$) fitted to experiment data. The median efficacy curve is indicated by the thick dark line. (B) Strength-duration curves ($n = 23$). The average S-D curve is indicated by the thick dark line.

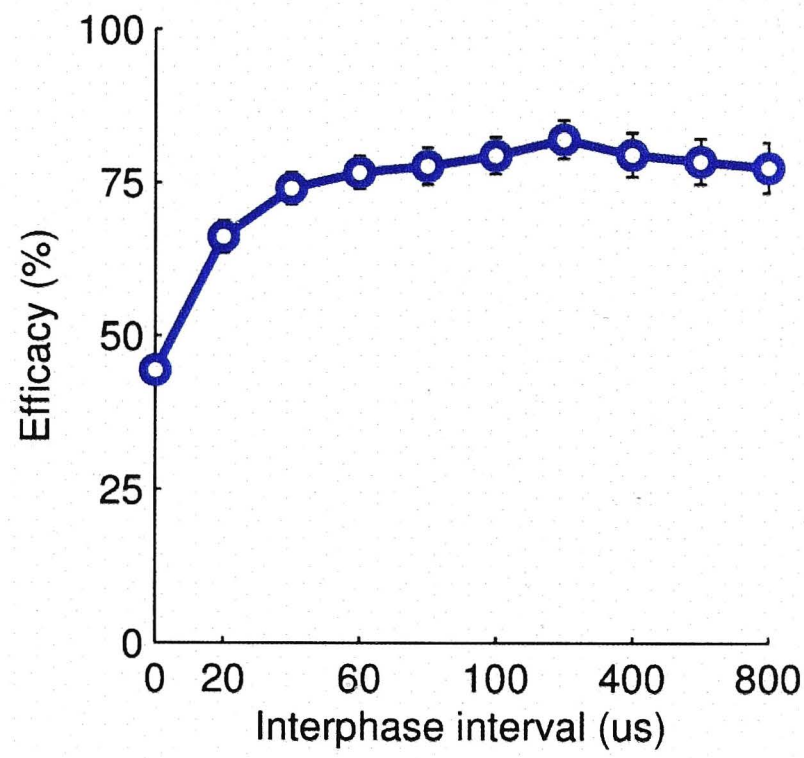

Figure 5.4. Efficacy as a function of interphase interval ($n = 48$). Error bars indicate plus/minus one standard error. Note that while addition of short interphase intervals (< 100 μs) does increase efficacy, longer durations have little effect.

additional increase to 40 μs interphase increased efficacy up to 74%. Additional interphase beyond 40 μs yielded trivial improvement. It is clear from the plot that although a short interphase interval serves to reduce activation thresholds, gains in efficacy saturate for values greater than 100 μs.

Asymmetry

Prior to optimising stimulus waveform asymmetry, the baseline waveform was updated using the optimal interphase interval. Threshold current amplitude was then determined for this updated baseline waveform. Phase durations of

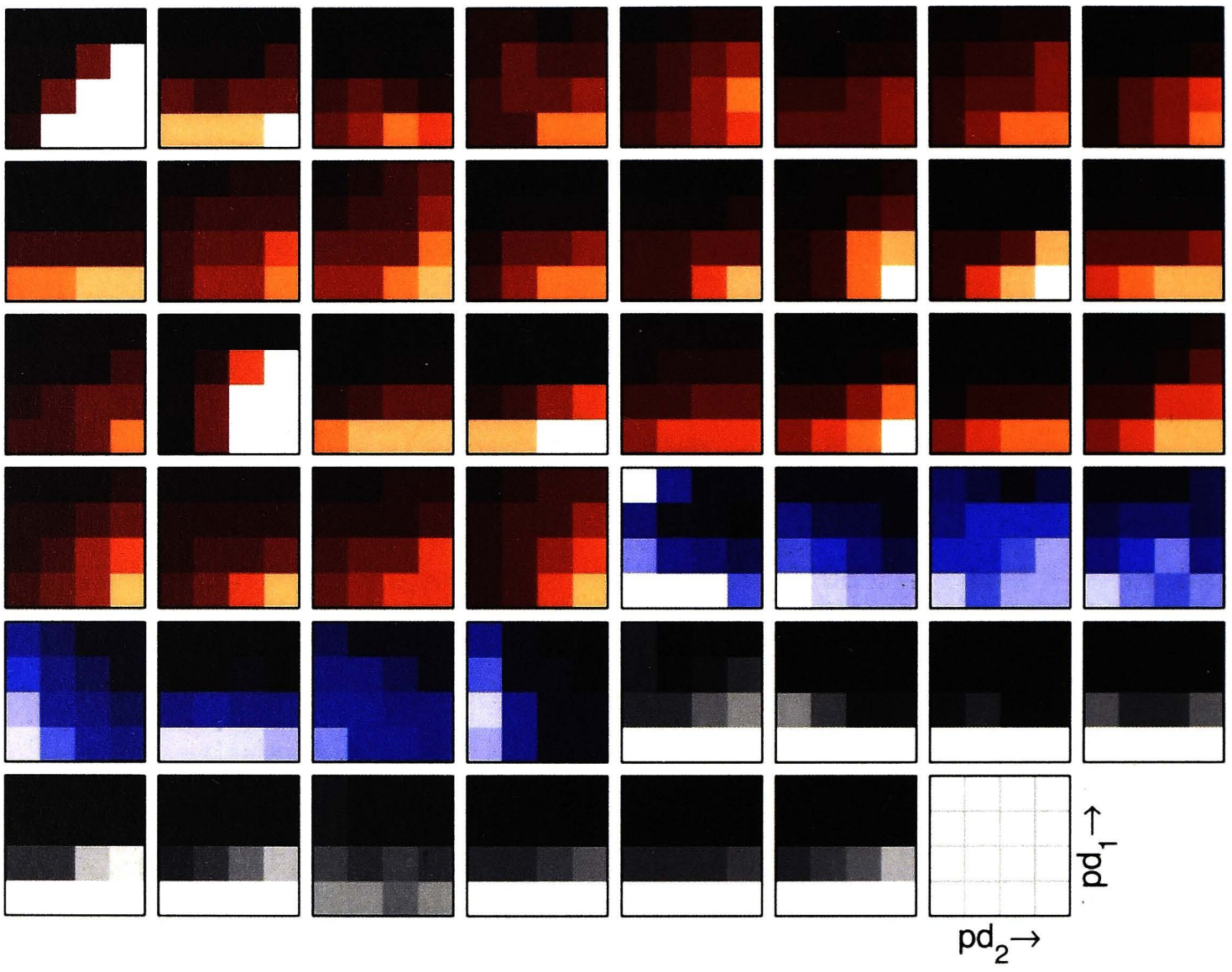

Figure 5.5. Efficacy as a function of phase duration for the waveform matrix ($n = 46$). Red: asymmetric waveform preference. Blue: symmetric waveform preference. Grey: short first-phase duration preference. Lighter shading indicates greater efficacy. Arrows in waveform matrix sketch indicate increasing phase duration.

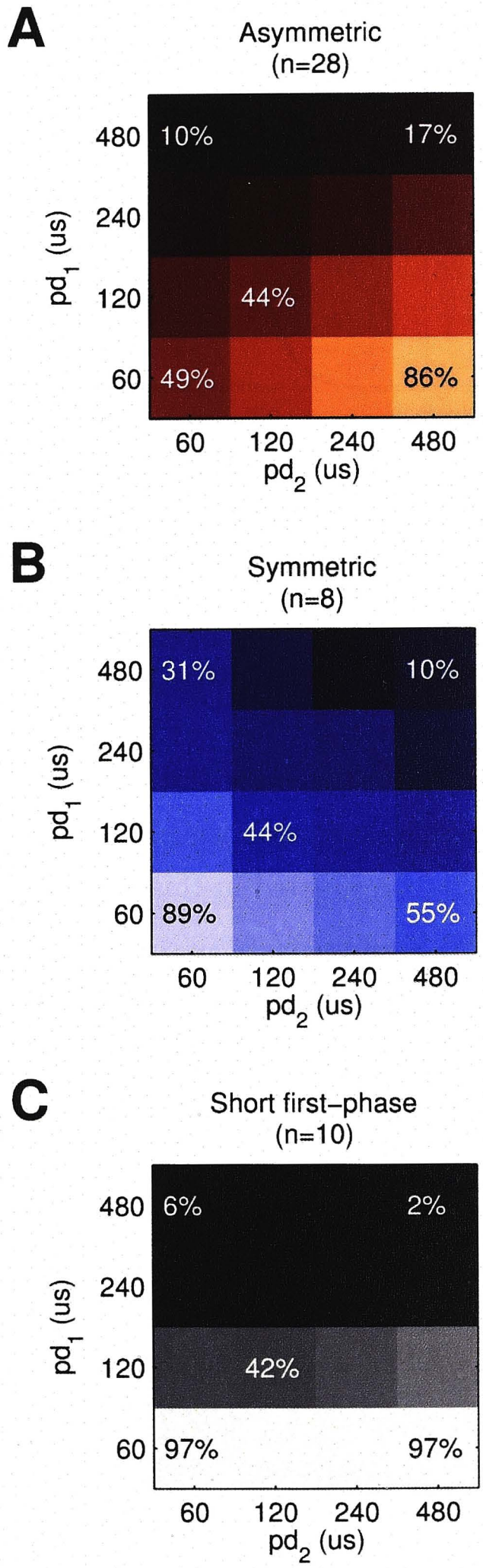

Figure 5.6. Average efficacy as a function of phase duration for the waveform matrix, for each response category. Efficacy for selected waveforms is indicated as a percentage for clarity. Lighter shading indicates greater efficacy. Most cells responded preferentially to the asymmetric waveform with (pd_1, pd_2) = (60 µs, 480 µs).

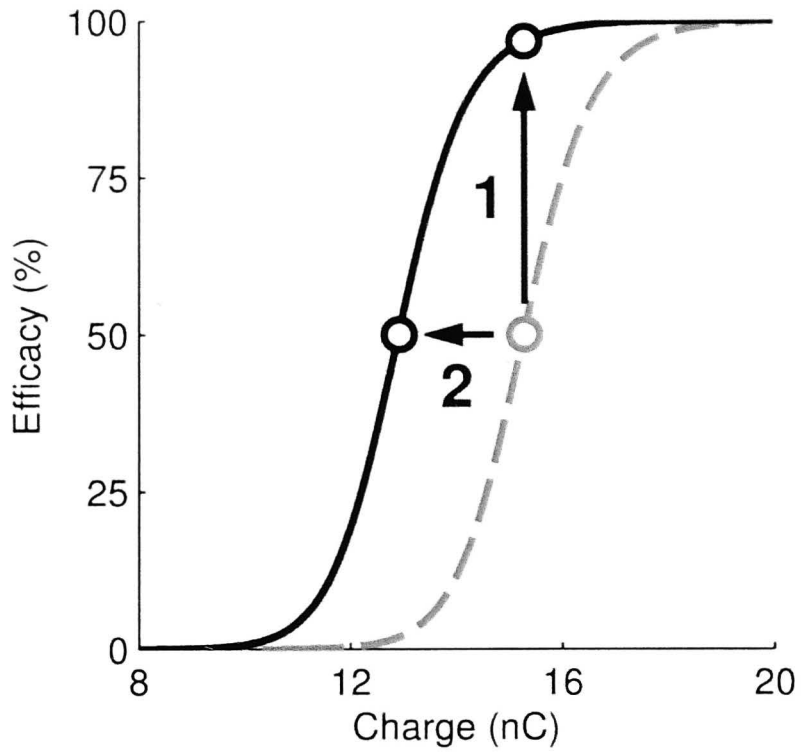

Figure 5.7. Charge savings for an example cell. Efficacy for the baseline stimulus waveform (dashed grey curve) can be improved by either increasing the injected per-phase charge (arrow 1) or by optimising for interphase interval (arrow 1). The charge savings achieved after optimisation effectively shift the efficacy curve to the left (arrow 2, solid black curve).

60 µs, 120 µs, 240 µs and 480 µs were tested for each phase, preserving the per-phase charge of the baseline waveform. Figure 5.1 shows an illustration of the 4×4 waveform matrix evaluated in this protocol section. Figure 5.5 uses the same representation to indicate average efficacy for the waveform matrix, showing the responses from 46 cells. A given cell was said to have a preference for the asymmetric waveform (pd_1, pd_2 = 60 µs, 480 µs) if its associated efficacy was at least 10 percentage points higher than that of the symmetric waveform ($pd_1 = pd_2 = 60$ µs). Such cells are indicated in figure 5.5 (red shading). The responses of all cells that meet this criterion were averaged, resulting in figure 5.6 (A). Similarly, cells that preferred the symmetric waveform (fig. 5.5, blue shading) and those that responded to both waveforms with similar efficacy (fig. 5.5, grey shading) were grouped into their respective categories and their responses averaged (figures 5.6 B, C). The number of cells that belong to each category is indicated in parentheses in figure 5.6. Over the range of phase durations considered, the shortest first-phase duration of 60 µs always gave rise to lower activation thresholds and the majority (63%) of cells responded best (red shading) when stimulated with a highly asymmetric waveform (PDR = 8; fig. 5.6 A). A smaller proportion (15%) of cells preferred symmetrical pulses (PDR = 1, fig. 5.6 B).

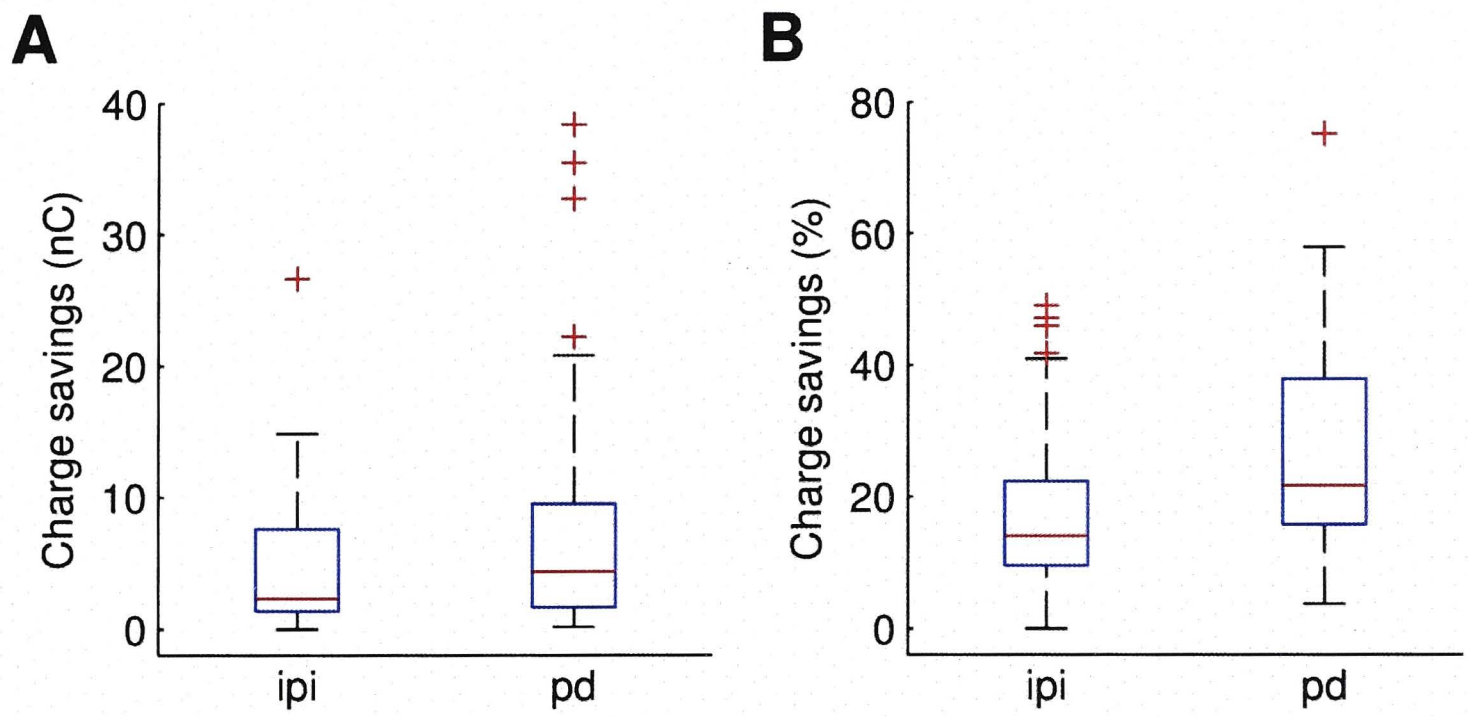

Figure 5.8. Per-phase charge savings after waveform optimisation ($n = 46$). (A) Raw charge savings. Median charge savings after optimising ipi and pd were 2.4 nC and 4.4 nC respectively. (B) Charge savings as a percentage of the pre-optimisation charge. Median charge savings after optimising ipi and pd were 14% and 22% respectively.

Relating efficacy to charge

We can translate increases in efficacy to per-phase charge savings by using the efficacy curve generated at the start of the experiment to determine a) the threshold current before optimisation, and b) the amount of current required to achieve the same efficacy after optimising the relevant parameter. The current difference is then converted to charge and expressed as a percentage of the per-phase charge before optimisation. An example of this procedure is shown in figure 5.7. The efficacy curve for a single cell, generated using the baseline waveform parameters (c.f. fig. 5.3 A) is shown by the dashed grey curve. The efficacy curve for this cell after optimising the interphase interval is shown by the solid black curve. The threshold criterion (50% efficacy) prior to waveform optimisation defines the baseline-per-phase charge (15.3 nC). After waveform optimisation, efficacy at this per-phase charge was increased from 50% to 97% (arrow 1). The amount of additional charge that would be required to generate an equivalent efficacy using the baseline waveform (2.4 nC) is then interpreted as charge saved. Waveform optimisation effectively shifts the efficacy curve to the left (arrow 2).

Figure 5.8 shows a box-and-whisker plot for charge savings as a result of optimising interphase interval and phase duration. Optimising interphase interval led to median charge savings of 14% and optimising phase duration resulted in median charge savings of 22%.

5.3.3 Frequency protocol

The optimal waveform, obtained after optimising the interphase interval and phase duration of the baseline waveform, was used to test the effect of stimulus frequency on efficacy. Increased stimulation frequency resulted in decreased efficacy. Figure 5.9 (A) plots efficacy as a function of pulse number for frequencies ranging from 5–200 Hz. Efficacy decreases for consecutive stimulus pulses, converging to a frequency-dependent level after approximately 20 pulses. By the 20th pulse, efficacy for 20 Hz and 200 Hz had fallen to roughly 65% and 30% of efficacy at 1 Hz, respectively. The effect of frequency on suprathreshold current, or the amplitude required to elicit 90–99% efficacy was also investigated. Figure 5.9 (B) plots the relationship between frequency and suprathreshold current ($n = 10$), expressed here as a multiple of that required for 1 Hz stimulation.

5.3.4 Morphology

Morphological differences within the single cell type considered in this study were found to contribute to differences in ability to keep up with repetitive electrical stimulation. Figure 5.10 demonstrates that cells with small and large dendritic fields (DFs) exhibit differences in their ability to sustain stimulation at high frequency. Over the duration of the early analysis window (first 10 stimulus pulses, fig. 5.10 A), cells with smaller DFs are highly responsive to stimulation over all frequencies. Conversely, cells with large DFs managed to respond to only half of these stimuli by 100 Hz. This difference persisted over the duration of the late analysis window (pulses 21–30, fig. 5.10 B), where small cells could again better sustain activation at the highest stimulation frequencies tested. A similar analysis was performed based on soma size. Again, smaller cells were found better able to sustain high frequency stimulation (fig. 5.11). These findings may be of consequence for retinal prosthesis patients if larger RGCs are found to be more susceptible to RP-induced degeneration, as Quigley (1998) found in his study of glaucoma.

Morphology was otherwise not found to significantly influence the response to electrical stimuli in this study. A histogram illustrating the distribution of large and small dendritic fields is shown in figure 5.10 (C). The distributions of large DF (red) and small DF (blue) efficacy curves in figure 5.10 (D) suggest that thresholds were largely independent of cell size (Wilcoxon rank sum test,

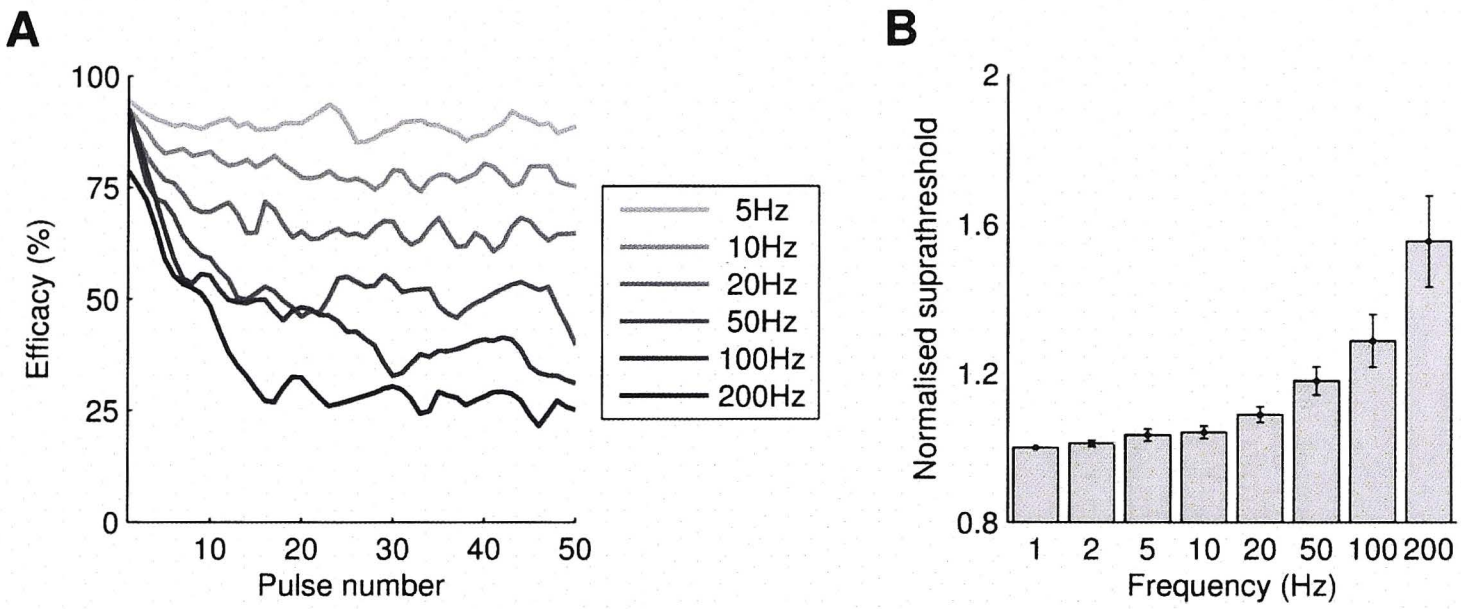

Figure 5.9. Frequency dependence of stimulation. (A) Efficacy, plotted against consecutive pulse number, falls with frequency ($n = 37$). Curves were treated with a moving average (five points). (B) Normalised suprathreshold current as a function of frequency. Error bars indicate plus/minus one standard error.

$p = 0.097$). Similarly, no significant differences were found between the optimal interphase interval and phase durations of large and small cells.

5.4 Discussion

This study sought to determine the waveform parameters of greatest influence on RGC activation thresholds and then characterise the most efficacious electrical waveform. The main findings may be summarised as follows: 1) cathodic-first, short-phase stimuli have lower charge thresholds than anodic-first stimuli, 2) the effect of asymmetry depends on phase duration, and 3) morphological differences between cells are correlated with the ability to sustain repetitive stimulation at high frequency.

5.4.1 Waveform parameters

Stimuli delivering more charge are more likely to evoke a biological response. Activation thresholds for the 120 μs per phase baseline waveform of the present study were found to be lower (median of 21 nC) in comparison to that observed in Chapter 4 (also Hadjinicolaou et al., 2012), where the median charge threshold of 41 nC was found for the 500 μs per phase waveform. Despite restricting observations to a single cell type, activation thresholds were found to exhibit substantial variation in these experiments, ranging from 3 nC to the highest value of 101 nC. In Chapter 4, which did not control for cell type, the smallest and largest thresholds were 10 nC and 82 nC, respectively.

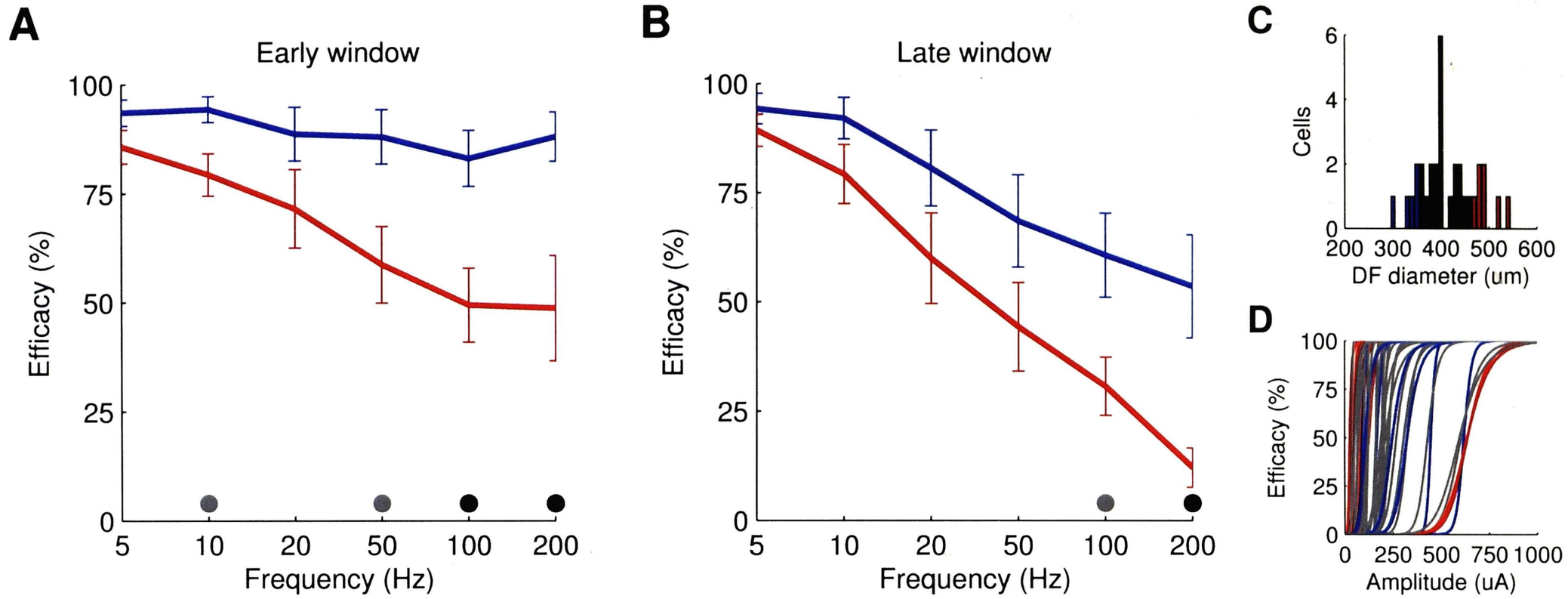

Figure 5.10. (A, B) Differences in frequency response as related to dendritic field size. Small DF diameters are defined as being < 360 µm $(n = 7)$, large DF diameters > 460 µm $(n = 7)$. Error bars indicate plus/minus one standard error. Grey and black dots indicate statistically significant differences in the responses of the two cell populations ($p < 0.05$ and $p < 0.01$, respectively). (A) considers efficacy over the early analysis window (first 10 stimuli pulses), while (B) considers pulses over the late analysis window (pulses 21–30). (C) Histogram of DF diameter distribution. Red: large DFs, blue: small DFs. (D) Efficacy curves (as in fig. 5.3), highlighting data from large DF (red) and small DF (blue) cells.

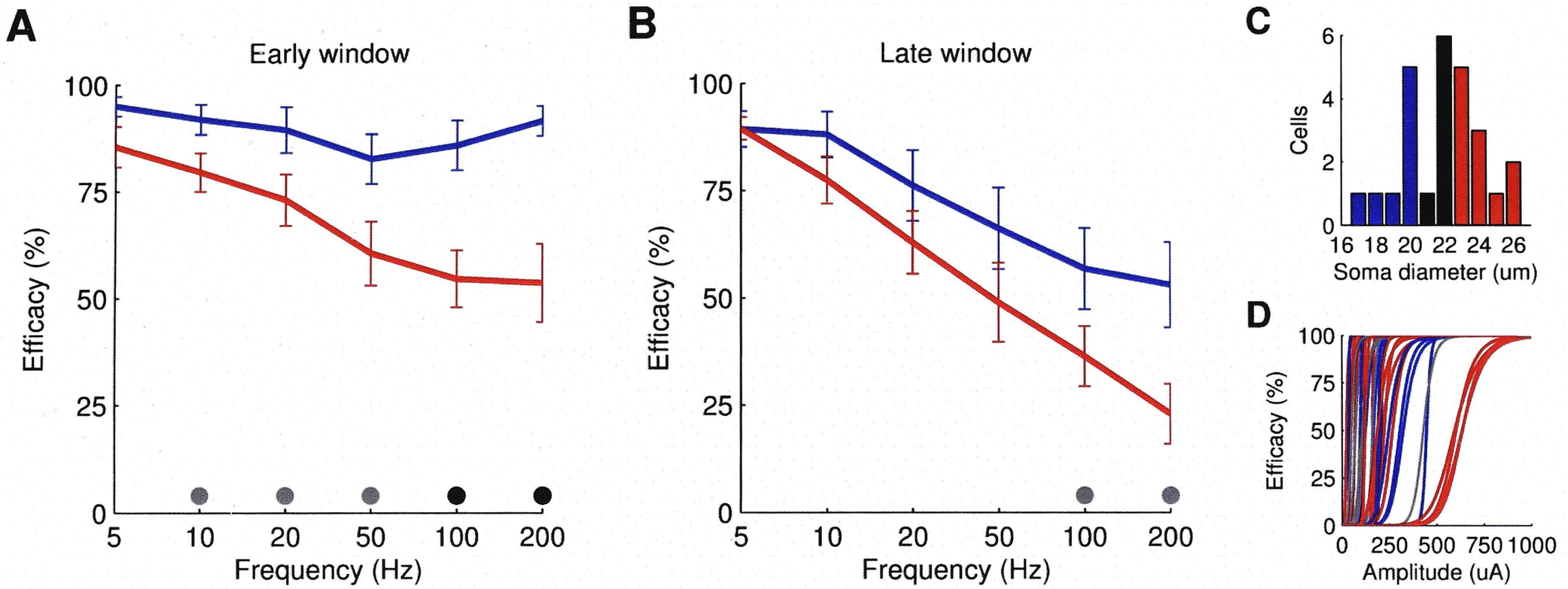

Figure 5.11. (A, B) Differences in frequency response as related to soma size. Small soma diameters are defined as being ≤ 20 µm $(n = 8)$, large soma diameters ≥ 23 µm $(n = 11)$. Error bars indicate plus/minus one standard error. Grey and black dots indicate statistically significant differences in the responses of the two cell populations ($p < 0.05$ and $p < 0.01$, respectively). (A) considers efficacy over the early analysis window (first 10 stimuli pulses), while (B) considers pulses over the late analysis window (pulses 21–30). (C) Histogram of soma diameter distribution. Red: large somas, blue: small somas. (D) Efficacy curves (as in fig. 5.3), highlighting data from large soma (red) and small soma (blue) cells.

Cathodic-leading pulses were found to be more effective than anodic-leading pulses. This finding has been predicted by neuronal modelling (Rattay, 1999) and validated experimentally in studies of auditory nerve fibres (Shepherd and Javel, 1999) and isolated retinae (Sekirnjak et al., 2006). There have, however, been cases in which lower activation thresholds were observed for anodic-first pulses (Jensen and Rizzo III, 2006). The authors found that activation thresholds for subretinal electrical activation of ON RGCs in the rabbit were not significantly influenced by stimulus polarity, while OFF RGCs required on average 2–7.5 times more current to reach threshold using cathodic-first stimulation compared with anodic stimulation.

Short phase durations yielded lower activation thresholds compared to longer phase durations with identical charge per phase. The reduction in pulse efficiency (i.e. efficacy for a given per-phase charge injection) with phase duration has been established previously (e.g. Rattay et al., 2012).

Stimulus waveform asymmetry has been observed to reduce charge thresholds in cat and guinea pig auditory nerve experiments (Shepherd and Javel, 1999; Miller et al., 2001) and was proven to be inconsequential in the study of Koivuniemi and Otto (2011), which employed intracortical stimulation of the rat auditory cortex. In my *in vitro* study, the effect of asymmetry largely depends on the duration of the first phase. The regression line fitted to data collected in the fractional factorial protocol predicts that charge thresholds increase with asymmetry and yet the two most effective waveforms are asymmetric. This is illustrated in figure 5.12, which plots normalised charge threshold against first-phase duration for four different levels of waveform asymmetry. This plot suggests that asymmetry serves to reduce charge thresholds if the first-phase duration is small enough (left-most points shown in red in fig. 5.12). Results from the phase duration optimisation stage depicted in figure 5.5 support this assertion – over the range of phase durations considered (60–480 µs), the shortest first-phase duration always gave rise to the smallest charge thresholds, which were usually reduced further with a PDR > 1.

Waveform efficacy improves with greater temporal separation between each phase. The increase in interphase interval from zero to 20 µs offers the largest gain in efficacy (22% increase; fig. 5.4) with successive steps resulting in smaller gains. Increasing interphase interval beyond 100 µs offers negligible improvement in threshold. These findings were made in the WO protocol and explain why interphase interval was not recognized as a significant parameter in the

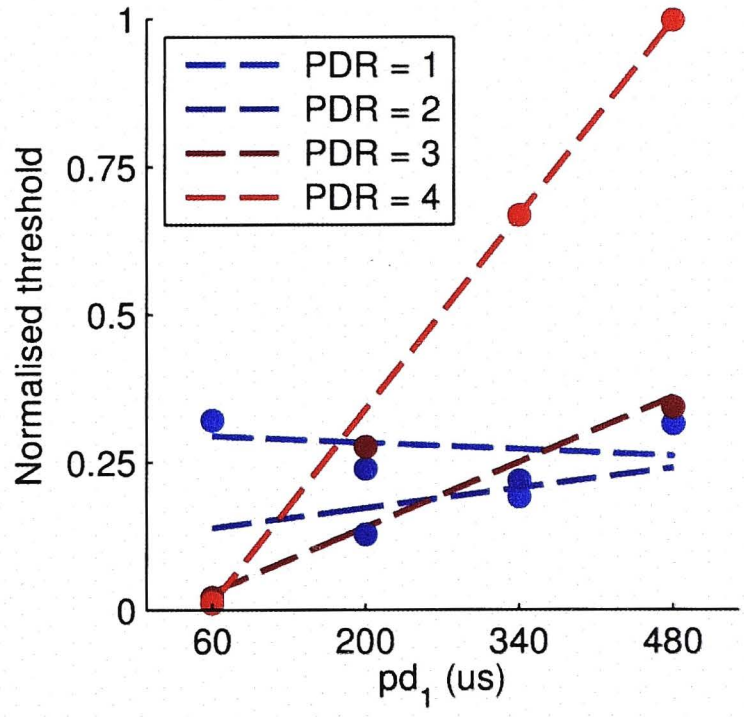

Figure 5.12. Normalised charge thresholds from the fractional factorial protocol and their relation to PDR and first-phase duration, regardless of other parameter values. PDR $= \{1, 2, 3, 4\} = \{$blue, dark-blue, dark-red, red$\}$. The gradients of the fitted lines suggest that threshold dependence on phase duration is intensified by asymmetry.

FF protocol analysis – any difference in threshold caused by moving between the two smallest values of interphase interval considered (60 µs and 240 µs) would have been dominated by the effects of polarity and phase duration. The observation that interphase interval improves efficacy is congruent with previous reports by investigations in the cat, guinea pig, and tiger salamander (Shepherd and Javel, 1999; Prado-Guitierrez et al., 2006; Weitz et al., 2011).

My finding that waveform efficacy decreases with stimulus frequency is consistent with that of other studies performed using isolated rabbit retina (Jensen and Rizzo III, 2007; Tsai et al., 2009; Freeman and Fried, 2011). These studies classified cells into ON and OFF categories but reported no significant difference between the ability of each broad cell type to sustain repetitive stimulation. There may be a connection between this phenomenon and the fading of visual percepts over time in human implant subjects. As contemplated by Freeman et al. (2011), this fading may arise from the desensitisation of a certain proportion of cells, as opposed to the entire ganglion cell population. My data demonstrate that variability in soma and dendritic field size has a substantial effect within cells of a single morphological type, suggesting that this desensitised proportion of cells may be distinguished by size. Suprathreshold current was also seen to increase with frequency, roughly by a factor of 1.5 at 200 Hz. This finding may have implications for the dynamic range of prosthetic stimuli and so could potentially be exploited by a retinal prosthesis to extend the dynamic range of perceived phosphene intensities.

5.4.2 Implications for retinal prostheses

The notion of 'optimal' in this study relates to a waveform that evokes a certain level of neural activity using minimal charge. In this study, RGCs are most receptive to cathodic-leading, asymmetric pulses of short phase duration, with a small amount of interphase interval.

It is likely that the electrical waveform employed by a commercially successful retinal prosthesis will depend on the site of intervention. Although the extent to which electrical stimulation can excite selective neuron populations (e.g. A2 cells) remains unclear, there is evidence that phase duration can be manipulated to elicit activity from different retinal neuron types.

Several groups (Jensen et al. 2005a; Fried et al. 2006; Tsai et al. 2009, isolated rabbit retina; Elfar et al. 2009, *in vivo* cat primary visual cortex) have found the electrically evoked retinal response to consist of a transient, short-latency component (attributed to direct RGC activation) as well as a late response originating from cellular activation presynaptic to the RGC (indirect activation). Fried et al. (2006) demonstrated that pulses of short duration could be used to selectively evoke short-latency spiking. Inner retinal neurons appear to be responsible for the late response and can be preferentially excited by longer phase durations (Fried et al., 2006; Margalit and Thoreson, 2006). It would be interesting to understand how the optimal waveform as defined by my study would differ for activation of bipolar or horizontal cells.

What kind of prosthetic vision will be evoked by electrical pulses of short phase duration? Short phase durations facilitate direct RGC stimulation, which can be made to replicate temporal patterns of activity observed in visually stimulated retina, supporting stimulus frequencies ranging from 50–250 Hz (Sekirnjak et al., 2006; Fried et al., 2006). Conversely, indirect spiking has been found to lack reliability during repetitive stimulation across a similar range of frequencies (Tsai et al., 2009). Sekirnjak et al. (2006) noted in their *in vitro* rat and guinea pig studies that short-latency spiking could be evoked in the absence of indirect activation for frequencies greater than 8 Hz, while Fried et al. (2006) found that indirect activation could be avoided entirely in the explanted rabbit retina. It has been suggested that direct retinal activation will afford high spatial selectivity (Wilms et al. 2003; Jensen et al. 2005a; Sekirnjak et al. 2006, 2009) but this is disputed. Elfar et al. (2009) determined the cortical activity associated with direct retinal activation in the cat to be broadly distributed and shifted towards the area centralis. Cortical activity

arising from indirect RGC activation was more focal and maintained higher correspondence with the retinotopic location of the electrical stimulus. Their study and others attribute the short-latency retinal response to the activation of incidental RGC axons positioned beneath the stimulating electrode, which is thought to limit the spatial resolution of a prospective retinal implant.

A factor that could influence the choice of waveform is the nature of degeneration in the patient. One supposed advantage of the subretinal and suprachoroidal modes of stimulation concerns the utilisation of surviving retinal circuitry for visual processing – the electrical activation of bipolar and horizontal cells over, or in addition to retinal ganglion cells is thought to lead to more precise phosphene generation (Weiland et al., 2005; Chader et al., 2009). Degenerative diseases such as retinitis pigmentosa are however characterised by extensive neural reorganization in addition to widespread neuronal death (Marc et al., 2003) and so it is likely that for severe cases of degeneration, the function of surviving interneurons will be compromised. This assertion is supported by findings from Margalit et al. (2011) who determined that synaptic responses from retinal interneurons were absent in late-stage degenerate mice and concluded that it may be more worthwhile to target retinal ganglion cells directly. Longer pulses are known to target retinal interneurons (Margalit and Thoreson, 2006) and so their use could be of benefit in early stages of disease where existing retinal circuitry retains its original function.

5.5 Conclusions

My study shows that waveform efficacy can be improved through manipulation of waveform parameters other than stimulus amplitude. For rectangular biphasic pulses, the largest gains in efficacy arise from the use of cathodic-leading pulses of short phase duration. Further performance improvements can be achieved by employing asymmetry and a small interphase interval. The present results suggest that a careful choice of waveform parameters could significantly improve the efficacy of a retinal prosthesis.

Chapter 6

Selective Sinusoidal Activation of RGCs

Modern retinal prostheses for the blind elicit visual perception through indiscriminate electrical stimulation of surviving neural populations. In the mammalian retina, the visual scene is encoded in the spike trains of 10–20 types of retinal ganglion cells, each of which responds differently to a visual stimulus. Indiscriminate activation of all these pathways by a retinal prosthetic would lead to the generation of misinformation, such as the simultaneous activation of ON and OFF pathways at the same retinal location. It is therefore of great interest to develop stimulation strategies that would selectively activate a subset of visual pathways. I directly injected sinusoidal currents into rat ganglion cells during whole cell current clamp recordings and demonstrated that certain RGC subsets, defined on the basis of morphological type, stratification, and size, were more responsive to high frequency stimulation. Frequency responses from ON and OFF cell recordings were compared with responses generated from single-compartment ON and OFF RGC models. Specifically, while OFF cells had the capacity to respond to higher frequencies (> 30 Hz) of intracellular stimulation, ON cells did not. Further simulations suggest this may be due to the presence of low-voltage-activated calcium (Ca^{2+}) channels expressed by OFF cells. It was also discovered that larger cells are better able to respond to high frequency intracellular stimulation. Given the intrinsic differences among ON and OFF cell responses to injected current, it may be possible to design extracellular stimulation strategies to activate selected visual pathways preferentially.

6.1 Introduction

The idea of using electrical current to confer visual information to the blind has received considerable global interest. Microelectronic visual prostheses target various stages of the visual system, with retinal prostheses seeking to restore vision to those suffering from degenerative eye diseases that compromise the photoreceptors of the retina. Clinical trials of retinal prostheses have demonstrated that while electrical stimulation of the retina does indeed elicit some sort of visual percept, these devices are as yet incapable of consistently evoking patterned neural activity resembling that observed in the healthy retina (Ahuja et al., 2011; Zrenner, 2002). Given that the retina uses up to 15 parallel pathways to encode different aspects of the visual scene (Wässle, 2004; Masland, 2001) and that existing modes of stimulation are largely non-specific, it is not perhaps surprising that visual percepts generated by current prosthetic devices are rather primitive. The ability to selectively activate particular cell types by means of careful electrical manipulation will allow for the induction of more natural neural activity and would constitute a significant advance over present stimulation strategies.

Retinal ganglion cells (RGCs) are tasked with the encoding of visual information into electrical signals that are relayed to the brain through the optic nerve. These cells constitute the output of the retina and take a variety of anatomical forms distinguished by soma size, dendritic field size, branching patterns, and stratification (Masland, 2001; Sun et al., 2002; Wässle, 2004). Together with the distribution of ion channels on the cellular membrane, these morphological characteristics give rise to intrinsic cellular properties that influence the nature and flow of visual information through the retinal network (O'Brien et al., 2002; Wong et al., 2012). For example, large cells, such as the alpha cells, have small input resistances and can thus be more easily activated by electrical stimuli.

Retinal ganglion cells (RGCs) vary not only in morphology but also in their response to light stimulation (for review, see Wässle 2004). The spiking frequency of an ON-centre cell (or simply ON cell) increases when its receptive field centre is exposed to light. Similarly, an OFF cell is excited by light decrements within the receptive field centre. ON-OFF cells respond to the change in contrast with both polarities. Each of these RGC types is further characterised by dendritic stratification – ON cell dendrites stratify within sublamina a of the inner plexiform layer, OFF cell dendrites stratify within sublamina b,

and ON-OFF cells dendrites occupy both sublaminae (Huxlin and Goodchild, 1997; Sun et al., 2002). Moreover, the distinct sets of circuitry underlying ON and OFF retinal pathways have a number of functional differences, including receptive field size, contrast adaptation, and contrast sensitivity (Chichilnisky and Kalmar, 2002; Zaghloul et al., 2003).

In the context of retinal prosthesis applications, it is of interest to see whether electrical stimulation can selectively elicit activation in a particular cell population. Recently it was shown that sinusoidal stimulation of the retina can preferentially activate different broad retinal cell classes. Using high frequency (100 Hz) stimulation, Freeman et al. (2010) were able to selectively activate RGCs. Lower frequencies were found to bias neural activation in bipolar cells (25 Hz) and photoreceptors (5 Hz). This finding appears to have considerable potential for the refinement of prosthetic stimulation. Additionally, modelled RGC responses to intracellular sinusoidal current injection predict that high frequency stimulation could bias OFF cell activation (Kameneva et al., 2010). In the present study I provide experimental validation of this prediction and further explore this frequency-selective activation of different RGC types.

Some of these data have been presented previously in a preliminary form (Hadjinicolaou et al., 2011).

6.2 Methods

6.2.1 Experiments

Retinal wholemount preparation

Whole-cell current clamp recordings from 82 RGCs were obtained using procedures described previously (O'Brien et al., 2002; Wong et al., 2012). Data were taken from 26 Long Evans rats aged between 6 and 11 months. Animals were anaesthetised with a mixture of Ketamine (100 mg/kg) and Xylazine (10 mg/kg) and enucleated, after which they were killed with an overdose of Sodium Pentobarbitone (350 mg intracardiac). Quadrants of retinal wholemounts were placed, ganglion cell layer up in the recording chamber (Warner Instruments, Hamden, CT USA, RC-26 GLP) and perfused (4–6 ml/min) with carbogenated Ames' medium (Sigma-Aldrich, St. Louis, MO) at room temperature. The chamber was mounted on the fixed stage of an upright microscope

(Olympus, BX51WI) utilizing a 40× water immersion lens. Tissue was visualised on a monitor with 4× additional magnification.

Physiological data collection and analysis

Before a whole-cell recording of a ganglion cell can be obtained, access to the cell surface must be obtained. This was achieved by making a small hole in the inner limiting membrane and optic fiber layer overlying the cell (O'Brien et al., 2002; Robinson and Chalupa, 1997; Taylor and Wässle, 1995; Wong et al., 2012). Recordings were limited to RGCs exposed during this procedure that had smooth surfaces and agranular cytoplasm. The pipette internal solution contained (in mM): K-gluconate 115, KCl 5, EGTA 5, HEPES 10, Na-ATP 2, Na-GTP 0.25; (mOsm = 273, pH = 7.3) including Alexa Hydrazide 488 (250 μM) and biocytin (0.5%).

Whole-cell current clamp recordings from RGCs were obtained with standard procedures (Hamill et al., 1981) using an intracellular amplifier (BA-1S, NPI). Initial pipette resistance was 3–7 MΩ. After measurement, this resistance was compensated using the bridge balance circuit of the amplifier. Resting potentials were corrected for the change in liquid junction potential that develops upon break-in and cell dialysis, measured directly as -5 mV (Neher, 1992). No capacitance compensation was employed to avoid inducing unwanted oscillations in the recording, which can lead to loss of the gigaohm seal.

The membrane potential was digitized with 16-bit precision at 20 kHz (USB-6221, National Instruments) and stored in digital form. The data were acquired using custom software developed in LabVIEW (National Instruments). Cells were excluded from analysis if they exhibited markedly inconsistent responses to stimuli, or if their morphological classification could not be reliably ascertained after performing the immunocytochemistry.

Electrical stimulation

Sinusoidal currents ranging in frequency from 1 to 60 Hz were injected through the recording pipette. The current amplitude was selected so as to compensate for the input resistance of each cell, which can vary over three orders of magnitude among different rat RGC types (Wong et al., 2012). Using a sinusoidal current of 10 Hz, the smallest amplitude was found such that at least one spike

was elicited from the cell in each stimulus cycle. This amplitude was then used to test all other frequencies. A single trial consisted of intracellular injection of the sinusoidal current of a given frequency for a period of 1s. The response of the cell was then quantified as the number of evoked spikes over this 1s period, and is labelled as *spiking frequency*. A single trial for each frequency was presented, and this was repeated to obtain at least two trials.

Immunocytochemistry and morphological identification

After recordings, the tissue was removed from the chamber, mounted onto filter paper, fixed for approximately 45 minutes in phosphate-buffered 4% paraformaldehyde, and stored for up to 2 weeks in 0.1 M phosphate-buffered saline (PBS; pH 7.4) at 4°C. Subsequent processing of the tissue revealed biocytin-filled cells by immersion in PBS with 0.5% Triton X-100 and 20 g/mL streptavidin conjugated to Alexa488 (Invitrogen) overnight. Tissue was thoroughly washed in PBS and stained with propidium iodide for roughly 8 minutes revealing the boundaries of the inner plexiform layer (IPL) by staining the nuclei of cells in the inner nuclear (INL) and ganglion cell layers (GCL). After additional washes in PBS, samples were mounted onto Superfrost slides and protected in 60% glycerol using a coverslip.

Ganglion cells were reconstructed in 3D with a confocal microscope (Zeiss PASCAL) and classified morphologically into types according to the criteria listed in the following papers (Sun et al., 2002; Huxlin and Goodchild, 1997; Wong et al., 2012). Cells were classified as either ON or OFF-center according to whether their dendrites were localised mainly within sublamina a (OFF $n = 22$) or sublamina b (ON $n = 5$) of the inner plexiform layer. Cells whose dendrites ramified in both strata (a and b) were classified as ON-OFF ($n = 14$).

6.2.2 Numerical simulations

The responses of ON and OFF RGCs were simulated using the formulations described by (Kameneva et al., 2011). Briefly, the dynamics of the ionic currents used to model ON and OFF cells were described using Hodgkin-Huxley

type equations:

$$C_m \frac{dV}{dT} = I_{\text{stim}} + \bar{g}_L(V - V_L) + \bar{g}_{\text{Na}} m^3 h(V - V_{\text{Na}}) + \bar{g}_{\text{Ca}} c^3 (V - V_{\text{Ca}}) + (\bar{g}_{\text{K}} n^4 + \bar{g}_{\text{K,A}} a^3 h_{\text{A}} + \bar{g}_{K(\text{Ca})})(V - V_{\text{K}}) + (\bar{g}_{\text{h}} l(V - V_{\text{h}}) + \bar{g}_{\text{T}} m_{\text{T}}^3 h_{\text{T}}(V - V_{\text{T}}) + \bar{g}_{\text{NaP}} p(V - V_{\text{Na}}), \quad (6.1)$$

where V is the membrane potential, $C_m = 1$ μF cm^{-2} represents the membrane capacitance, I_{stim} is an intracellular stimulation current, and $\bar{g}$ is the maximum conductance of an ionic current, specified by the subscript. The values for the parameters in (6.1) are given in the appendix. The model was implemented as a single-compartment model in NEURON (Hines, 1993) and solved using a standard Euler integration method with a time step of 0.025 ms. The constrained models of ON and OFF cells were used to examine the possibility of selective sinusoidal stimulation of each cell population. Simulations were used to systematically explore the frequency-amplitude parameter space and the associated cellular responses. Sinusoidal currents were tested over all frequencies while keeping the stimulus amplitude constant. The amplitude was made to vary between 10–100 pA and the stimulation frequency between 1–100 Hz.

6.2.3 Data analysis

All data analysis was performed using custom software developed in MATLAB (MathWorks). To explore the effect of cell morphology on spiking frequency, two subsets of cells (large and small) were identified on the basis of dendritic field and soma size. Cells with dendritic field diameters exceeding 410 μm were designated as large, while cells with dendritic field diameters less than 250 μm were designated as small. Further, cells were designated as small if their soma diameters were $\leq$ 14 μm, and large if their diameters were $\geq$ 20 μm. The statistical significance of any observed difference between spiking frequency for RGC subsets was evaluated with a random permutation test, as described in Chapter 5. Frequency response data from two cells were excluded on the basis of their responses being more than three standard deviations from the mean. The relationship between soma diameter and dendritic field diameter ($\rho = 0.484, p = 0.001$) was confirmed by computing Pearson's linear correlation coefficient.

6.3 Results

6.3.1 Anatomy

Recordings were made from 82 RGCs, for which data on morphological classification ($n = 40$), stratification ($n = 41$), soma diameter ($n = 42$), and dendritic field diameter ($n = 44$) was collected. It was not always possible to completely reconstruct the recorded cell's morphology. For example, while the morphological type of a given cell may be recovered, uneven retinal tissue may prevent classification on the basis of ON, OFF, or ON-OFF stratification. It is also possible to discern the stratification of a cell in cases where the soma was not adequately reconstructed, preventing morphological classification. Of the cells recorded, 42 cells could not be classified conclusively and were therefore omitted from the analysis presented here. The remaining cells were classified as A-type ($n = 15$), B-type ($n = 2$), C-type ($n = 11$), or D-type ($n = 12$) according to the classification scheme proposed by Sun et al. (2002). In general, cells classified as A-type had large somata and large dendritic fields, cells with small-to-medium-sized somata and dendritic fields were classified as B-type, and cells with small-to-medium-sized somata and medium-to-large dendritic fields were designated as C-type. Bistratified cells were assigned to the D-type class. On the basis of stratification, $n = 5$ were classified as ON cells, $n = 22$ as OFF cells, and $n = 14$ as ON-OFF cells. Dendrite stratification was calculated by the formula

$$strat_{\%}(x) = 100\left(1 - \frac{IPL_{start} - x}{IPL_{start} - IPL_{end}}\right),$$

where x refers to the depth (here, 'depth' increases from the ganglion cell layer towards the photoreceptor layer) of a terminal dendrite, and IPL_{start} and IPL_{end} refer to the start and beginning of the inner plexiform layer, respectively. Stratification distributions for ON and OFF cells are shown in figure 6.1. Examples of ON, ON-OFF and OFF cell reconstructions are shown in figure 6.2.

6.3.2 Physiology

In this section, the frequency responses of various RGC subsets (A, B, C, and D; ON and OFF; large and small) to sinusoidal current stimuli are compared.

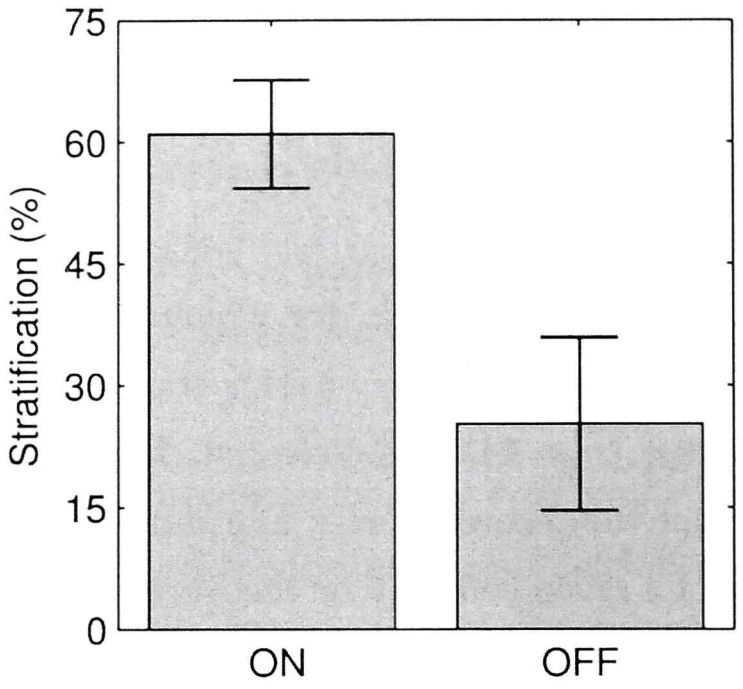

Figure 6.1. Stratification distributions for ON ($n = 5$) and OFF ($n = 21$) cells. Error bars indicate plus/minus one standard deviation.

Stimulus amplitudes were set so as to elicit at least one spike per sinusoidal phase when delivered at 10 Hz. In some cases, multiple spikes were evoked by each stimulus cycle, leading to a spiking frequency of greater than 10 Hz for the optimised amplitude.

Morphological cell types

Figure 6.3 (A) shows spike frequency plotted against stimulus frequency for four different morphological cell types. The A cells appear to have the highest upper cut-off frequencies when compared to those of other morphological types (fig. 6.3A). The average cutoff frequencies with respect to the spiking frequency at 10 Hz are estimated as 40 Hz (A-type), 11 Hz (B-type), 8 Hz (C-type), and 16 Hz (D-type). Though responses from A cells and B cells seem most different, the limited number of recordings from B cells ($n = 2$) make it difficult to draw any credible conclusions. On the other hand, frequency responses from C- and D-type cells are quite similar ($p > 0.05$ for all frequencies). The majority of monostratified cells were OFF-centre (14/15 A-type, 0/2 B-type, and 8/11 C-type). Figure 6.3 (B) compares the A-type and C-type frequency responses, while (C) compares A-type and D-type responses. It is clear that for these cell groupings, the error bars do not overlap at frequencies above 10 Hz, demonstrating a difference in frequency selectivity.

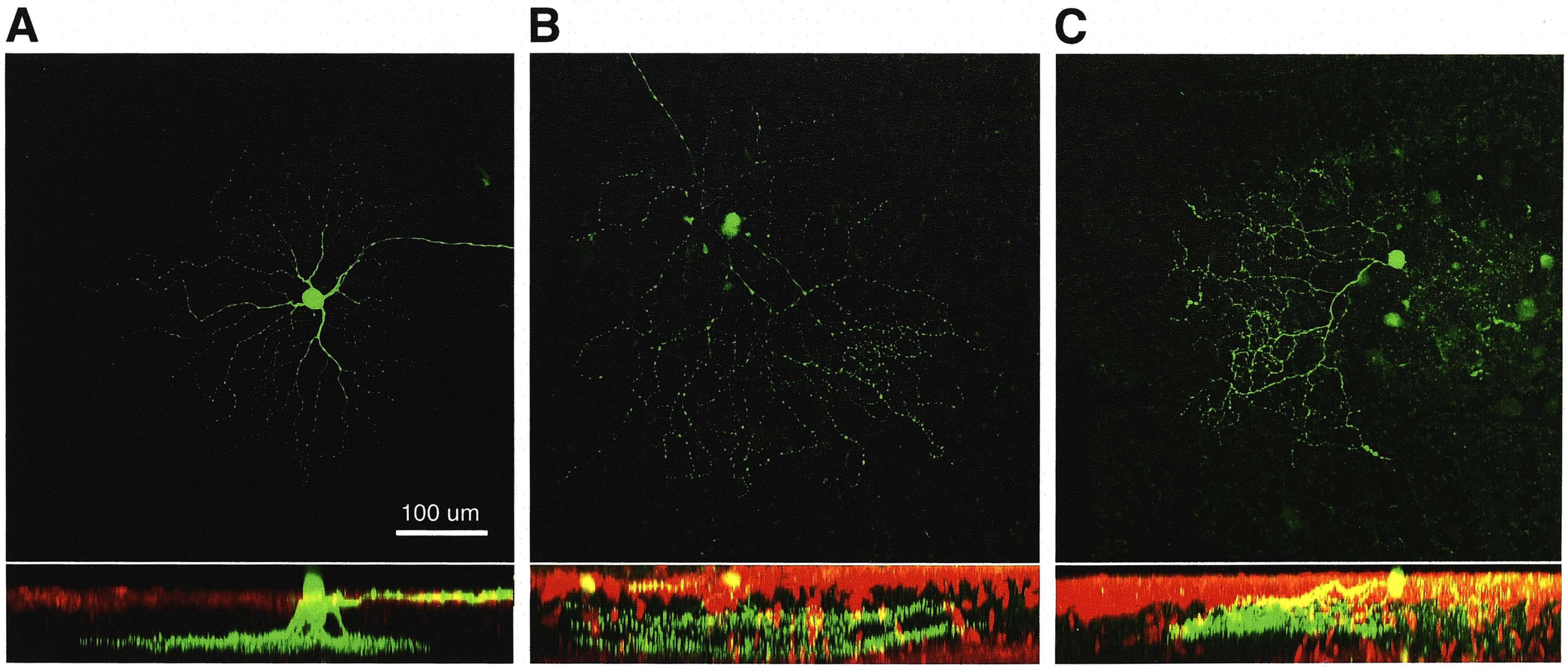

Figure 6.2. 3D reconstructions of OFF (A2o; panel A), ON-OFF (D2; panel B) and ON (C4i, panel C) cells. A cross-section of the retina (shown beneath each *en face* representation) illustrates where each cell stratifies within the inner plexiform layer (IPL). Recorded cells are labelled with Alexa488 (green). All other cells in the ganglion cell layer and IPL are labelled with propidium iodide (red).

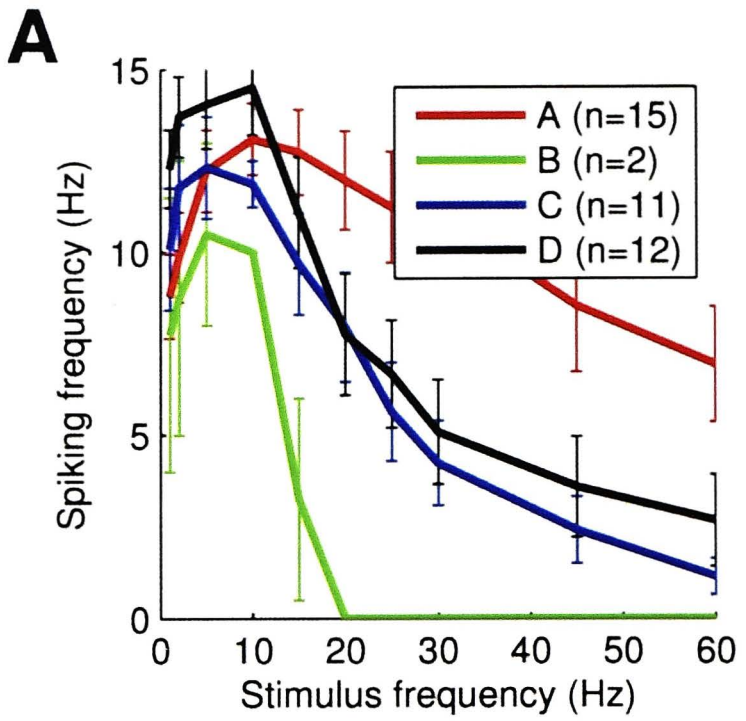

Figure 6.3. Spike rate as related to stimulus frequency for different morphological cell classes. (A) Frequency responses from A, B, C, and D cell classes. (B) A comparison of A-type (red) and C-type (blue) responses. (C) A comparison of A-type (red) and D-type (black) responses. Statistically significant differences between responses for a given frequency are denoted by grey ($p < 0.05$) and black ($p < 0.01$) dots. Error bars indicate plus/minus one standard error.

ON and OFF stratification

To investigate the reported difference between ON and OFF cells (Margolis and Detwiler, 2007; Kameneva et al., 2010), identified neurons were classified on the basis of their stratification, combining cells across all morphological classes. ON cells ($n = 5$) comprised 3 A-type, 1 B-type, and 1 C-type cell. OFF cells ($n = 22$) comprised $n = 14$ A-type and $n = 8$ C-type cells. While it would be ideal to compare ON versus OFF for each cell type individually, random cell selection prevented this from being a possibility in the present work. However, it should be considered that ON and OFF stimulation will activate all cell types simultaneously in the real retina, so the results presented here are relevant to general stimulation with a prosthetic device. The frequency responses of all identified ON, OFF, and ON-OFF RGCs, along with the responses to the 42 non-identified cells are shown in figure 6.4. In general, OFF cells are able to maintain their spiking rate when stimulated at the highest frequencies tested, while ON cell responses are suppressed beyond 30 Hz. Figure 6.5 shows the frequency tuning characteristics averaged across the identified ON, OFF, and ON-OFF cell types. The ON-OFF frequency response appears to be a hybrid of those of the ON and OFF cells – at lower frequencies, ON-OFF cells respond similarly to OFF cells, while at higher frequencies their suppressed response resembles that of the ON cells. Based on their intrinsic properties, it has been noted previously that the firing properties of ON and ON-OFF cells are more similar to one another than either are to OFF cells (Wong et al., 2012).

Large and small cells

In Chapter 5, it was revealed that small cells could better keep up with high frequency extracellular stimulation. This prompted further investigation as to whether a similar finding could be made for the intracellular stimulation employed in this chapter. Significant differences were observed between the frequency responses of large and small cell populations. Responses were collected from cells of all morphological types. Figure 6.6 (A, B) demonstrates that it is in fact the larger cells, both in terms of soma size and dendritic field size, that are better able to respond to intracellular sinusoidal stimulation than smaller cells. Histograms illustrating the distribution of large and small cells are shown in figure 6.6 (C, D).

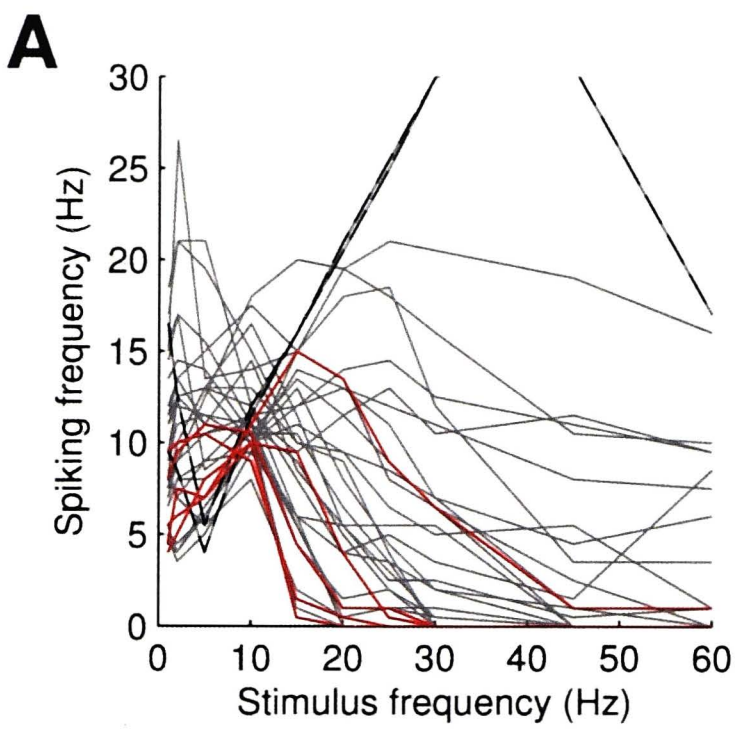

Figure 6.4. Spike rate as related to stimulus frequency for identified ON (A), OFF (B), and ON-OFF (C) cells. Responses from cells that were not fully identified using anatomical techniques ($n = 42$) are in grey. The two outliers excluded from further analysis are indicated in black.

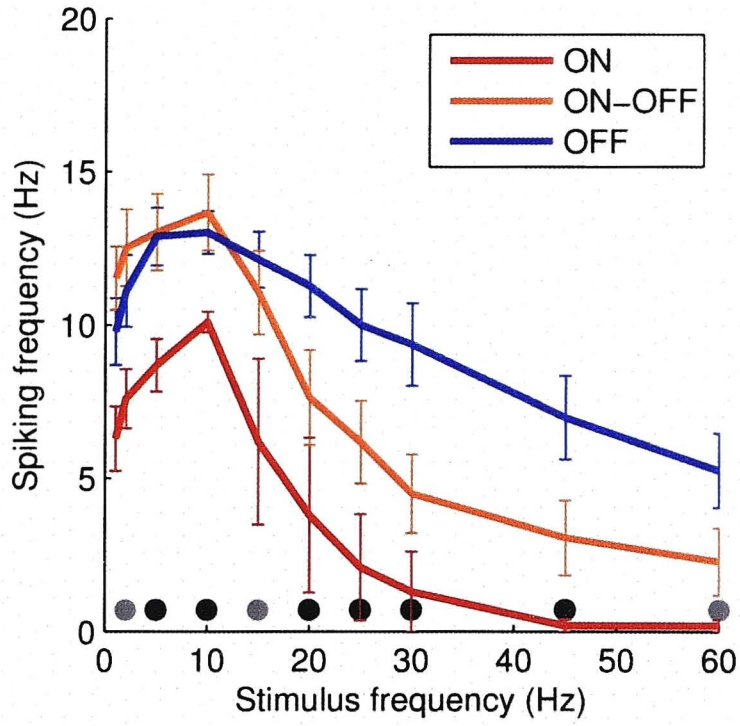

Figure 6.5. Spike rate as a function of stimulation frequency for ON, OFF, and ON-OFF cell recordings. Statistically significant differences between ON- and OFF-type responses for a given frequency are denoted by grey ($p < 0.05$) and black ($p < 0.01$) dots. Error bars indicate plus/minus one standard error.

6.3.3 Simulations

In this section, the responses of ON and OFF RGCs to sinusoidal current injection are compared to the simulated responses of the RGC model of Kameneva et al. (2010). Data from all confirmed ON and OFF cells are used, irrespective of morphological type and size.

Filter characteristics of ON and OFF cells

Figure 6.7 shows simulated responses (blue) to sinusoidal current injections at 10 Hz (left) and 30 Hz (right). For comparison, experimental recordings from representative ON and OFF cells are shown in black. The simulated responses exhibit many similarities to the observed experimental recordings. Notably, simulated ON and OFF cells exhibit differences in their response to higher frequency stimulation similar to those described for the ON and OFF cells recorded in my investigation. During 10 Hz stimulation, the simulated ON cell produced a single spike during each cycle of the stimulus current. The simulated OFF cell produced two action potentials on every cycle of the sinusoid. Similar observations were made in the experimental recordings (fig. 6.7, black traces) although the real OFF cell shown produces two spikes on only two cycles and more often producing only a single spike per cycle. While both ON and OFF cells shown here could sustain their responses to 10 Hz stimulation, only the OFF cell could keep up at 30 Hz. (fig. 6.7, right, black traces)

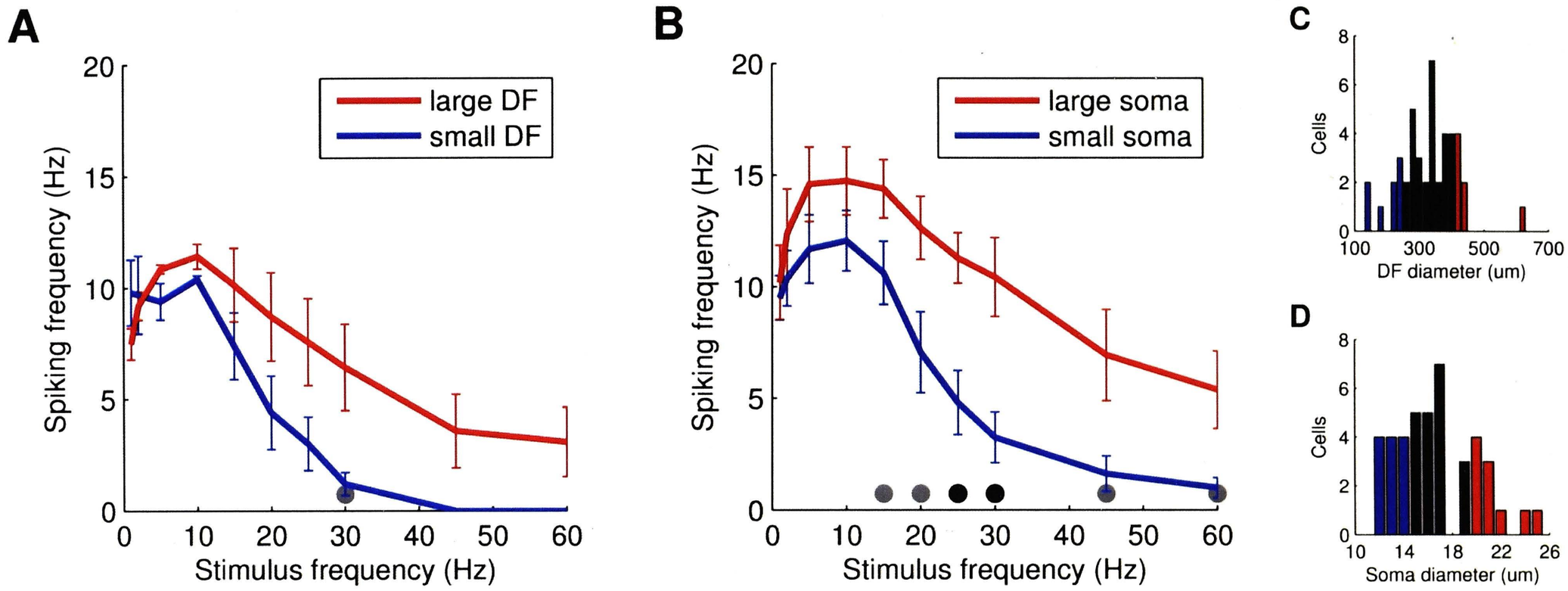

Figure 6.6. Spike rate as related to stimulus frequency for large and small cells. (A) Averaged responses from cells with large ($>$ 410 µm) and small ($<$ 250 µm) dendritic field diameters. (B) Averaged responses from cells with large ($\geq$ 20 µm) and small ($\leq$ 14 µm) soma diameters. Statistically significant differences between large and small responses for a given frequency are denoted by grey ($p < 0.05$) and black ($p < 0.01$) dots. (C, D) Dendritic field and soma diameter histograms, highlighting large (red) and small (blue) distributions. Error bars indicate plus/minus one standard deviation.

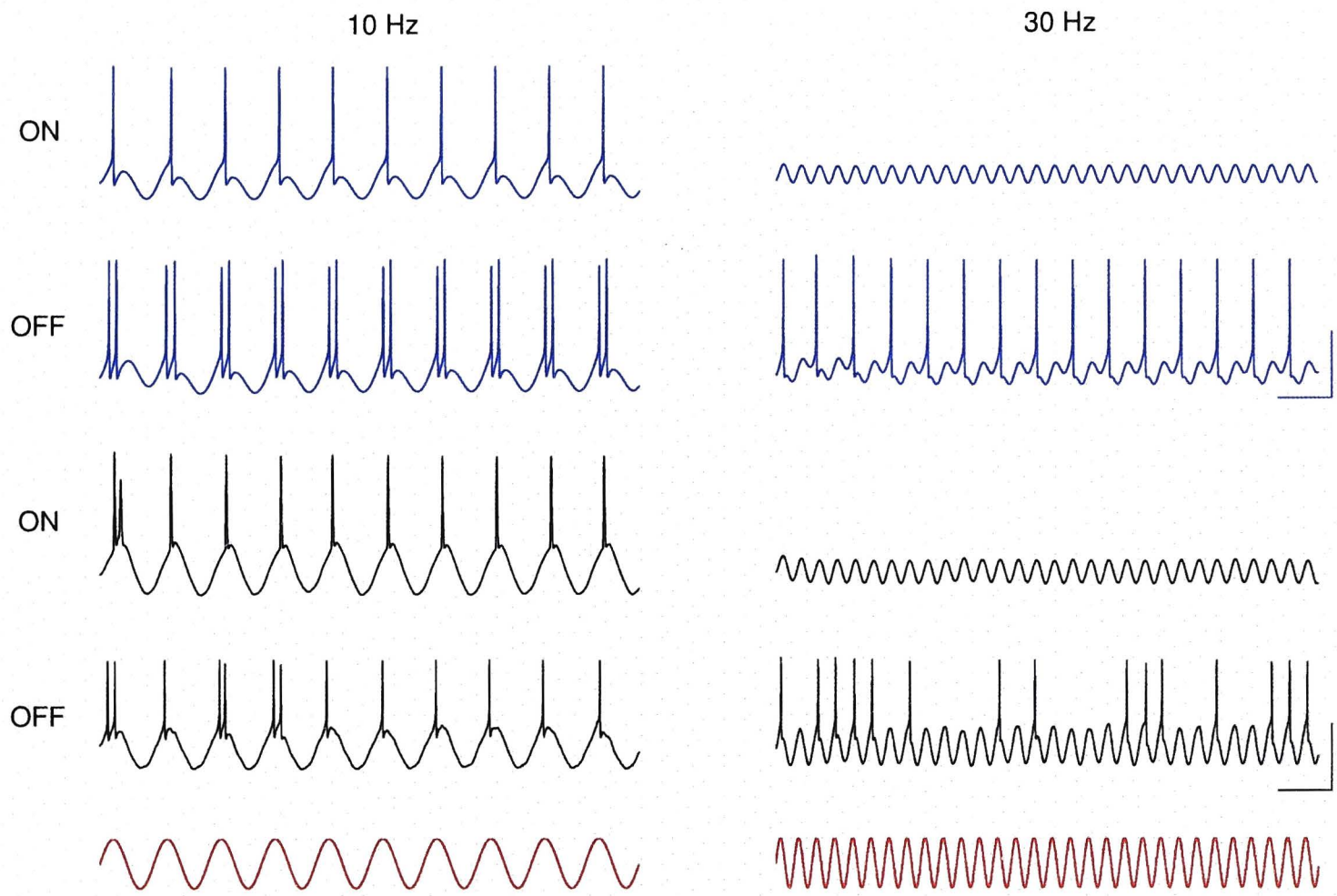

Figure 6.7. ON and OFF RGC responses to sinusoidal stimulation. Blue: simulated responses. Black: responses from experimental recordings. The stimulus amplitude was conserved across all frequencies. Stimulus cycles are provided at the bottom. Vertical bars: 50 mV, horizontal bars: 100 ms.

albeit firing only sporadically. The simulated ON cell failed to produce any spikes in response to stimulation at 30 Hz. The simulated OFF cell exhibited low amplitude fluctuations for every second cycle of the stimulus, producing a spike on every other cycle.

Spiking frequency is plotted as a function of stimulus frequency for the simulated ON and OFF cells in figure 6.8 (A). For comparison, the average spike frequency as a function of stimulus frequency for the recorded ON ($n = 5$) and OFF ($n = 22$) cells are shown in figure 6.8 (B) (these curves are reproduced from figure 6.5). The frequency response derived from the model cells predicts the general features of the responses observed experimentally. Both the simulated responses and the recorded data exhibit a low-pass characteristic with spiking frequency falling off as stimulus frequency is increased above the reference frequency of 10 Hz. Both the simulated OFF cell and the recorded OFF cells responded at all frequencies investigated (1–60 Hz) although the response from the simulated OFF cell appears much more robust (producing roughly two spikes within each cycle of the stimulus) than that typically observed in the data (where responses were more sporadic).

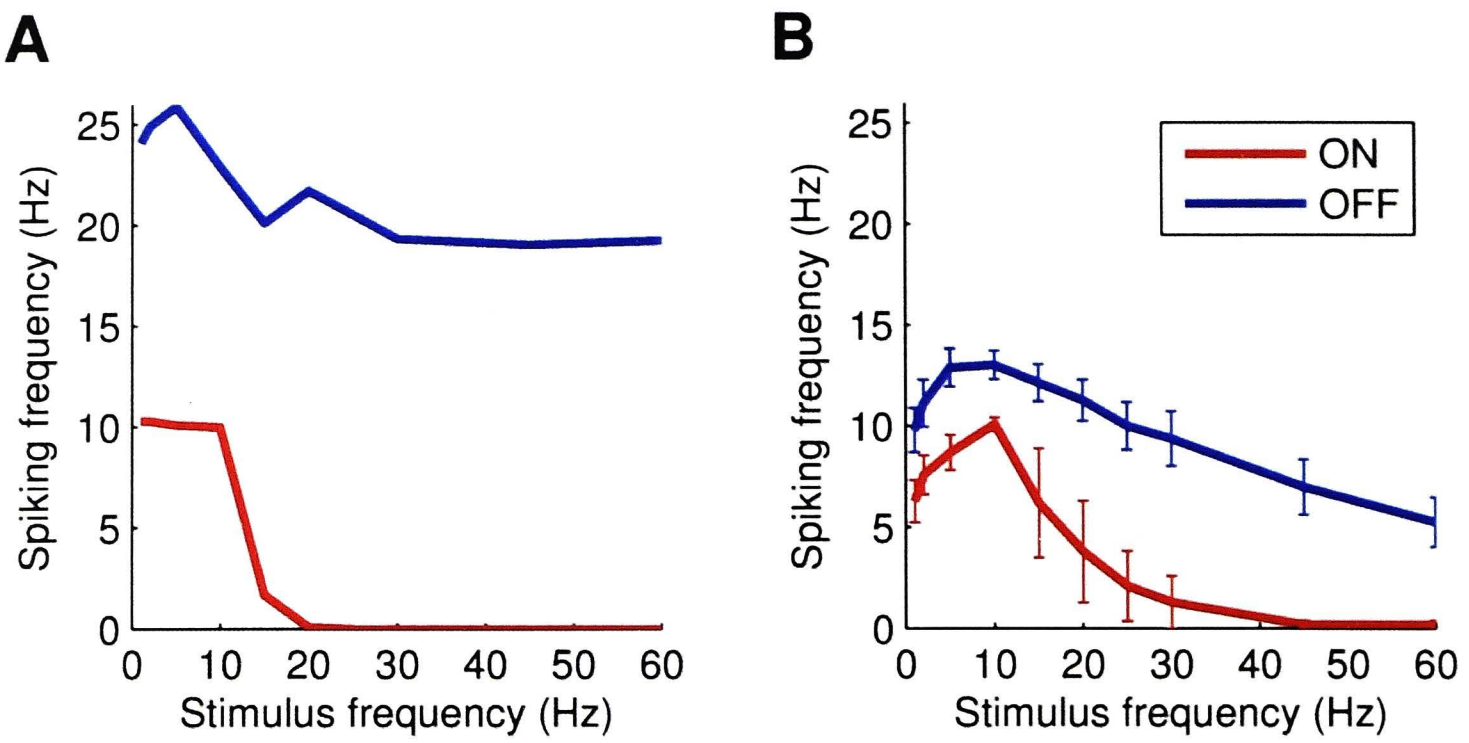

Figure 6.8. Spike rate as a function of stimulation frequency, for ON (red) and OFF (blue) cells. (A) Simulation results. (B) Experimental results, as in figure 5. Error bars indicate plus/minus one standard error.

Frequency-induced phase shift in spike timing

A closer look at the timing of action potentials within the sinusoidal stimulus cycle revealed a phase shift with frequency (fig. 6.9). Figure 6.9 (A) shows a histogram of ON cell spiking as a function of the sinusoidal phase at which the spike occurred, for experimental data. Figure 6.9 (B) contains simulated data corresponding to figure 6.9 (A). Action potentials from both ON and OFF RGCs were initiated during the early depolarizing phase of the sinusoid at low frequencies, shifting to the depolarizing peak with increasing frequency. The discrepancies observed between model and data are perhaps caused by the greater spike timing variability encountered during experiments, compared with that of simulations. This could be attributed to the variability in synaptic input delivered to the RGC by the rod bipolar pathway (Murphy and Rieke, 2006), which has not been accounted for in simulations.

Influence of Ca^{2+} and hyperpolarization-activated currents

One notable difference between ON and OFF cell physiology is the differential expression of low-voltage-activated (LVA) Ca^{2+} channels. LVA Ca^{2+} channels are expressed in OFF cells but not in ON cells (Margolis et al., 2010). Using the model OFF cell, I investigated the extent to which the observed differences in the frequency response of ON and OFF cells might be attributed to differences in LVA Ca^{2+} current. In the model OFF cell, LVA Ca^{2+} channels

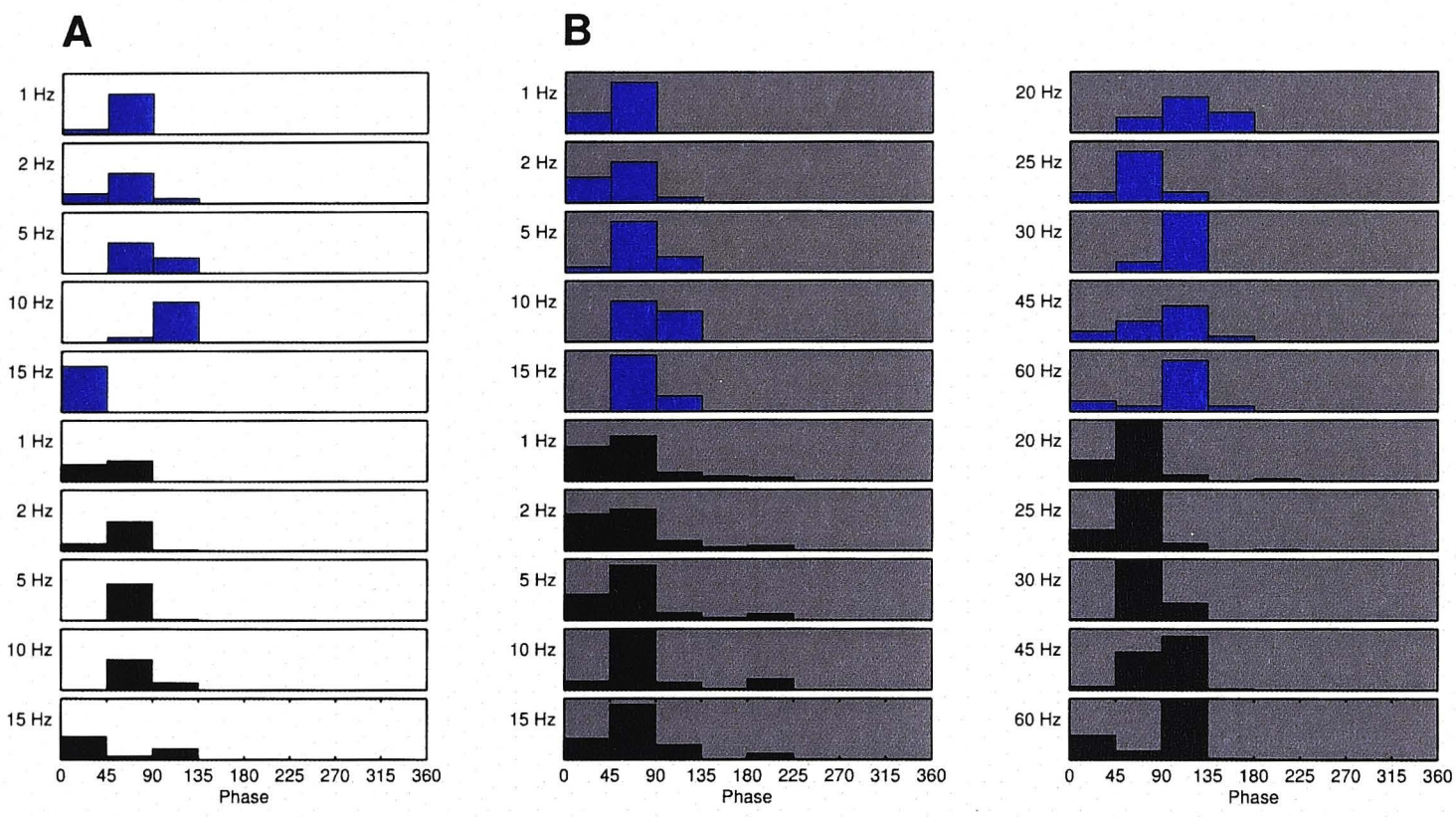

Figure 6.9. Phase shifts in spike timing with frequency. Blue: simulated results. Black: experimental data. (A) ON cell spike histograms are shown in the first column (white background) for 1-15 Hz stimuli. (B) OFF cell spike histograms are shown in the remaining two columns (grey background) for 1–15 Hz and 20–60 Hz stimuli. For experimental data, the maximum bin count is 50. For simulated data, the maximum bin count is 12.

are represented by the T-type calcium current i_{CaT}. This is a transient current, ceasing within 270 ms after initiation (Wang et al., 1991). Simulations of the OFF cell were conducted with and without the presence of the T-type calcium current. Figure 6.10 shows spiking frequency as a function of stimulus frequency for the model OFF cell with $\bar{g}_T = 4 \times 10^{-4}$ S/cm^2 (blue line) and for the same model with i_{CaT} removed ($\bar{g}_T = 0$ S/cm^2). In the absence of the T-type calcium current, the response of the model cell is completely suppressed for frequencies above ~15 Hz, demonstrating that the expression of LVA Ca^{2+} channels is a likely mechanism allowing OFF cells to follow higher frequencies of stimulation.

The differences between modelled ON and OFF responses can be examined in terms of the T-type LVA Ca^{2+} gating variables, m (representing the percentage of open channels) and h (the proportion of inactivated channels). The modelled T-type current takes the form

$$I_T = \bar{g}_T m_T^3 h_T (V - V_T).$$

Figure 6.11 shows the simulated ON (red trace) and OFF (blue trace) responses to 30 Hz sinusoidal stimulation. At time t_1, due to the positive sinusoidal phase of the injected stimulus, the membrane potential reaches the level

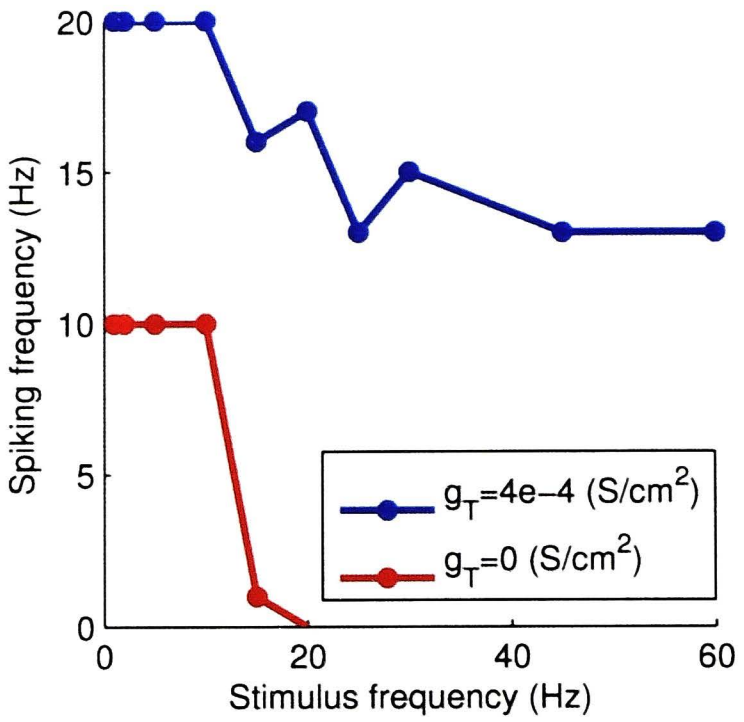

Figure 6.10. Spike rate as a function of stimulus frequency, with and without the presence of T-type currents.

at which T-type currents start to open (fig. 6.11, horizontal dashed line). This level is identical for both ON and OFF cells. The membrane potential continues to rise with the depolarizing phase of the stimulus, eventually reaching the threshold for LVA Ca^{2+} channel activation. Since these channels are only present in the OFF cell, its associated membrane potential continues to rise from time t_2 to t_3 due to the influx of Ca^{2+} ions. Meanwhile, the membrane potential of the ON cell starts to hyperpolarize in response to the negative-going phase of the injected sinusoid. The additional depolarizing influence of the T-type currents in the OFF cell keeps the membrane potential high enough such that the next cycle of the stimulus can drive the cell above threshold and elicit an action potential.

This disparity between ON and OFF cell responses persists for higher frequencies of stimulation. Figure 6.12 features the simulated responses of ON and OFF cells to sinusoidal stimulation of 200 Hz.

6.4 Discussion

Intracellular sinusoidal stimulation was found to preferentially activate certain retinal ganglion cell populations in this study. A-type cells, which are characterised by large somata and dendritic fields, were found to be more responsive to higher stimulus frequencies when compared with cells of other morphological classes. The recordings from B cells (smaller somata and dendritic fields), in spite of their paucity in the present data set, suggest that these cells are

the least responsive to high frequency stimulation. Further, cells of differing stratification were associated with differing frequency responses. OFF cells, regardless of cell type, were able to sustain activation over a broad range of stimulus frequencies, while ON cell spiking was very low for frequencies above 30 Hz. This work also reveals a differential frequency response between large and small RGC subsets. Large cells, both in terms of dendritic field size and soma size, were found to be more responsive to high frequency intracellular stimulation compared to small cells.

This last finding appears to conflict with the effect of morphology (i.e. size) described in Chapter 5 for extracellular biphasic stimuli. In that study, the small cells were better able to sustain activation at high stimulus frequencies. There are differences, however, that make comparison between the two modes of stimulation more equivocal. For the intracellular sinusoidal stimuli used in this chapter, the amount of charge injected per phase decreased with frequency. On the other hand, the per-phase charge was constant for the extracellular rectangular biphasic current pulses used in Chapter 5. An alternative intracellular stimulation protocol that would better compare with the extracellular protocol from Chapter 5 would keep the per-phase charge of a sinusoid constant by scaling the stimulus amplitude with frequency, for example. Cell type is another confounding factor. While the A2 cell class was the only class examined in Chapter 5, all cell types were under investigation in this study. As stimulation frequency increases, the likelihood of an injected pulse generating a spike becomes increasingly dependent on the input resistance R_{in} of the cell, an intrinsic cell property that varies between each cell class. Large cells (e.g. A-type), owing to their small input resistance, have small time constants $\tau = RC$, and so can be more easily driven by repetitive stimuli. Conversely, small cells (e.g. B-type) exhibit large input resistances and so are unable to sustain high frequency activation. The data in figure 6.3 validate these assertions, demonstrating that of the cell classes, A cells were the most responsive, and B cells were the least responsive to high frequency stimulation.

The experimental results of the present study were used to validate predictions made by single-compartment biophysical models of ON and OFF RGCs (Kameneva et al., 2010), the construction of which was based on previous reports of the ion channels present in these cells. Simulated ON RGCs were heavily suppressed by high stimulation frequencies ($\geq$15 Hz, versus $\geq$30 Hz for the ON cells recorded here), while simulated OFF cells were able to follow

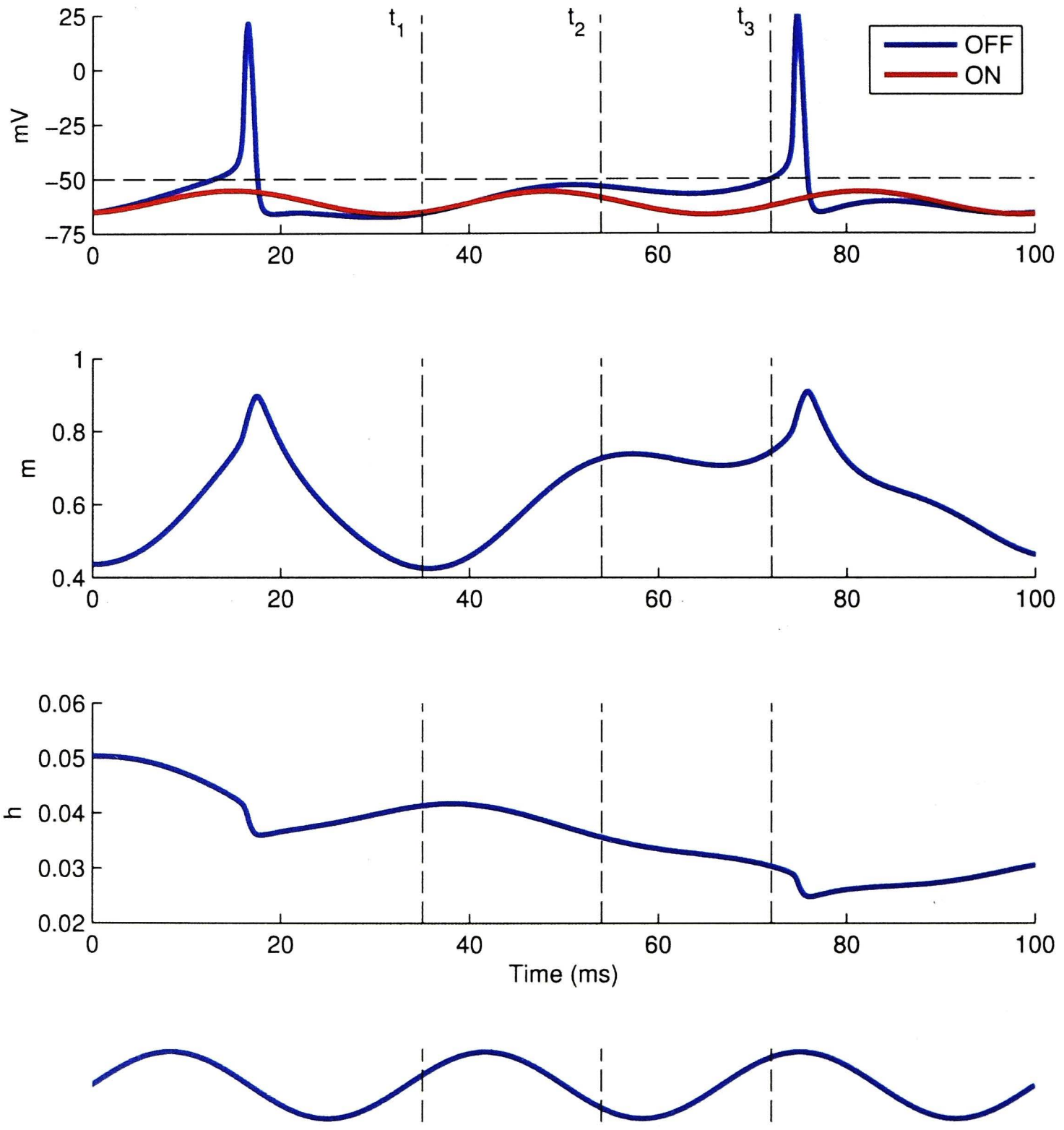

Figure 6.11. Simulated responses of ON (red) and OFF (blue) RGCs to 30 Hz sinusoidal stimulation, together with the modelled OFF cell LVA ion channel gating variables. The parameter m refers to the proportion of open T-type Ca^{2+} channels and the value h corresponds with the proportion of inactivated channels. A trace of the sinusoidal stimulation is shown below.

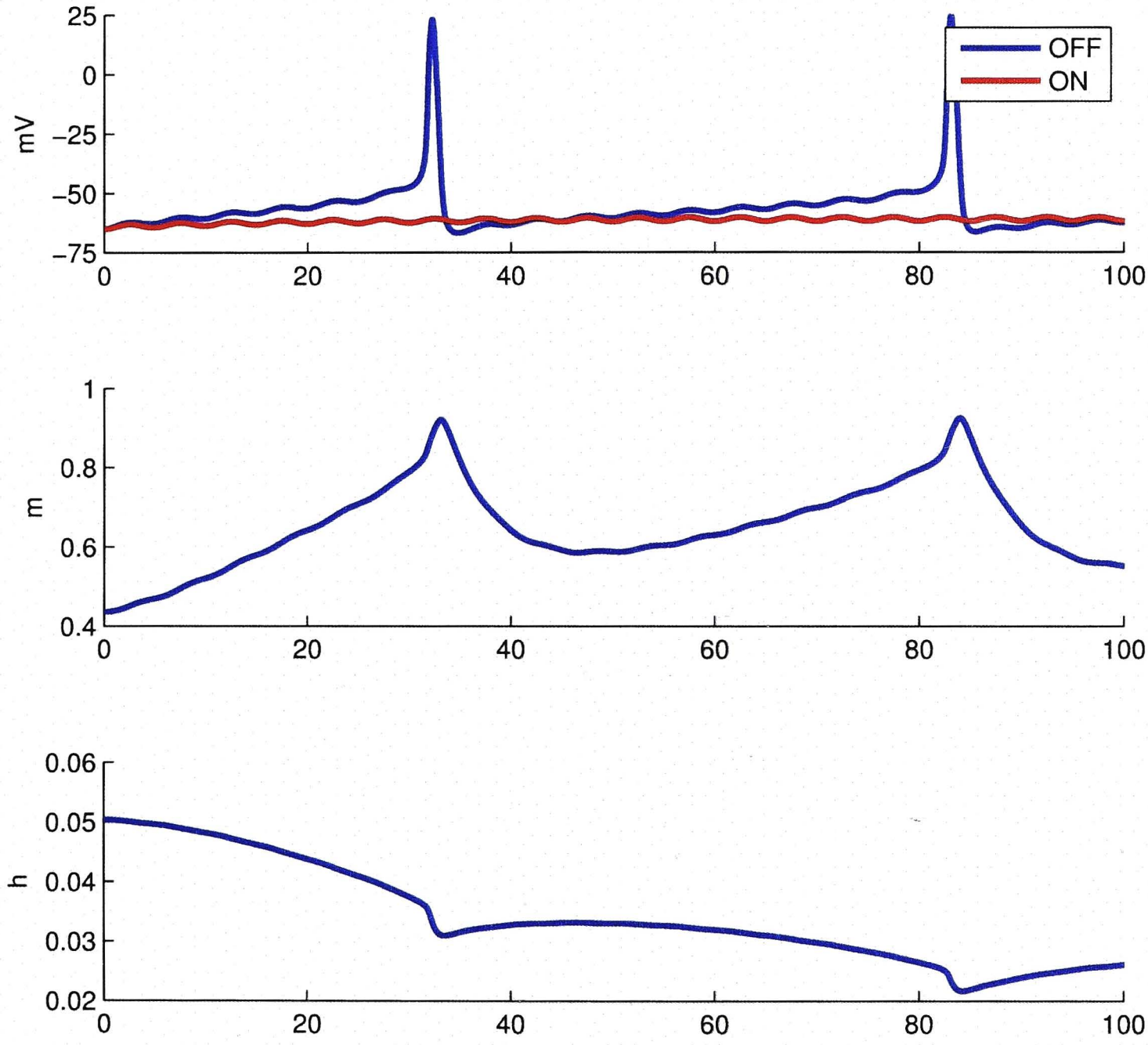

Figure 6.12. Simulated responses of ON (red) and OFF (blue) RGCs to 200 Hz sinusoidal stimulation, together with the modelled OFF cell LVA ion channel gating variables, as in figure 6.11.

stimulation frequencies of up to 60 Hz. The model predicted an increasing phase lag in the timing of action potentials with frequency, which was confirmed in the experimental data recorded here.

The modeling suggests that LVA Ca^{2+} current is largely responsible for the different band-pass characteristics observed between ON and OFF RGC responses to sinusoidal stimulation. At rest ($V_m = -65$ mV), the LVA Ca^{2+} channels, present only in OFF cells, are closed. In the case of sinusoidal stimuli, the hyperpolarizing phase serves to re-activate enough of these channels to enable rebound action potentials, which are triggered by the subsequent depolarizing phase. This process most likely occurs during a spike generated afterhyperpolarization (AHP). It is thought that the OFF cells use this rebound spiking mechanism to generate a precisely timed response to light offset (Margolis et al., 2010).

Differences between ON and OFF RGC responses to electrical stimulation, often with rectangular, biphasic, cathodic-first current stimuli, have been investigated previously (Sekirnjak et al., 2008; Jensen and Rizzo III, 2009; Cai et al., 2011). Jensen and Rizzo III (2009) reported that mouse ON RGCs were more sensitive to cathodic-first pulses than OFF cells. Electrical stimuli were delivered using a single platinum wire electrode. On the other hand, Sekirnjak et al. (2008) did not report a statistically significant difference between ON and OFF parasol cell activation thresholds using multielectrode arrays in the macaque. At present, there is a distinct lack of information regarding different RGC types and their responses to electrical stimulation at high frequency. One *in vitro* study of the rabbit retina found that with a high enough stimulating amplitude, brisk-transient cells were able to sustain pulse trains irrespective of the tested frequency, generating one spike per pulse for stimulation rates as high as 600 Hz (Cai et al., 2011). Conversely, most other cell types investigated in this study were unable to follow pulse trains at 300 Hz stimulation. Yang et al. (2011) investigated rabbit RGC responses to subretinal stimulation. Interestingly, they reported that ON cells responded to a greater range of frequencies, with the OFF cells effectively silenced by stimulation frequencies greater than 16 Hz.

The idea of selectively activating RGCs by means of sinusoidal electrical stimulation is not yet well explored. Freeman et al. (2010) studied the responses of rabbit retinal neurons to extracellular sinusoidal stimulation and found that RGCs were most sensitive to high frequency (100 Hz) stimulation, with bipolar

cells and photoreceptors preferentially activated by stimulation at 25 Hz and 5 Hz, respectively. The authors discovered that RGC axonal activation could be avoided by using lower frequency stimuli. Robinson and Chalupa (1997) used intracellular sinusoidal current injections to characterise the intrinsic properties of cat alpha and beta RGCs. These cells, although not classified by stratification, were found to have roughly the same ability in keeping up with repetitive stimulation, maintaining at least one spike per stimulus cycle for frequencies up to 10 Hz. In their study, the amplitude was adjusted so as to achieve the same hyperpolarization across all frequencies, in contrast to the present work where amplitude was fixed for all frequencies, allowing for investigation of the cells filtering characteristics.

Although our data suggests that sinusoidal stimulation can preferentially activate ON or OFF pathways, it is unlikely that such a waveform can be safely used at low frequency without modification in a retinal prosthesis. A standard 10 Hz sinusoid, for instance, is effectively a symmetric, biphasic pulse of 50 ms phase duration, the use of which would rapidly lead to electrode degradation (Rose and Robblee, 1990). High frequency (>100 Hz) sinusoids, on the other hand, have an effective phase duration on the order of microseconds. It may be possible to take advantage of the differential expression of LVA Ca^{2+} channels to preferentially stimulate the OFF pathway at such frequencies. On the other hand, a low frequency waveform may be ideal for conveying focal information. A stimulating electrode will likely activate, in addition to nearby RGC somata, passing axons whose associated neurons supply input to a different cortical area (Elfar et al., 2009). It follows that in order to achieve focal activation of the retina, activation of fibres distant to the stimulating electrode should be minimised. In their study of the isolated rabbit retina, Freeman et al. (2010) found that low frequency (10 Hz and 25 Hz) sinusoidal stimuli could excite a cell without exciting nearby axons, when the stimulating electrode was adjacent to the soma. A sinusoidal stimulus used for this purpose might, for example, employ a smaller amplitude to compensate for the large per-phase charge associated with a waveform of this type.

These results are based on the responses of RGCs in normal retina. Will similar results hold in the degenerate retina? It has been shown that RGC morphology and physiology is inherently stable during photoreceptor degeneration and that many functional characteristics (e.g. balance of excitatory and inhibitory synaptic input, intrinsic firing properties, dendritic Ca^{2+} signalling) observed

in the wild-type mouse are preserved in rd mice (Margolis et al., 2008). Conversely, retinal degeneration has been associated with marked variations in spontaneous activity and has been shown to affect certain cell types differently, with preferential preservation of OFF cell responses in the rd mouse (Stasheff, 2008). The presense of this elevated spontaneous activity is further complicated by rhythmic 'waves' of spiking (Stasheff, 2008; Margolis et al., 2008). Further, the preservation of ON and OFF pathways will likely also depend on the type of degeneration. Stasheff et al. (2011) found that RGC light responses had been eliminated by P28 in the rd1 retina, while those of the rd10 retina persisted well beyond this age, expiring after P60. It remains to be seen how the degenerate retina will respond to sinusoidal stimulation, and I intend to pursue this line of work in future studies.

6.5 Conclusions

The present results show that it is possible to preferentially activate certain RGC subsets using higher stimulation frequencies, and that frequency modulation may be useful in retinal prosthetic devices as a means of eliciting selective activation of certain RGC populations that are differentiated by either morphology, stratification, or size. Simulations have also shown that the difference in frequency response between ON and OFF cells could potentially be caused by the expression of LVA Ca^{2+} channels in OFF but not ON RGCs. These findings could have important implications for the development of new stimulation strategies for visual prostheses.

Chapter 7

Summary

In the first chapter, I established the merit of using the rat A2 ganglion cell as an object of study in my research. Over the course of the second chapter, I discussed the concept of prosthetic vision, together with several issues that remain problematic in current retinal prosthesis initiatives. I have sought to address the issue of selective electrical stimulation through work in chapters 5 and 6. Chapter 4 demonstrates the electrochemical viability of using nitrogen-doped ultra-nanocrystalline diamond as a material for delivering electrical stimuli to evoke a biological response.

In this chapter I briefly summarise the key findings from chapters 4, 5, and 6 and outline a number of potential directions for future research.

Stimulating with N-UNCD

Chapter 4 explored the feasibility of using N-UNCD electrodes to elicit neuronal activation for prosthesis applications. Electrodes fabricated from N-UNCD possessed high electrochemical stability and biocompatibility, and were resistant to morphological and electrochemical changes over long-term continuous pulsing at charge injection limits. These electrodes exhibited a higher charge injection capacity than that of platinum (though significantly lower than that of iridium oxide) and were able to electrically activate RGCs while remaining well within the electrochemical limits of the material. It is also possible, using the fabrication techniques described in Chapter 4, to manipulate the diamond material to suit a variety of applications. The device being developed as part of the Bionic Vision Australia initiative will utilize these electrodes in the form of 100×100 μm square pads. The smaller dimensions

should allow for more precise patterns of electrical stimulation, which is expected to increase the maximum spatial resolution of the prospective retinal prosthesis.

Optimal electrical activation of RGCs

Work in Chapter 5 investigated how the parameters of an electrical waveform could be adjusted to increase efficacy, while preserving the injected per-phase charge. Recordings were made exclusively from rat A2 retinal ganglion cells. The waveform under consideration was a rectangular biphasic pulse, the same type of waveform employed by the current generation epiretinal implant of the Bionic Vision Australia retinal prosthesis initiative (Bionic Vision Australia, 2013). Accordingly, efficacy is defined as the proportion of stimuli that successfully evoked a biological response from the target RGC.

RGCs invariably favored a cathodic-first pulse of short first-phase duration, with a small interphase interval. First-phase duration and polarity were found to have the largest effects on activation thresholds. Results from the preliminary parameter survey demonstrated that on average, a 480 µs-per-phase pulse required 19 nC more charge per phase to reach activation threshold, in comparison to a 60 µs-per-phase pulse. A cathodic-first pulse required 11 nC less injected per-phase charge to reach activation threshold, relative to an anodic-first pulse. The median per-phase charge of the baseline waveform prior to optimisation (cathodic-first, symmetric, 120 µs per phase, no interphase interval) was 21 nC.

Every retinal ganglion cell investigated appeared to prefer one of three different electrical waveforms, as described in Chapter 5. The majority of RGCs (>60%) were most sensitive to a highly asymmetric waveform, with phase duration ratio PDR = pd_2/pd_1 = 480/60 = 8. A smaller proportion (17%) was most responsive to a symmetric waveform (PDR = 1). The remaining cells (22%) were responsive to pulses of short first-phase duration, regardless of asymmetry.

All RGCs became desensitised to repetitive electrical stimulation. The likelihood of an injected pulse evoking an action potential appeared to converge to a specific level by the thirtieth pulse, and this level fell with frequency. While a link between cellular morphology and waveform preference was not observed, cells with smaller somas and dendritic fields were better able to sustain electrical stimulation at high frequency.

The review of Merrill et al. (2005) summarises several commonly used rectangular, biphasic waveforms in electrophysiology, as well as their relative efficacy. The authors note that cathodic-first, asymmetric waveforms and those which utilise nonzero interphase intervals are more effective than cathodic-first, symmetric pulses, which in turn are more effective than anodic-first, symmetric pulses. My results are congruent with these findings. When compared to other waveforms in this review, the optimal electrical waveform as defined by my study is thought to be relatively efficacious and is not associated with high levels of electrode corrosion.

My study was limited to a single RGC type, the rat A2 cell. This alpha-like cell has been identified in every mammalian species investigated (Wässle and Boycott, 1991; Peichl, 1991) and its morphological homologue in the human is the parasol ganglion cell (Huxlin and Goodchild, 1997; Sun et al., 2002), which is primarily responsible for encoding transient, low-resolution motion signals (e.g. Schiller and Logothetis, 1990). To achieve a high level of spatial acuity, retinal prostheses will likely need to target the midget ganglion cell population of the human retina. It remains an open question as to how the optimal stimulus waveform might differ for different RGC types such as midget cells. However, one significant hurdle to addressing this question is that the midget homologue has not yet been identified in any other model species.

Selective sinusoidal activation of RGCs

In Chapter 6, intracellular sinusoidal current injections were used to reveal significant differences in how certain RGC subsets responded to high frequency stimulation. Here, I demonstrate that high frequency stimulation can bias neural activation in the A cell population over all other cell types. B cells appear to be the least responsive, failing to respond to frequencies much above 20 Hz. Cells differentiated by stratification also expressed differential frequency responses. OFF cells were able to sustain repetitive activation over all tested frequencies, while ON cell responses were heavily suppressed for stimulation frequencies of more than 30 Hz. Recordings from ON-OFF RGCs were used to demonstrate that the frequency response of these cells appears to be a hybrid of the ON and OFF responses. As was discovered in Chapter 5, large and small cells differed in their responsiveness to repetitive stimulation, though for these intracellular stimuli, the larger cells were better able to sustain high frequency activation.

Hodgkin-Huxley models of ON and OFF RGCs were used to simulate frequency responses of each cell type, and these were compared with ON and OFF RGC recordings. The general features of the experimentally observed responses agreed with those of simulated responses. Additional simulations suggest that the observed difference between ON and OFF cells may be attributed to the expresson of low-voltage-activated Ca^{2+} currents in OFF but not ON RGCs.

7.1 Implications for retinal prostheses

In Chapter 5, I discovered that smaller cells were better able to keep up with high frequency stimulation. Quigley (1998) found that larger cells were more susceptible to degeneration in his study of glaucoma. If this is also a characteristic of degeneration in the case of retinitis pigmentosa, my finding may appear encouraging. Even within the single cell type considered in this investigation, there is considerable variation in the ability of a cell to sustain repetitive stimulation at high frequency, which is strongly correlated to the size of the cell. If this is a general property that applies to all RGCs irrespective of cell type, then it stands to reason that smaller cells, which are more likely to transmit fine spatial detail, will be better equipped to follow repetitive prosthetic stimulation.

If short pulses result in direct RGC activation and direct activation is caused by electrical stimulation of local fibres, then short, cathodic pulses such as those found in my study may in fact be selective for fibres rather than cell bodies. McIntyre and Grill (2000) employ stimuli of relatively short phase duration (200 µs) in their computational study and predicted that a cathodic stimulus activating 70% of passing fibres will also activate 10% of local cells. An otherwise equivalent anodic stimulus activating 70% of local cells also activated 25% of fibres. Indirect activation may offer better spatial resolution largely because the targeted bipolar cells do not have lateral axons. If this is true, the electrical waveform employed in a commercially successful retinal prosthesis will likely require additional charge to preferentially stimulate cell bodies and so may not be optimal in terms of charge minimisation.

Freeman et al. (2010) use extracellular sinusoidal stimulation to preferentially activate different cell types in the isolated rabbit retina. RGCs were best activated by high frequency (100 Hz) stimulation. The authors also found

that while low frequency (10 Hz and 25 Hz) stimuli could be used to excite the cell when the stimulating electrode was in close proximity to the soma, spiking could not be initiated from the axon, even for the largest tested amplitudes. A retinal prosthesis working to deliver fine spatial detail could potentially avoid the quandary of axonal activation by delivering short pulses at low frequencies. Conversely, rapid, non-focal visual information such as motion detection might best be conveyed using high frequency stimulation of the periphery.

My intracellular study in Chapter 6 is the first that compares the electrical responses of RGCs on the basis of morphology. This is important because, as detailed in the first chapter, anatomically distinct cell types encode particular aspects of visual processing. An *in vitro* stimulation strategy that elicits activation in selective neural populations would facilitate characterisation of the bioelectrical interactions that result from prosthetic stimulation, thereby allowing for the development of a more informed stimulation strategy in the implant, and hopefully, the evocation of more meaningful prosthetic vision.

7.2 Future work

There are several ways in which the work in Chapter 5 can be extended. One option would be to repeat the optimization procedure for another cell type, ideally one whose properties mirror that of the midget ganglion cell. Should the optimal waveform for this cell be substantially different to that of the A2 cell (and notionally by extension, the parasol cell), it may be useful for a retinal prosthesis to employ both waveforms to recreate different components of the visual scene – the optimal parasol waveform for peripheral vision and the optimal midget waveform for central vision, for example. If these waveforms cannot preferentially stimulate the midget or parasol pathways, it may yet be possible to find waveforms that bias neural activation in the ON or OFF pathways.

The optimal waveform may also depend on the effects of retinal degeneration, particularly in advanced stages of disease where retinal circuitry can be significantly altered in both structure and function. Synaptic inputs were not controlled for in my study, and so the extent to which the retinal network influenced RGC waveform preference is unknown. Accordingly, it may be worth blocking synaptic input to examine the effect on the optimal waveform. Depending on the site of stimulation, it could potentially be of value to consider

the optimal waveform for another retinal neuron class. In the case of a subretinal or suprachoroidal implant, finding the optimal waveform for the bipolar or amacrine cell may be of greater merit.

With advances in retinal prosthesis development, the capacity of present-day stimulators to deliver more complicated electrical waveforms (that differ from the "tried-and-true" subset) should eventually become widespread. It is clear that the use of rectangular, biphasic pulses represents the primary constraint of my study, and so consideration of other waveform types such as sinusoids and Gaussian functions constitutes a natural extension to this work. A simple idea would be to replace each phase of the optimal waveform with a sinusoidal half-phase of equivalent charge and to see how this influences efficacy.

Appendix A

Simulation Parameters

Table A.1. Simulation parameters for equation (6.1) in Chapter 6.

Parameter	**Value**
R	8.314 J/(M·K)
F	9.684×10^4
$[Ca^{2+}]_e$	1.8 mM
$[Ca^{2+}]_i(t)$	$\frac{d[Ca^{2+}]_i(t)}{dt} = \frac{-3I_{Ca}(t)}{2FR} - \frac{[Ca^{2+}]_i(t)-[Ca^{2+}]_{res}}{\tau_{Ca}}$
$[Ca^{2+}]_{diss}$	10^{-6} M
$[Ca^{2+}]_{res}$	0.1 µM
τ_{Ca}	1.5 ms
T	22°C
C_m	1 µF/cm^2
V_{Na}	35 mV
V_{K}	-70 mV
V_{L}	-60 mV
V_{h}	0 mV
V_{T}	120 mV
$V_{\mathrm{Ca}}(t)$	$\frac{RT}{2F}\ln\left(\frac{[Ca^{2+}]_e}{[Ca^{2+}]_i(t)}\right)$
$\bar{g}_{\mathrm{Na}}$	4×10^{-2} S/cm^2
$\bar{g}_{\mathrm{K}}$	1.2×10^{-2} S/cm^2
$\bar{g}_{\mathrm{K,A}}$	3.6×10^{-2} S/cm^2
$\bar{g}_{\mathrm{Ca}}$	2×10^{-3} S/cm^2
$\bar{g}_{\mathrm{L}}$	5×10^{-5} S/cm^2
$\bar{g}_{\mathrm{K(Ca)}}(t)$	$2 \times 10^{-3} \cdot \frac{([Ca^{2+}]_i(t)/[Ca^{2+}]_{diss})^2}{1+([Ca^{2+}]_i(t)/[Ca^{2+}]_{diss})^2}$
$\bar{g}_{\mathrm{h}}$	$0 \leq \bar{g}_{\mathrm{h}} \leq 1 \times 10^{-5}$ S/cm^2 (ON RGCs)
	$2 \times 10^{-6} \leq \bar{g}_{\mathrm{h}} \leq 1 \times 10^{-4}$ (OFF RGCs)
$\bar{g}_{\mathrm{T}}$	0 S/cm^2 (ON RGCs)
	$4 \times 10^{-4} \leq \bar{g}_{\mathrm{T}} \leq 12 \times 10^{-4}$ S/cm^2 (OFF RGCs)
$\bar{g}_{\mathrm{NaP}}$	$0 \leq \bar{g}_{\mathrm{NaP}} \leq 1 \times 10^{-5}$ S/cm^2 (ON RGCs)
	5×10^{-8} S/cm^2 (OFF RGCs)

Variables $m, h, c, n, a, h_A, l, m_T, p$ in 6.1 reflect the opening and closing of voltage-gated ion channels and satisfy the following:

$$\frac{dx}{dt} = -(\alpha_x + \beta_x)x + \alpha x,$$

where x is the gating variable. The rate of change h_T has the following second-order dynamics:

$$\dot{h}_T = \alpha_{h_T}(1 - h_T - d) - \beta_{h_T} h_T,$$

where d satisfies

$$\dot{d} = \beta_d(1 - h_T - d) - \alpha_d d.$$

Table A.2. Rate constants for voltage-gated ion channels. Voltage is in units of millivolts.

Parameter	α	β
Na^+ channel	$\alpha_m = \frac{-0.6(V+30)}{e^{-0.1(V+30)}-1}$	$\beta_m = 20e^{-(V+55)/18}$
	$\alpha_h = 0.4e^{-(V+50)/20}$	$\beta h = \frac{6}{1+e^{-0.1(V+20)}}$
Ca^{2+} channel	$\alpha_c = \frac{-0.3(V+13)}{e^{-0.1(V+13)}-1}$	$\beta c = 10e^{-(V+38)/18}$
K^+ channel	$\alpha_n = \frac{-0.02(V+40)}{e^{-0.1(V+40)}-1}$	$\beta_n = 0.4e^{-(V+50)/80}$
A channel	$\alpha_a = \frac{-0.006(V+90)}{e^{-0.1(V+90)}-1}$	$\beta_a = 0.1e^{-(V+30)/10}$
	$\alpha_{h_A} = 0.04e^{-(V+70)/20}$	$\beta_{h_A} = \frac{0.6}{1+e^{-0.1(V+40)}}$
h channel	$\alpha_l = e^{0.08316(V+75)}$	$\beta_l = e^{0.033264(V+75)}$
T channel	$\alpha_{m_T} = (1.7 + e^{-(V+28.8)/13.5})^{-1}$	$\beta_{m_T} = \frac{1+e^{-(V+63)/7.8)}}{1.7+e^{-(V+28.8)/13.5}}$
	$\alpha_{h_T} = e^{-(V+160.3)/17.8}$	$\beta_{h_T} = \alpha_{h_T}((0.25 + e^{(V+83.5)/6.3})^{0.5} - 0.5)$
	$\alpha_d = \frac{1+e^{(V+37.4)/30}}{240(0.5+(0.25+e^{(V+83.5)/6.3})^{0.5})}$	$\beta_d = \alpha_d(0.25 + e^{(V+83.5)/6.3})^{0.5}$
NaP channel		
$[V < -40]$	$\alpha_p = \frac{0.025+0.14e^{(V+40)/10}}{1+e^{-(V+48)/10}}$	$\beta_p = \frac{1-(1+e^{-(V+48)/10})^{-1}}{0.025+0.14e^{(V+40)/10}}$
$[V \geq -40]$	$\alpha_p = \frac{0.02+0.145e^{(V+40)/10}}{1+e^{-(V+48)/10}}$	$\beta_p = \frac{1-(1+e^{-(V+48)/10})^{-1}}{0.02+0.145e^{(V+40)/10}}$

Bibliography

Ahuja, A. K., Behrend, M. R., Kuroda, M., Humayun, M. S., and Weiland, J. D. (2008). An in vitro model of a retinal prosthesis. *IEEE Transactions on Biomedical Engineering*, 55:1744–1753.

Ahuja, A. K., Dorn, J. D., Caspi, A., McMahon, M. J., Dagnelie, G., Dacruz, L., Stanga, P., Humayun, M. S., and Greenberg, R. J. (2011). Blind subjects implanted with the Argus II retinal prosthesis are able to improve performance in a spatial-motor task. *British Journal of Ophthalmology*, 95: 539–543.

Armstrong, C. M. and Hille, B. (1998). Voltage-gated ion channels and electrical excitability. *Neuron*, 20:371–380.

Aspenberg, P., Anttila, A., Konttinen, Y. T., Lappalainen, R., Goodman, S. B., Nordsletten, L., and Santavirta, S. (1996). Benign response to particles of diamond and SiC: bone chamber studies of new joing replacement coating materials in rabbits. *Biomaterials*, 17:807–812.

Basser, P. J. and Roth, B. J. (2000). New currents in electrical stimulation of excitable tissues. *Annual Review of Biomedical Engineering*, 2:377–397.

Bear, M. F., Connors, B. W., and Paradiso, M. A. *Neuroscience: exploring the brain (3rd edition)*, chapter Chapter 4 – The action potential, page 86. Lippincott Williams & Wilkins, (2006).

Behrend, M. R., Ahuja, A. K., Humayun, M. S., Chow, R. H., and Weiland, J. D. (2012). Resolution of the epiretinal prosthesis is not limited by electrode size. *IEEE Transactions on Neural Systems and Rehabilitation Engineering*, 19:436–442.

Benardete, E. A, Kaplan, E., and Knight, B. W. (1992). Contrast gain control in the primate retina: P cells are not X-like, some M cells are. *Visual Neuroscience*, 8:483–486.

Bergonzo, P., Bongrain, A., Scorsone, E., Bendali, A., Rousseau, L., Lissorgues, G., Mailley, P., Li, Y., Kauffmann, T., Goy, F., Yvert, B., Sahel, J. A., and Picaud, S. (2011). 3D shaped mechanically flexible diamond microelectrode arrays for eye implant applications: the MEDINAS project. *IRBM*, 32:91–94.

Besch, D., Sachs, H., Szurman, P., Gülicher, D., Wilke, R., Reinert, S., Zrenner, E., Bartz-Schmidt, K. U., and Gekeler, F. (2008). Extraocular surgery for implantation of an active subretinal visual prosthesis with external connections: feasibility and outcome in seven patients. *British Journal of Ophthalmology*, 92:1361–1368.

Bi, A., Cui, J., Ma, Y., Olshevskaya, E., Pu, M., Dizhoor, A. M., and Pan, Z. (2006). Ectopic expression of a microbial-type rhodopsin restores visual responses in mice with photoreceptor degeneration. *Neuron*, 50:23–33.

Bionic Vision Australia. The bionic eye, (2013). URL `http://bionicvision.org.au/eye`.

Boycott, B. B. and Wässle, H. (1974). The morphological types of ganglion cells of the domestic cat's retina. *The Journal of Physiology*, 240:397–419.

Boycott, B. B. and Wässle, H. (1991). Morphological classification of bipolar cells of the primate retina. *European Journal of Neuroscience*, 3:1069–1088.

Brelén, M. E., Duret, F., Gérard, B., Delbeke, J., and Veraart, C. (2005). Creating a meaningful visual perception in blind volunteers by optic nerve stimulation. *Journal of Neural Engineering*, 2:S22–S28.

Brindley, G. S. and Lewin, W. S. (1968). The sensations produced by electrical stimulation of the visual cortex. *The Journal of Physiology*, 196:479–493.

Buch, P. K., Bainbridge, J. W., and Ali, R. R. (2008). AAV-mediated gene therapy for retinal disorders: from mouse to man. *Gene Therapy*, 15:849–857.

Butterwick, A., Vankov, A., Huie, P., Freyvert, Y., and Palanker, D. (2007). Tissue damage by pulsed electrical stimulation. *IEEE Transactions on Biomedical Engineering*, 54:2261–2267.

Cai, C. S., Ren, Q. S., Desai, N. J., Rizzo III, J. F., and Fried, S. I. (2011). Response variability to high rates of electrical stimulation in retinal ganglion cells. *Journal of Neurophysiology*, 106:153–162.

Chader, G. J., Weiland, J. D., and Humayun, M. S. (2009). Artificial vision: needs, functioning, and testing of a retinal prosthesis. *Progress in Brain Research*, 175:317–332.

Chalupa, L. M. and Günhan, E. (2004). Development of ON and OFF retinal pathways and retinogeniculate projections. *Progress in Retinal and Eye Research*, 23:31–51.

Chan, L. H., Ray, A., Thomas, B. B., Humayun, M. S., and Weiland, J. D. In vivo study of response threshold in retinal degenerate model at different degenerate stages. In *IEEE Engineering in Medicine and Biology Society Conference Proceedings*, (2008).

Chan, T. L., Martin, P. R., Clunas, N., and Grünert, U. (2001). Bipolar cell diversity in the primate retina: morphologic and immunocytochemical analysis of a new world monkey, the marmoset callithrix jacchus. *The Journal of Comparative Neurology*, 437:219–239.

Chen, S., Mahadevappa, M., Roizenblatt, R., Weiland, J. D., and Humayun, M. S. (2006). Neural responses elicited by electrical stimulation of the retina. *Transactions of the American Ophthalmological Society*, 104:252–259.

Chichilnisky, E. J. and Kalmar, R. S. (2002). Functional asymmetries in ON and OFF ganglion cells of primate retina. *The Journal of Neuroscience*, 22: 2737–2747.

Cho, A. K., Sampath, A. P., and Weiland, J. D. (2011). Physiological response of mouse retinal ganglion cells to electrical stimulation: effect of soma size. *Conference Proceedings of the IEEE Engineering in Medicine and Biology Society*, 2011:1081–1084.

Cho, A. K., Sampath, A. P., and Weiland, J. D. (2012). Physiological response of normal and rd mouse retinal ganglion cells to electrical stimulation. *Conference Proceedings of the IEEE Engineering in Medicine and Biology Society*, 2012:2985–2988.

Cleland, B. G., Dubin, M. W., and Levick, W. R. (1971). Sustained and transient neurones in the cat's retina and lateral geniculate nucleus. *The Journal of Physiology*, 217:473–496.

Cleland, B. G. and Levick, W. R. (1974). Brisk and sluggish concentrically organized ganglion cells in the cat's retina. *The Journal of Physiology*, 240: 421–456.

Cogan, S. F. (2008). Neural stimulation and recording electrodes. *Annual Review of Biomedical Engineering*, 10:275–309.

Cogan, S. F., Guzelian, A. A., Agnew, W. F., Yuen, T. G. H., and McCreery, D. B. (2004). Over-pulsing degrades activated iridium oxide films used for intracortical neural stimulation. *Journal of Neuroscience Methods*, 137: 141–150.

Colodetti, L., Weiland, J. D., Colodetti, S., Ray, A., Seiler, M. J., and Hinton, D. R. (2007). Pathology of damaging electrical stimulation in the retina. *Experimental Eye Research*, 85:23–33.

Crook, J. D., Peterson, B. B., Packer, O. S., Robinson, F. R., Troy, J. B., and Dacey, D. M. (2008). Y-cell receptive field and collicular projection of parasol ganglion cells in macaque monkey retina. *The Journal of Neuroscience*, 28:11277–11291.

Curcio, C. A. and Allen, K. A. (1990). Topography of ganglion cells in human retina. *The Journal of Comparative Neurology*, 300:5–25.

Curcio, C. A., Sloan, K. R., Kalina, R. E., and Hendrickson, A. E. (1990). Human photoreceptor topography. *The Journal of Comparative Neurology*, 292:497–523.

Dacey, D. M. (1993). The mosaic of midget ganglion cells in the human retina. *The Journal of Neuroscience*, 13:5334–5355.

Dacey, D. M. Origins of perception: retinal ganglion cell diversity and the creation of parallel visual pathways. In *The cognitive neurosciences*, pages 281–301. The MIT Press, (2004).

Dacey, D. M. and Petersen, M. R. (1992). Dendritic field size and morphology of midget and parasol ganglion cells of the human retinas. *Proceedings of the National Academy of Sciences*, 89:9666–9670.

Daiger, S. P., Bowne, S. J., and Sullivan, L. S. (2007). Perspective on genes and mutations causing retinitis pigmentosa. *Archives of Ophthalmology*, 125: 151–158.

de Balthasar, C., Patel, S., Roy, A., Freda, R., Greenwald, S., Horsager, A., Mahadevappa, M., Yanai, D., McMahon, M. J., Humayun, M. S., Greenberg, R. J., Weiland, J. D., and Fine, I. (2008). Factors affecting perceptual thresholds in epiretinal prostheses. *Investigative Ophthalmology and Visual Science*, 49:2303–2314.

Delbeke, J., Pins, D., Michaux, G., Wanet-Defalque, M., Parrini, S., and Veraart, C. (2001). Electrical stimulation of anterior visual pathways in retinitis pigmentosa. *Investigative Ophthalmology & Visual Science*, 42:291–297.

Dowling, J. E. (2005). Artificial human vision. *Expert Review of Medical Devices*, 2:73–85.

Dryja, T. P., McGee, T. L., Reichel, E., Hahn, L. B., Cowley, G. S., Yandell, D. W., Sandberg, M. A., and Berson, E. L. (1990). A point mutation of the rhodopsin gene in one form of retinitis pigmentosa. *Nature*, 343:364–366.

Durand, D. M. *Biomedical engineering fundamentals*, chapter 28: Electrical stimulation of excitable systems, pages 28–1–28–21. CRC Press, (2006).

Efron, B. and Tibshirani, R. J. *An introduction to the bootstrap*. Chapman and Hall, (1993).

Elfar, S. D., Cottaris, N. P., Iezzi, R., and Abrams, G. W. (2009). A cortical (V1) neurophysiological recording model for assessing the efficacy of retinal visual prostheses. *Journal of Neuroscience Methods*, 180:195–207.

Enroth-Cugell, C. and Robson, J. G. (1966). The contrast sensitivity of retinal ganglion cells of the cat. *The Journal of Physiology*, 187:517–552.

Fariss, R. N., Li, Z., and Milam, A. H. (2000). Abnormalities in rod photoreceptors, amacrine cells, and horizontal cells in human retinas with retinitis pigmentosa. *American Journal of Ophthalmology*, 129:215–223.

Field, G. D., Gauthier, J. L., Sher, A., Greschner, M., Machado, T. A., Jepson, L. H., Shlens, J., Gunning, D. E., Mathieson, K., Dabrowski, W., Paninski, L., Litke, A. M., and Chichilnisky, E. J. (2010). Functional connectivity in the retina at the resolution of photoreceptors. *Nature*, 467:673–678.

Field, G. D., Sher, A., Gauthier, J. L., Greschner, M., Shlens, J., Litke, A. M., and Chichilnisky, E. J. (2007). Spatial properties and functional organization of small bistratified ganglion cells in primate retina. *The Journal of Neuroscience*, 27:13261–13272.

Fite, K. V., Janušonis, S., Foote, W., and Bengston, L. (1999). Retinal afferents to the dorsal raphe nucleus in rats and mongolian gerbils. *The Journal of Comparative Neurology*, 414:469–484.

Freeman, D. K., Eddington, D. K., Rizzo III, J. F., and Fried, S. I. (2010). Selective activation of neuronal targets with sinusoidal electric stimulation. *Journal of Neurophysiology*, 104:2778–2791.

Freeman, D. K. and Fried, S. I. (2011). Multiple components of ganglion cell desensitization in response to prosthetic stimulation. *Journal of Neural Engineering*, 8:016008.

Freeman, D. K., Rizzo III, J. F., and Fried, S. I. (2011). Encoding visual information in retinal ganglion cells with prosthetic stimulation. *Journal of Neural Engineering*, 8:035005.

Fried, S. I., Hsueh, H. A., and Werblin, F. S. (2006). A method for generating precise temporal patterns of retinal spiking using prosthetic stimulation. *Journal of Neurophysiology*, 95:970–978.

Fried, S. I., Lasker, A. C. W., Desai, N. J., Eddington, D. K., and Rizzo III, J. F. (2009). Axonal sodium-channel bands shape the response to electrical stimulation in retinal ganglion cells. *Journal of Neurophysiology*, 101:1972–1987.

Fukuda, Y. (1977). A three-group classification of rat retinal ganglion cells: histological and physiological studies. *Brain Research*, 119:327–344.

Ganesan, K., Stacey, A., Meffin, H., Lichter, S., Greferath, U., Fletcher, E. L., and Prawer, S. Diamond penetrating electrode array for epi-retinal prosthesis. In *Engineering in Medicine and Biology Society, 2010 Annual International Conference of the IEEE*, (2010).

Garrett, D. J., Ganesan, K., Stacey, A., Fox, K., Meffin, H., and Prawer, S. (2011). Ultra-nanocrystalline diamond electrodes: optimization towards neural stimulation applications. *Journal of Neural Engineering*, 9:016002.

Garrido, J. A., Nowy, S., Hartl, A., and Stutzmann, M. (2008). The diamond/aqueous electrolyte interface: an impedance investigation. *Langmuir*, 24:3897–3904.

Gerding, H., Benner, F. P., and Taneri, S. (2007). Experimental implantation of epiretinal retina implants (EPI-RET) with an IOL-type receiver unit. *Journal of Neural Engineering*, 4:S38–S49.

Gosalia, K., Weiland, J. D., Humayun, M. S., and Lazzi, G. (2004). Thermal elevation in the human eye and head due to the operation of a retinal prosthesis. *IEEE Transactions on Biomedical Engineering*, 51:1469–1477.

Gothe, J., Brandt, S. A., Irlbacher, K., Röricht, S., Sabel, B. A., and Meyer, B. (2002). Changes in visual cortex excitability in blind subjects as demonstrated by transcranial magnetic stimulation. *Brain*, 125:479–490.

Gunst, R. F. and Mason, R. L. (2009). Fractional factorial design. *WIREs Computational Statistics*, 1:234–244.

Güven, D., Weiland, J. D., Fujii, G. Y., Mech, B. V., Mahadevappa, M., Greenberg, R. J., Roizenblatt, R., Qiu, G., LaBree, L., Wang, X., Hinton, D. R., and Humayun, M. S. (2005). Long-term stimulation by active epiretinal implants in normal and RCD1 dogs. *Journal of Neural Engineering*, 2: S65–S73.

Hadjinicolaou, A. E., Kameneva, T., Wong, R. C. S., Grayden, S. L., Cloherty, S. L., Ibbotson, M. R., Burkitt, A. N., Meffin, H., and O'Brien, B. J. Sinusoidal stimulation of retinal ganglion cells: computational model and experimental results. In *Proceedings of the Australian Neuroscience Society Conference*, (2011).

Hadjinicolaou, A. E., Leung, R. T., Garrett, D. J., Ganesan, K., Fox, K., Nayagam, D. A. X., Shivdasani, M. N., Meffin, H., Ibbotson, M. R., Prawer, S., and O'Brien, B. J. (2012). Electrical stimulation of retinal ganglion cells with diamond and the development of an all-diamond retinal prosthesis. *Biomaterials*, 33:5812–5820.

Hafezi, F., Grimm, C., Simmen, B., Wenzel, A., and Reme, C. (2000). Molecular ophthalmology: an update on animal models for retinal degenerations and dystrophies. *British Journal of Ophthalmology*, 84:922–927.

Hamill, O. P., Marty, A., Neher, E., Sakmann, B., and Sigworth, F. J. (1981). Improved patch-clamp techniques for high-resolution current recording from cells and cell-free membrane patches. *Pflügers Archiv*, 391:85–100.

Hartline, H. K. (1938). The response of single optic nerve fibres of the vertebrate eye to illumination of the retina. *American Journal of Physiology*, 121:400–415.

Hayes, K. C., Carey, R. E., and Schmidt, S. Y. (1975). Retinal degeneration associated with taurine deficiency in the cat. *Science*, 188:949–951.

Heine, W. F. and Passaglia, C. L. (2011). Spatial receptive field properties of rat retinal ganglion cells. *Visual Neuroscience*, 28:403–417.

Heynen, H. and van Norren, D. (1985). Origin of the electroretinogram in the intact macaque eye–II. *Vision Research*, 25:709–715.

Hines, M. NEURON – a program for simulation of nerve equations, (1993).

Hodgkin, A. L. and Huxley, A. F. (1952). A quantitative description of membrane current and its application to conduction and excitation in nerve. *The Journal of Physiology*, 117:500–544.

Humayun, M. S., de Juan Jr, E., Dagnelie, G., Greenberg, R. J., Propst, R. H., and Phillips, H. (1996). Visual perception elicited by electrical stimulation of retina in blind humans. *Archives of Ophthalmology*, 114:40–46.

Humayun, M. S., Weiland, J. D., Fujii, G. Y., Greenberg, R. J., Williamson, R., Little, J., Mech, B. V., Cimmarusti, V., Van Boemel, G., Dagnelie, G., and de Juan Jr, E. (2003). Visual perception in a blind subject with a chronic microelectronic retinal prosthesis. *Vision Research*, 43:2573–2581.

Huxlin, K. R. and Goodchild, A. K. (1997). Retinal ganglion cells in the albino rat: revised morphological classification. *The Journal of Comparative Neurology*, 385:309–323.

Jensen, R. J. and Rizzo III, J. F. (2006). Thresholds for activation of rabbit retinal ganglion cells with a subretinal electrode. *Experimental Eye Research*, 83:367–373.

Jensen, R. J. and Rizzo III, J. F. (2007). Responses of ganglion cells to repetitive electrical stimulation of the retina. *Journal of Neural Engineering*, 4:S1–S6.

Jensen, R. J. and Rizzo III, J. F. (2009). Activation of ganglion cells in wild-type and rd1 mouse retinas with monophasic and biphasic current pulses. *Journal of Neural Engineering*, 6:035004.

Jensen, R. J., Rizzo III, J. F., Ziv, O. R., Grünert, U., and Wyatt, J. (2003). Thresholds for activation of rabbit retinal ganglion cells with an ultrafine, extracellular microelectrode. *Investigative Ophthalmology & Visual Science*, 44:3533–3543.

Jensen, R. J., Ziv, O. R., and Rizzo III, J. F. (2005)a. Responses of rabbit retinal ganglion cells to electrical stimulation with an epiretinal electrode. *Journal of Neural Engineering*, 2:S16–S21.

Jensen, R. J., Ziv, O. R., and Rizzo III, J. F. (2005)b. Thresholds for activation of rabbit retinal ganglion cells with relatively large, extracellular microelectrodes. *Investigative Ophthalmology & Visual Science*, 46:1486–1496.

Jones, B. W., Kondo, M., Terasaki, H., Lin, Y., McCall, M., and Marc, R. E. (2012). Retinal remodeling. *Japanese Journal of Ophthalmology*, 56:289–306.

Joucla, S., Branchereau, P., Cattaert, D., and Yvert, B. (2012). Extracellular neural microstimulation may activate much larger regions than expected by stimulations: a combined experimental and modeling study. *Public Library of Science ONE*, 7:e41324.

Kameneva, T., Meffin, H., and Burkitt, A. N. Differential stimulation of ON and OFF retinal ganglion cells: a modeling study. In *Conference Proceedings of the IEEE Engineering in Medicine and Biology Society*, (2010).

Kameneva, T., Meffin, H., and Burkitt, A. N. (2011). Modelling intrinsic electrophysiological properties of ON and OFF retinal ganglion cells. *Journal of Computational Neuroscience*, 31:547–561.

Kanda, H., Morimoto, T., Fujikado, T., Tano, Y., Fukuda, Y., and Sawai, H. (2004). Electrophysiological studies of the feasibility of suprachoroidal-transretina stimulation for artificial vision in normal and RCS rats. *Investigative Ophthalmology & Visual Science*, 45:560–566.

Kang, I. K., Reem, R. E., Kaczmarowski, A. L., and Malpeli, J. G. (2009). Contrast sensitivity of cats and humans in scotopic and mesopic conditions. *Journal of Neurophysiology*, 102:831–840.

Kaplan, E. and Benardete, E. A. (2001). The dynamics of primate retinal ganglion cells. *Progress in Brain Research*, 134:17–34.

Kelly, S. K., Shire, D. B., Chen, J. H., Doyle, P., Gingerich, M. D., and Cogan, S. F. (2011). A hermetic wireless subretinal neurostimulator for vision prostheses. *IEEE Transactions on Biomedical Engineering*, 58:3197–3205.

Kim, S. Y., Sadda, S., Pearlman, J., Humayun, M. S., de Juan Jr, E., Melia, B. M., and Green, W. R. (2002). Morphometric analysis of the macula in eyes with disciform age-related macular degeneration. *Retina*, 22:471–477.

Kim, Y. T., Ito, Y., Tadai, K., Mitani, T., Kim, U. S., Kim, H. S., and Cho, B. W. (2005). Drastic change of electric double layer capaticance by surface functionalization of carbon nanotubes. *Applied Physics Letters*, 87:234106.

Klauke, S., Goertz, M., Rein, S., Hoehl, D., Thomas, U., Eckhorn, R., Bremmer, F., and Wachtler, T. (2011). Stimulation with a wireless intraocular epiretinal implant elicits visual percepts in blind humans. *Investigative Ophthalmology and Visual Science*, 52:449–455.

Koivuniemi, A. S. and Otto, K. J. (2011). Asymmetric versus symmetric pulses for cortical microstimulation. *IEEE Transactions on Neural Systems and Rehabilitation Engineering*, 19:468–476.

Kolb, H., Fernandez, E., and Nelson, R. Webvision: the organization of the retina and visual system, (2007). URL `http://www.ncbi.nlm.nih.gov/books/NBK11530/`.

Kolb, H. and Nelson, R. (1984). Chapter 2 – Neural architecture of the cat retina. *Progress in Retinal Research*, 3:21 – 60. ISSN 0278-4327.

Krebs, M. P., White, D. A., and Kaushal, S. (2009). Biphasic photoreceptor degeneration induced by light in a t17m rhodopsin mouse model of cone bystander damage. *Investigative Ophthalmology & Visual Science*, 50:2956–2965.

Kuffler, S. W. (1953). Discharge patterns and functional organization of mammalian retina. *Journal of Neurophysiology*, 16:37–68.

Leventhal, A. G., Rodieck, R. W., and Dreher, B. (1981). Retinal ganglion cell classes in the old world monkey: morphology and central projections. *Science*, 213:1139–1142.

Levick, W. R. (1975). Form and function of cat retinal ganglion cells. *Nature*, 254:659–662.

Liu, W., Vichienchom, K., Clements, M., DeMarco, S. C., Hughes, C., McGucken, E., Humayun, M. S., de Juan Jr, E., Weiland, J. D., and Greenberg, R. J. (2000). A neuro-stimulus chip with telemetry unit for retinal prosthetic device. *IEEE Journal of Solid-State Circuits*, 35:1487–1497.

Luan, L., Ren, C., Lau, B. W., Yang, J., Pickard, G. E., So, K., and Pu, M. (2011). Y-like retinal ganglion cells innervate the dorsal raphe nucleus in the mongolian gerbil (meriones unguiculatus). *PLoS ONE*, 6:e18938.

Maguire, A. M., Simonelli, F., Auricchio, A., High, K. A., and Bennett, J. (2008). Safety and efficacy of gene transfer for Leber's Congenital Amaurosis. *The New England Journal of Medicine*, 358:2240–2248.

Mahadevappa, M., Weiland, J. D., Yanai, D., Fine, I., Greenberg, R. J., and Humayun, M. S. (2005). Perceptual thresholds and electrode impedance in three retinal prosthesis subjects. *IEEE Transactions on Neural Systems and Rehabilitation Engineering*, 13:201–206.

Majji, A. B., Humayun, M. S., Weiland, J. D., Suzuki, S., D'Anna, S. A., and de Juan Jr, E. (1999). Long-term histological and eletrophysiological results of an inactive epiretinal electrode array implantation in dogs. *Investigative Ophthalmology & Visual Science*, 40:2073–2081.

Marc, R. E., Jones, B. W., Watt, C. B., and Strettoi, E. (2003). Neural remodeling in retinal degeneration. *Progress in Retinal and Eye Research*, 22:607–655.

Margalit, E., Babai, N., Luo, J., and Thoreson, W. B. (2011). Inner and outer retinal mechanisms engaged by epiretinal stimulation in normal and rd mice. *Visual Neuroscience*, 28:145–154.

Margalit, E. and Thoreson, W. B. (2006). Inner retinal mechanisms engaged by retinal electrical stimulation. *Investigative Ophthalmology & Visual Science*, 47:2606–2612.

Margolis, D. J. and Detwiler, P. B. (2007). Different mechanisms generate maintained activity in ON and OFF retinal ganglion cells. *The Journal of Neuroscience*, 27:5994–6005.

Margolis, D. J. and Detwiler, P. B. (2011). Cellular origin of spontaneous ganglion cell spike activity in aminal models of retinitis pigmentosa. *Journal of Ophthalmology*, Volume 2011:Article ID 507037, 6 pages.

Margolis, D. J., Gartland, A. J., Euler, T., and Detwiler, P. B. (2010). Dendritic calcium signaling in ON and OFF mouse retinal ganglion cells. *The Journal of Neuroscience*, 30:7127–7138.

Margolis, D. J., Newkirk, G., Euler, T., and Detwiler, P. B. (2008). Functional stability of retinal ganglion cells after degeneration-induced changes in synaptic input. *The Journal of Neuroscience*, 28:6526–6536.

Masland, R. H. (2001). The fundamental plan of the retina. *Nature*, 4:877–886.

Maslim, J., Valter, K., Egensperger, R., Holländer, H., and Stone, J. (1997). Tissue oxygen during a critical developmental period controls the death and survival of photoreceptors. *Investigative Ophthalmology & Visual Science*, 38:1667–1677.

Maslim, J., Webster, M., and Stone, J. (1986). Stages in the structural differentiation of retinal ganglion cells. *The Journal of Comparative Neurology*, 254:382–402.

Mather, G. *Foundations of sensation and perception*, chapter 6: The physics of vision – light and the eye, pages 145–177. Psychology Press Ltd, (2009).

Mazzoni, F., Novelli, E., and Strettoi, E. (2008). Retinal ganglion cells survive and maintain normal dendritic morphology in a mouse model of inherited photoreceptor degeneration. *Journal of Neuroscience*, 28:14282–14292.

McHardy, J., Robblee, L. S., Marston, J. M., and Brummer, S. B. (1980). Electrical-stimulation with Pt electrodes. 4. Factors influencing Pt dissolution in inorganic saline. *Biomaterials*, 1:129–134.

McIntyre, C. C. and Grill, W. M. (2000). Selective microstimulation of central nervous system neurons. *Annals of Biomedical Engineering*, 28:219–233.

Mehenti, N. Z., Fishman, H. A., and Bent, S. F. (2007). A model neural interface based on functional chemical stimulation. *Biomedical Microdevices*, 9:579–586.

Merigan, W. H., Byrne, C. E., and Maunsell, J. H. R. (1991). Does primate motion perception depend on the magnocellular pathway? *The Journal of Neuroscience*, 11:3422–3429.

Merigan, W. H. and Eskin, T. A. (1986). Spatio-temporal vision of macaques with severe loss of pb retinal ganglion cells. *Vision Research*, 26:1751–1761.

Merrill, D. R., Bikson, M., and Jefferys, J. G. R. (2005). Electrical stimulation of excitable tissue: design of efficacious and safe protocols. *Journal of Neuroscience Methods*, 141:171–198.

Michael, C. R. (1988). Retinal afferent arborization patterns, dendritic field orientations, and the segregation of function in the lateral geniculate nucleus of the monkey. *Proceedings of the National Academy of Sciences*, 85:4914–4918.

Miller, C. A., Robinson, B. K., Rubinstein, J. T., Abbas, P. J., and Runge-Samuelson, C. L. (2001). Auditory nerve responses to monophasic and biphasic electric stimuli. *Hearing Research*, 151:79–94.

Murphy, G. J. and Rieke, F. (2006). Network variability limits stimulus-evoked spike timing precision in retinal ganglion cells. *Neuron*, 52:511–524.

Nagar, S., Krishnamoorthy, V., Cherukuri, P., Jain, V., and Dhingra, N. K. (2009). Early remodeling in an inducible animal model of retinal degeneration. *The Journal of Neuroscience*, 160:517–529.

Negi, S., Bhandari, R., Rieth, L., Van Wagenen, R., and Solzbacher, F. (2010). Neural electrode degradation from continuous electrical stimulation: comparison of sputtered and activated iridium oxide. *Journal of Neuroscience Methods*, 186:8–17.

Neher, E. (1992). Correction for liquid junction potentials in patch clamp experiments. *Methods in Enzymology*, 207:123–131.

Neher, E. and Sakmann, B. (1976). Single-channel currents recorded from membrane of denervated frog muscle fibres. *Nature*, 260:799–802.

Nelson, R., Famiglietti, E. V., and Kolb, H. (1978). Intracellular staining reveals different levels of stratification for on- and off-center ganglion cells in cat retina. *Journal of Neurophysiology*, 41:472–483.

Nelson, R. and Kolb, H. *The visual neurosciences*, chapter 18 – ON and OFF pathways in the vertebrate retina and visual system, pages 260–278. MIT Press, Cambridge, MA, (2003).

O'Brien, B. J., Isayama, T., Richardson, R., and Berson, D. M. (2002). Intrinsic physiological properties of cat retinal ganglion cells. *The Journal of Physiology*, 538:787–802.

O'Hearn, T. M., Srinivas, R. S., Weiland, J. D., Maia, M., Margalit, E., and Humayun, M. S. (2006). Electrical stimulation in normal and retinal degeneration (rd1) isolated mouse retina. *Vision Research*, 46:3198–3204.

Olsson, J. E., Gordon, J. W., Pawlyk, B. S., Roof, D., Hayes, A., Molday, R. S., Mukai, S. M., Cowley, G. S., Berson, E. L., and Dryja, T. P. (1992). Transgenic mice with a rhodopsin mutation (pro23his): A mouse model of autosomal dominant retinitis pigmentosa. *Neuron*, 9:815–830.

Parver, L. M., Auker, C. R., and Carpenter, D. O. (1983). Choroidal blood flow: III. Reflexive control in human eyes. *Archives of Ophthalmology*, 101: 1604–1606.

Pasternak, T., Merigan, W. H., Flood, D. G., and Zehl, D. (1983). The role of area centralis in the spatial vision of the cat. *Vision Research*, 23:1409–1416.

Peichl, L. (1989). Alpha and delta ganglion cells in the rat retina. *The Journal of Comparative Neurology*, 286:120–139.

Peichl, L. (1991). Alpha ganglion cells in mammalian retinae: common properties, species differences, and some comments on other ganglion cells. *Visual Neuroscience*, 7:155–169.

Perry, V. H. (1979). The ganglion cell layer of the retina of the rat: a Golgi study. *Proceedings of the Royal Society B*, 204:363–375.

Perry, V. H. and Cowey, A. (1984). Retinal ganglion cells that project to the superior colliculus and pretectum in the macaque monkey. *Neuroscience*, 12:1125–1137.

Perry, V. H., Oehler, R., and Cowey, A. (1984). Retinal ganglion cells that project to the dorsal lateral geniculate nucleus in the macaque monkey. *Neuroscience*, 12:1101–1123.

Petrusca, D., Grivich, M. I., Sher, A., Field, G. D., Gauthier, J. L., Greschner, M., Shlens, J., Chichilnisky, E. J., and Litke, A. M. (2007). Identification and characterization of a Y-like primate retinal ganglion cell type. *The Journal of Neuroscience*, 27:11019–11027.

Pezaris, J. S. and Reid, R. C. (2006). Demonstration of artificial visual percepts generated through thalamic microstimulation. *Proceedings of the National Academy of Sciences*, 104:7670–7675.

Piyathaisere, D. V., Margalit, E., Chen, S., Shyu, J., D'Anna, S. A., Weiland, J. D., Grebe, R. R., Grebe, L., Fujii, G. Y., Kim, S. Y., Greenberg, R. J., de Juan Jr., E., and Humayun, M. S. (2003). Heat effects on the retina. *Ophthalmic surgery, lasers & imaging*, 34:114–120.

Prado-Guitierrez, P., Fewster, L. M., Heasman, M., McKay, C. M., and Shepherd, R. K. (2006). Effect of interphase gap and pulse duration on electrically evoked potentials is correlated with auditory nerve survival. *Hearing Research*, 215:47–55.

Pu, M., Xu, L., and Zhang, H. (2006). Visual response properties of retinal ganglion cells. *Investigative Ophthalmology and Visual Science*, 47:3579–3585.

Purves, D. *Neuroscience, 2nd edition*, chapter 11 – Vision: The Eye. Sinauer Associates, Inc., (2001).

Quigley, H. A. (1998). Neuronal death in glaucoma. *Progress in Retinal and Eye Research*, 18:39–57.

Ranck Jr, J. B. (1975). Which elements are excited in electrical stimulation of mammalian central nervous system: a review. *Brain Research*, 98:417–440.

Rattay, F. (1999). The basic mechanism for the electrical stimulation of the nervous system. *Neuroscience*, 89:335–346.

Rattay, F., Paraedes, L. P., and Leao, R. N. (2012). Strength-duration relationship for intra- versus extracellular stimulation with microelectrodes. *Neuroscience*, 214:1–13.

Rizzo III, J. F. (2011). Update on retinal prosthetic research: the Boston Retinal Implant project. *Journal of Neuro-Ophthalmology*, 31:160–168.

Rizzo III, J. F., Wyatt, J., Loewenstein, J., Kelly, S. K., and Shire, D. B. (2003). Perceptual efficacy of electrical stimulation of human retina with a microelectrode array during short-term surgical trials. *Investigative Ophthalmology & Visual Science*, 44:5362–5369.

Roach, K. L. *Electrochemical models for electrode behavior in retinal prostheses.* PhD thesis, Department of Electrical Engineering and Computer Science, Massachusetts Institute of Technology, (2003).

Robinson, D. W. and Chalupa, L. M. (1997). The intrinsic temporal properties of alpha and beta retinal ganglion cells are equivalent. *Current Biology*, 7: 366–374.

Rodieck, R. W. and Watanabe, M. (1993). Survey of the morphology of macaque retinal ganglion cells that project to the pretectum, superior colliculus, and parvicellular laminae of the lateral geniculate nucleus. *The Journal of Comparative Neurology*, 338:289–303.

Rodrigues, E. B. *Retina implant project - chronic implantation of active epiretinal implants.* PhD thesis, Department of Ophthalmology, Philipps University of Marburg, (2003).

Rose, T. L. and Robblee, L. S. (1990). Electrical stimulation with Pt electrodes: VIII. Electrochemically safe charge injection limits with 0.2 ms pulses. *IEEE Transactions on Biomedical Engineering*, 37:1118–1120.

Roska, B. and Werblin, F. S. (2001). Vertical interactions across ten parallel, stacked representations in the mammalian retina. *Nature*, 410:583–587.

Saito, H. (1983). Morphology of physiologically identified X-, Y-, and W-type retinal ganglion cells of the cat. *The Journal of Comparative Neurology*, 221: 279–288.

Santos, A., Humayun, M. S., de Juan Jr, E., Greenberg, R. J., Marsh, M. J., Klock, I. B., and Milam, A. H. (1997). Preservation of the inner retina in retinitis pigmentosa. *Archives of Ophthalmology*, 115:511–515.

Schalch, W. (1992). Carotenoids in the retina – a review of their possible role in preventing or limiting damage caused by light and oxygen. *EXS*, 62: 280–298.

Schiefer, M. A. and Grill, W. M. (2006). Sites of neuronal excitation by epiretinal electrical stimulation. *IEEE Transactions on Neural Systems and Rehabilitation Engineering*, 14:5–13.

Schiller, P. H. and Logothetis, N. K. (1990). The color-opponent and broad-band channels of the primate visual system. *Trends in Neurosciences*, 13: 1990.

Schiller, P. H., Logothetis, N. K., and Charles, E. R. (1990). Functions of the colour-opponent and broad-band channels of the visual system. *Nature*, 343:68–70.

Sefton, A. J. and Dreher, B. *The rat nervous system*, chapter 32: Visual system, pages 1083–1165. Academic Press, (1995).

Sekirnjak, C., Hottowy, P., Sher, A., Dabrowski, W., Litke, A. M., and Chichilnisky, E. J. (2006). Electrical stimulation of mammalian retinal ganglion cells with multielectrode arrays. *Journal of Neurophysiology*, 95: 3311–3327.

Sekirnjak, C., Hottowy, P., Sher, A., Dabrowski, W., Litke, A. M., and Chichilnisky, E. J. (2008). High-resolution electrical stimulation of primate retina for epiretinal implant design. *The Journal of Neuroscience*, 28: 4446–4456.

Sekirnjak, C., Hulse, C., Jepson, L. H., Hottowy, P., Sher, A., Dabrowski, W., Litke, A. M., and Chichilnisky, E. J. (2009). Loss of responses to visual but not electrical stimulation in ganglion cells of rats with severe photoreceptor degeneration. *Journal of Neurophysiology*, 102:3260–3269.

Sekirnjak, C., Jepson, L. H., Hottowy, P., Sher, A., Dabrowski, W., Litke, A. M., and Chichilnisky, E. J. (2011). Changes in physiological properties of rat ganglion cells during retinal degeneration. *Journal of Neurophysiology*, 105:2560–2571.

Shapley, R. and Perry, V. H. (1986). Cat and monkey retinal ganglion cells and their visual functional roles. *Trends in Neurosciences*, 9:229–235.

Shepherd, R. K. and Javel, E. (1999). Electrical stimulation of the auditory nerve: II. Effect of stimulus waveshape on single fibre response properties. *Hearing Research*, 130:171–199.

Shepherd, R. K., Murray, M. T., Houghton, M. E., and Clark, G. M. (1985). Scanning electron microscopy of chronically stimulated platinum intracochlear electrodes. *Biomaterials*, 6:237–242.

Shintani, K., Shechtman, D. L., and Gurwood, A. S. (2009). Review and update: current treatment trends for patients with retinitis pigmentosa. *Optometry*, 80:384–401.

Shivdasani, M. N., Luu, C. D., Cicione, R., Fallon, J. B., Allen, P. J., Leuenberger, J., Suaning, G. J., Lovell, N. H., Shepherd, R. K., and Williams, C. E. (2010). Evaluation of stimulus parameters and electrode geometry for an effective suprachoroidal retinal prosthesis. *Journal of Neural Engineering*, 7:036008.

Siu, T. L. and Morley, J. W. (2008). Suppression of visual cortical evoked responses following deprivation of pattern vision in adult mice. *European Journal of Neuroscience*, 28:484–490.

Stanford, L. R. (1987). X-cells in the cat retina: relationships between the morphology and physiology of a class of cat retinal ganglion cells. *Journal of Neurophysiology*, 58:940–964.

Stanford, L. R. and Murray Sherman, S. (1984). Structure/function relationships of retinal ganglion cells in the cat. *Brain Research*, 297:381–386.

Stasheff, S. F. (2008). Emergence of sustained spontaneous hyperactivity and temporary preservation of OFF responses in ganglion cells of the retinal degeneration (rd1) mouse. *Journal of Neurophysiology*, 99:1408–1421.

Stasheff, S. F., Shankar, M., and Andrews, M. P. (2011). Developmental time course distinguishes changes in spontaneous and light-evoked retinal ganglion cell activity in rd1 and rd10 mice. *Journal of Neurophysiology*, 105:3002–3009.

Steinberg, R. H., Reid, M., and Lacy, P. L. (1973). The distribution of rods and cones in the retina of the cat (*Felis domesticus*). *The Journal of Comparative Neurology*, 148:229–248.

Sterling, P. (1983). Microcircuitry of the cat retina. *Annual Review of Neuroscience*, 6:149–185.

Stett, A., Barth, W., Weiss, S., Haemmerle, H., and Zrenner, E. (2000). Electrical multisite stimulation of the isolated chicken retina. *Vision Research*, 40:1785–1795.

Sun, W., Li, N., and He, S. (2002). Large-scale morphological survey of rat retinal ganglion cells. *Visual Neuroscience*, 19:483–493.

Suzuki, A., Ivandini, T. A., Yoshimi, K., Fujishima, A., Oyama, G., Nakazato, T., Hattori, N., Kitazawa, S., and Einaga, Y. (2007). Fabrication, characterization, and application of boron-doped diamond microelectrodes for in vivo dopamine detection. *Analytical Chemistry*, 79:8608–8615.

Suzuki, S., Humayun, M. S., Weiland, J. D., Chen, S., Margalit, E., Piyathaisere, D. V., and de Juan Jr, E. (2004). Comparison of electrical stimulation thresholds in normal and retinal degenerated mouse retina. *Japanese Journal of Ophthalmology*, 48:345–349.

Takahashi, M., Miyoshi, H., Verma, I. M., and Gage, F. H. (1999). Rescue from photoreceptor degeneration in the rd mouse by human immunodeficiency virus vector-mediated gene transfer. *Journal of Virology*, 73:7812–7816.

Tang, L., Tsai, C., Gerberich, W. W., Kruckeberg, L., and Kania, D. R. (1995). Biocompatibility of chemical-vapor-deposited diamond. *Biomaterials*, 16: 483–488.

Taylor, H. R., Pezzullo, M. L., and Keeffe, J. E. (2006). The economic impact and cost of visual impairment in Australia. *British Journal of Ophthalmology*, 90:272–275.

Taylor, W. R. and Wässle, H. (1995). Receptive field properties of starburst cholinergic amacrine cells in the rabbit retina. *European Journal of Neuroscience*, 7:2308–2321.

Theorét, H., Merabet, L., and Pascual-Leone, A. (2004). Behavioral and neuroplastic changes in the blind: evidence for functionally relevant cross-modal interactions. *Journal of Physiology - Paris*, 98:221–233.

Thomson, J. A. *Outlines of zoology.* New York, Appleton, (1916).

Tian, N. and Copenhagen, D. R. (2003). Visual stimulation is required for refinement of ON and OFF pathways in postnatal retina. *Neuron*, 39:85–96.

Troy, J. B. and Shou, T. (2002). The receptive fields of cat retinal ganglion cells in physiological and pathological states: where we are after half a century of research. *Progress in Retinal and Eye Research*, 21:263–302.

Tsai, D., Morley, J. W., Suaning, G. J., and Lovell, N. H. (2009). Direct activation and temporal response properties of rabbit retinal ganglion cells following subretinal stimulation. *Journal of Neurophysiology*, 102:2982–2993.

Varney, M. W., Aslam, D. M., Janoudi, A., Ho-Yin, C., and Wang, D. H. (2011). Polycrystalline-diamond MEMS biosensors including neural microelectrode-arrays. *Biosensors*, 1:118–133.

Veitinger, S. The patch-clamp technique, (2011). URL `http://www.leica-microsystems.com/science-lab/the-patch-clamp-technique/`.

Verweij, J., Hornstein, E. P., and Schnapf, J. L. (2003). Surround antagonism in macaque cone photoreceptors. *The Journal of Neuroscience*, 23:10249–10257.

Walter, P., Kisvárday, Z. F., Gortz, M., Alteheld, N., Rossler, G., Stieglitz, T., and Eysel, U. T. (2005). Cortical activation via an implanted wireless retinal prosthesis. *Investigative Ophthalmology & Visual Science*, 46:1780–1785.

Wang, X. J., Rinzel, J., and Rogawski, M. A. (1991). A model of the T-type calcium current and the low-threshold spike in thalamic neurons. *Journal of Neurophysiology*, 66:839–850.

Wässle, H. (2004). Parallel processing in the mammalian retina. *Nature Reviews Neuroscience*, 5:747–757.

Wässle, H. and Boycott, B. B. (1991). Functional architecture of the mammalian retina. *Physiological Reviews*, 71:447–480.

Wässle, H. and Illing, R. B. (1980). The retinal projection to the superior colloculus in the cat: a quantitative study with HRP. *The Journal of Comparative Neurology*, 190:333–356.

Watanabe, M. and Rodieck, R. W. (1989). Parasol and midget ganglion cells of the primate retinas. *The Journal of Comparative Neurology*, 289:434–454.

Watanabe, T., Shimizu, T. K., Tateyama, Y., Kim, Y., Kawai, M., and Einaga, Y. (2010). Giant electric double-layer capacitance of heavily boron-doped diamond electrode. *Diamond and Related Materials*, 19:772–777.

Weber, A. J. and Harman, C. D. (2005). Structure-function relations of parasol cells in the normal and glaucomatous primate retina. *Investigative Ophthalmology and Visual Science*, 46:3197–3207.

Weiland, J. D., Cho, A. K., and Humayun, M. S. (2011). Retinal prostheses: current clinical results and future needs. *Ophthalmology*, 118:2227–2237.

Weiland, J. D., Liu, W., and Humayun, M. S. (2005). Retinal prosthesis. *Annual Review of Biomedical Engineering*, 7:361–401.

Weitz, A. C., Behrend, M. R., Humayun, M. S., Chow, R. H., and Weiland, J. D. (2011). Interphase gap decreases electrical stimulation threshold of retinal ganglion cells. *Conference Proceedings of the IEEE Engineering in Medicine and Biology Society*, 2011:6725–6728.

Werblin, F. S. and Dowling, J. E. (1969). Organization of the retina of the mudpuppy, necturus maculosus. II. Intracellular recording. *The Journal of Physiology*, 32:339–355.

Wilke, R., Gabel, V., Sachs, H., Bartz-Schmidt, K. U., Gekeler, F., Besch, D., Szurman, P., Stett, A., Wilhelm, B., Peters, T., Harscher, A., Greppmaier, U., Kibbel, S., Benav, H., Bruckmann, A., Stingl, K., Kusnyerik, A., and Zrenner, E. (2011). Spatial resolution and perception of patterns mediated by a subretinal 16-electrode array in patients blinded by hereditary retinal dystrophies. *Investigative Ophthalmology & Visual Science*, 52:5995–6003.

Wilms, M. and Eckhorn, R. (2005). Spatiotemporal receptive field properties of epiretinally recorded spikes and local electroretinograms in cats. *BMC Neuroscience*, doi:10.1186/1471-2202-6-50(50).

Wilms, M., Eger, M., Schanze, T., and Eckhorn, R. (2003). Visual resolution with epi-retinal electrical stimulation estimated from activation profiles in cat visual cortex. *Visual Neuroscience*, 20:543–555.

Wong, R. C. S., Cloherty, S. L., Ibbotson, M. R., and O'Brien, B. J. (2012). Intrinsic physiological properties of rat retinal ganglion cells with a comparative analysis. *Journal of Neurophysiology*, 108:2008–2023.

Wong, Y. T., Chen, S. C., Seo, J. M., Morley, J. W., Lovell, N. H., and Suaning, G. J. (2009). Focal activation of the feline retina via a suprachoroidal electrode array. *Vision Research*, 49:825–833.

Xie, S. T., Shafer, G., Wilson, C. G., and Martin, H. B. (2006). In vitro adenosine detection with a diamond-based sensor. *Diamond and Related Materials*, 15:225–228.

Yamauchi, Y., Franco, L. M., Jackson, D. J., Naber, J. F., Ziv, O. R., Rizzo III, J. F., Kaplan, H. J., and Enzmann, V. (2005). Comparison of electrically evoked cortical potential thresholds generated with subretinal or suprachoroidal placement of a microelectrode array in the rabbit. *Journal of Neural Engineering*, 2:S48–S56.

Yanai, D., Weiland, J. D., Mahadevappa, M., Greenberg, R. J., Fine, I., and Humayun, M. S. (2007). Visual performance using a retinal prosthesis in three subjects with retinitis pigmentosa. *American Journal of Ophthalmology*, 143:820–827.

Yang, Y. T., Lin, P. K., Wan, C., Yang, W. C., Lin, L. J., Wu, C. Y., and Chiao, C. C. (2011). Responses of rabbit retinal ganglion cells to subretinal electrical stimulation using a silicon-based microphotodiode array. *Investigative Ophthalmology and Visual Science*, 52:9353–9361.

Yoshimi, K., Naya, Y., Mitani, N., Kato, T., Inoue, M., Natori, S., Takahashi, T., Weitemier, A., Nishikawa, N., McHugh, T., Einaga, Y., and Kitazawa, S. (2011). Phasic reward responses in the monkey striatum as detected by voltammetry with diamond microelectrodes. *Neuroscience Research*, 71: 49–62.

Zaghloul, Z., Boahen, K., and Demb, J. B. (2003). Different circuits for ON and OFF retinal ganglion cells cause different contrast sensitivities. *Journal of Neuroscience*, 23:2645–2654.

Zhou, J. A., Woo, S. J., Park, S. I., Kim, E. T., Seo, J. M., Chung, H., and Kim, S. J. (2008). A suprachoroidal electrical retinal stimulator design for long-term animal experiments and in vivo assessment of its feasibility and biocompatibility in rabbits. *Journal of Biomedicine and Biotechnology*, doi:10.1155/2008/547428.

Zrenner, E. (2002). Will retinal implants restore vision? *Science*, 295:1022–1025.

Zrenner, E., Bartz-Schmidt, K. U., Benav, H., Besch, D., Bruckmann, A., Gabel, V., Gekeler, F., Greppmaier, U., Harscher, A., Kibbel, S., Koch, J., Kusnyerik, A., Peters, T., Stingl, K., Sachs, H., Stett, A., Szurman, P., Wilhelm, B., and Wilke, R. (2011). Subretinal electronic chips allow blind patients to read letters and combine them to words. *Proceedings of the Royal Society B*, 278:1489–1497.

Zrenner, E., Stett, A., Weiss, S., Aramant, R. B., Guenther, E., Kohler, K., Miliczek, K. D., Seiler, M. J., and Haemmerle, H. (1999). Can subretinal microphotodiodes successfully replace degenerated photoreceptors? *Vision Research*, 39:2555–2567.